Construction of typical facies models and the three-dimensional distribution of their petrophysical parameters

A foundation of understanding 3D seismic facies

Master Thesis

from
Denise Hofer

Chair of Geophysics

Montanuniversity Leoben

Leoben, February 2018

Affidavit

Ich erkläre an Eides statt, dass ich diese Arbeit selbständig verfasst, andere als die angegebenen Quellen und Hilfsmittel nicht benutzt und mich auch sonst keiner unerlaubten Hilfsmittel bedient habe.

I declare in lieu of oath, that I wrote this thesis and performed the associated research myself, using only literature cited in this volume.

(Denise Hofer)

Leoben, Februar 21, 2018

Acknowledgement

I deeply want to thank my thesis advisors Dipl.-Ing. Johannes Amtmann from the University of Leoben and Geo5 GmbH, Hon.Prof. Dr.rer.nat.habil. Dr.habil. Jürgen Schön as well as Ass.Prof. Dipl.-Ing. Dr.mont. Nina Gegenhuber from the University of Leoben for providing me with this master thesis and supporting me over the duration of my work and their dedicated assistance. Especially I want to thank Dipl.-Ing. Johannes Amtmann with whom I worked out a new way of facies modeling and creating fact sheets.

Additionally I want to thank Dipl.-Ing. Dr. mont. Marcellus G. Schreilechner and Dipl.-Ing. Christoph G. Eichkitz from the Geo5 GmbH and members of the research project who supported me throughout the project.

It was a pleasure for me to work with and learn from such skilled and enthusiastic people. For that opportunity and experience I am very thankful.

Finally, I want to thank my family and friends who supported me during my time of study. Most of all my parents and my boyfriend Benedikt, who were always there for me in times of hardship and kept me going.

Kurzfassung

Um 3D Seismik interpretieren zu können ist das Verständnis der seismischen und geologischen Fazies von Bedeutung. Hierfür sind Geometrie einer Fazies und die petrophysikalischen Eigenschaften dieser von großer Bedeutung. Um dieses Verständnis der seismischen und geologischen Fazies zu verbessern, müssen diese Fazien genauer untersucht werden. Diese Masterarbeit versucht dies, und befasst sich mit der Konstruktion von dreidimensionalen Faziesmodellen und der Verteilung ihrer petrophysikalischen Eigenschaften. Dazu ist diese Masterarbeit in zwei Teile geteilt.

Im ersten Teil wurden Geometrie und Fazies der verschiedenen geologischen Körper (Fluss, Fächer, Salzdom, Riff, Vulkan, und Karst) aus der Literatur entnommen. Anhand dieser Informationen wurde ein dreidimensionales Modell, anhand der Software „Petrel" (3D seismische Interpretations- und Modellierungssoftware), jedes einzelnen Ablagerungsraums konstruiert. Um ein optimales Modell der seismischen Fazies zu erzielen kamen zwei Methoden zur Faziesmodellierung zum Einsatz. Methode I für fluviale Systeme und Methode II, welche ein neu entwickelter Workflow ist, für komplexe strukturelle und stratigraphische Ablagerungssysteme. Für die Methode I wurde eine vordefinierte Funktion, welche von einer kommerziellen Software zur Verfügung gestellt wird, verwendet. Diese Funktion erlaubte die Konstruktion von Faziesmodellen mit Objekten die generiert und stochastisch verteilt wurden. Die grundlegende Idee der Methode II basiert auf der Erstellung eines klassischen geologischen Modells bei den Störungen und Horizonte in 3D interpretiert werden. Anstelle einer 3D Seismik wurden Profile von echten Beispielen für das Modellieren verwendet.

Der zweite Teil untersucht den Einfluss der petrophysikalischen Parameter (Kompression- und Scherwellengeschwindigkeit, Dichte und Porosität) auf die einzelnen geologischen Körper. Dafür wurde ein Bereich von typischen petrophysikalischen Parametern für jede Fazies aus der Literatur gewählt. Zusätzlich wurde der Einfluss von Porosität, Tongehalt, Porenfluid und Tiefe auf Dichte und Geschwindigkeit berücksichtigt.

Das Ergebnis dieser Masterarbeit ist in Form von Faktenblättern zusammengefasst. Für jeden einzelnen geologischen Körper wurde ein Faktenblatt mit allen notwendigen Information erstellt. Solch ein Faktenblatt repräsentiert einen geologischen Körper und zeigt die Verbindung der wichtigsten Fazies Komponenten, ihrer Ausmaße (verwendet für die Modellierung) und ihrer petrophysikalischen Parameter. Schlussendlich können diese strukturellen Modelle und ihre petrophysikalischen Parameter für seismisches „Forward Modeling" verwendet werden.

Abstract

For interpretation of 3D seismic the understanding of geological facies and seismic facies is important. Therefore, the geometry and properties of the facies are of importance. To improve this, a research study is done, which is dealing with the construction of three dimensional facies models. Furthermore the distribution of their petrophysical properties is discussed. This study is divided into two parts.

In the first part, information about the geometry and about facies of different geological bodies (channel, fan, salt dome, reef, volcano and karst) were taken from literature. Based on this results, a three dimensional model with "Petrel software" (3D seismic interpretation and modeling software) of each depositional environment was constructed. To achieve an optimal model of the seismic facies two methods were used. Method I for fluvial systems and Method II, which is a newly created workflow, for complex structural or stratigraphic depositional systems. For Method I a predefined function, which is provided by a commercial software, was used. This function allowed the building of facies models with objects, which are generated and distributed stochastically. The basic idea of Method II is based on the creation of a classical geological model by interpretation of faults and horizons in 3D. Instead of a 3D seismic, profiles from real examples were used.

The second part is dealing with petrophysical parameters (density, compressional- and shear wave velocity) on each geological body. Therefore, a range of typical petrophysical parameters of each facies were obtained from literature information. In addition, the influence of porosity, clay content, pore fluid change and depth on density and velocity were considered.

The result of this study is summarized in form of fact sheets. For each geobody a fact sheet with all useful information was created. Such a fact sheet represents a geological body and shows the link between the major facies compounds, their measurements (used for modeling) and their petrophysical parameters. Finally, these facies models and their petrophysical properties can be used for seismic forward modeling.

Table of contents

List of figures

List of tables

Abbreviations

1 Introduction

A facies is a distinctive rock that can be characterized by lithology, texture, sedimentary structures and fossil content (Reading and Levell 1996). These characteristics are strongly dependent on formation and hence there is a link to depositional environments. Reading and Levell (1996) declared that the name lithofacies is more appropriate than facies if fossils are absent. By relating to the process of formation, facies can be named for example "fluvial facies" or "turbidite facies". The name of facies can be used as long as it is justified. For this study the facies name is either related to lithology or to the formation process. A series of facies that pass gradually from one into the other is called a facies sequence and was introduced by Walther (1894). Walther's law of facies declared that facies is lying on top of each other along a crustal profile and was once formed beside each other.

This study deals with seismic facies that represent sedimentary units in seismic scale. Seismic resolution is around five to tens of meters and therefore only medium to large scale sedimentary units are resolved. The resolution depends on the input signal and the investigation depth (Bacon at al., 2003). In general, the higher the frequency signal (the lower the wavelength) the better the resolution. The ranges of seismic signals lie between 3-120Hz. Emery and Myers (1996) show a comparison of a single cycle sine wave of 30Hz in medium velocity of 2000m/s to the Big Ben in London and a gamma ray log through the Beatrice Oil Field (Figure 1). Seismic facies is characterized by the lithology (such as sandstone), bedding (such as massive or interbedded), petrography (porosity, shale content and fluid fill) and seismic properties (density, compressional- and shear wave velocity) (after Avseth, 2007).

This research study is the first of three master thesis for the GeoSegment3D research project. The project investigates on Clustering Algorithms to extract facies. Therefore, different attributes are necessary for facies determination. The goal of this thesis is to provide the project with facies models and petrophysical parameters that respond to the individual facies. Because of their major control on geometry and petrophysical parameters, facies can be linked to seismic attributes.
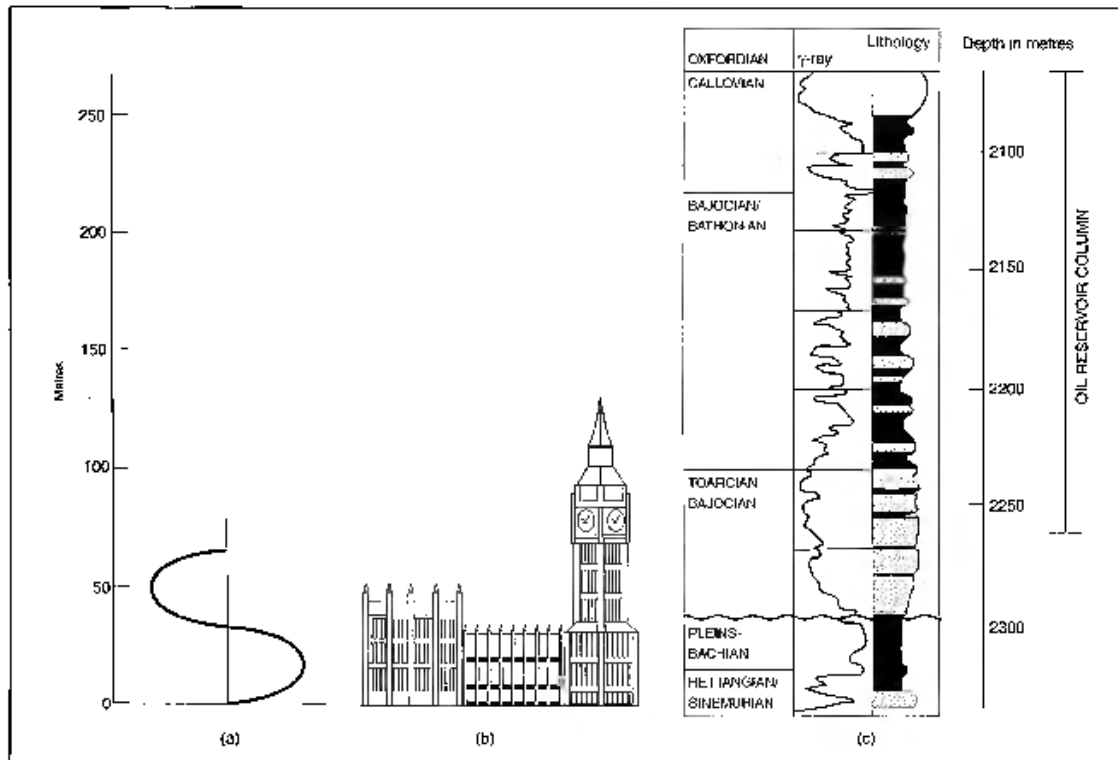
Figure 1: (a) single cycle sine wave (30Hz and 2000m/s or 60Hz and 4000m/s); (b) Big Ben in London (around 115m high); (c) gamma ray log through the Beatrice Oil Field).

For creating the final facies models the first part of this master thesis investigates on the different facies types and their geometrical extent within a typical geological body (channel, fan, salt dome, reef, volcano and karst). Each geological body is represented by a facies model. The architecture of geological bodies in nature can vary on a wide scale. For the channels and the submarine fan typical geometrical values were taken from literature. In case of the fluvial channel four facies models were created, because the architecture of a channel typically changes from a braided to a meandering channel with decreasing distance from the origin. For the salt dome, reef, volcano and karst bodies real examples with already defined measurements from literature were used to create the facies models.

These facies models are the basis for facies modeling. Facies modeling is the process of populating facies as discrete data in a 3D model. Facies can be distributed by either stochastic or deterministic methods. Stochastic methods are cell-based methods or object-based methods. Cell-based methods are further differentiated in two-point statistics and multi-point statistics and use statistical methods like the variogram or multiple point statistics from a training image to gain the spatial continuity between the grid cells (Pyrz et al., 2014). The resulting models do

not reflect clean geometries, because cell-based methods assign data to the model cell and continue randomly. Object-based methods however assign predefined geometric bodies stochastically within a background facies. These methods completely honor the geometric shape of the objects. Object based methods, used as Method I, gained wide popularity especially in modeling fluvial systems as well as lobe systems (Pyrz et al., 2014). In case of modeling complex internal structures of a geological body (salt dome, reef, volcano, karst) with several distinct facies, which need to be in a specific order and place, these methods are limited and a deterministic approach is required. Interactive facies modeling allows a deterministic placement of facies within a 3D grid. With different painting tools facies can be drawn directly into the grid, but it is more suitable for adding facies in an already existing facies model (Schlumberger, 2015). To model facies bodies with a complex architectural structure without existing well data, none of the introduced methods work properly. Therefore, this study shows a new workflow of modeling a salt dome, reef, volcano and karst body. The idea origins from geological modeling, where faults and horizons are picked along a seismic, a fault model and a 3D grid is created, horizons are made and zonation and layering is performed. Hence Method II ("Radial Module Process") is a new workflow of geological modeling, which uses profiles from geological bodies instead of a seismic section (Figure 2). In this case boundaries between the different facies (faults and horizons) are picked along the profiles, which are placed radial around the center. For each facies one grid is generated, which build up the final facies model.
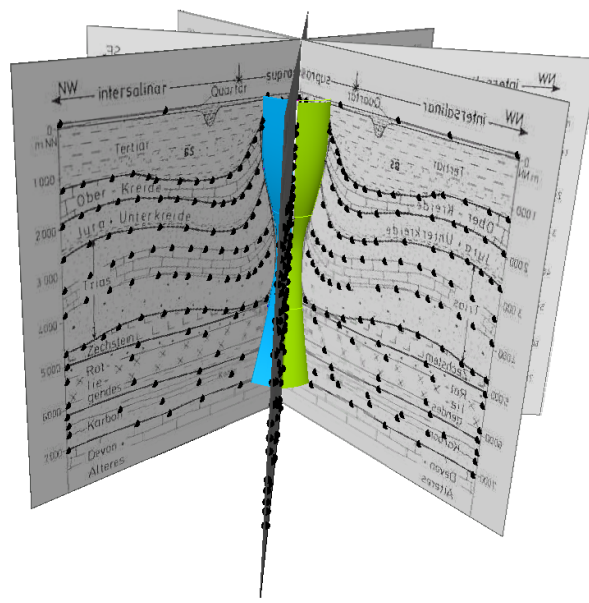
Figure 2: Process of modelling a salt dome by using Method II.

The blue/green cylindrical shape is represented by the faults of the salt dome. The black points represent the horizons of the sedimentary column, which were converted into surfaces in a next step.

The second part of this master thesis investigates in the status quo of literature and research for petrophysical parameters and their influencing factors. Each facies body has specific seismic properties (density, compressional- and sheer wave velocity), which are influenced depending on the rock type by several factors like porosity, shale volume and fluid fill. Typical ranges of seismic properties for different rock types are shown by Schön (2015) and Fjaer et al. (2008). Ranges for dry (gas) and water saturated carbonate rocks (main dolomite and dachstein limestone) are taken from the petrophysical database of the Geophysical Institute of the Montanuniversity of Leoben. Seismic properties are influenced by porosity, shale volume and fluid fill. Athy (1930) showed a nonlinear porosity decrease with depth for sedimentary environments. Density of porous rocks depend on mineral composition, porosity and the density of the pore fluid (Schön, 2015). Decreasing porosity with depth leads to an increase in density and velocity (compressional- and shear wave velocity). Wyllie et al. (1956) showed with the time-average equation a simplified porosity-velocity relationship, which works best for well compacted sedimentary rocks. Schön (1996) implemented an equation for the velocity depth relationship for sediments with a granular structure. Han et al. (1986), Castagna et al. (1985) and Kirchberger (2001) investigated beside porosity the influence of shale volume for water saturated shaly sand formations. Velocities of clastic sediments are strong controlled by the type of grai-grain-contact and cementation – ranging from unconsolidated sand to well cemented sandstone; modeling of this influence is still a problem. Velocity change is the combined effect of elastic moduli and density variation. Compressional wave velocity increases from dry (gas) to kerosene and is highest for water. The opposite happens for shear wave velocity, because fluids have no shear resistance (King 1966). The static Gassman model predicts velocities for a saturated rock with one fluid, for instance water, from the velocities of a saturated rock with another fluid, for instance gas (Gassman, 1951). The increase of velocity with depth is caused by the increased pressure on the rock skeleton (effective pressure).

The results are presented in form of fact sheets for each facies model. They provide an overview of the geometrical inputs of each facies and list ranges of petrophysical parameters which are recommended for petrophysical modeling.

2 Facies Modeling

2.1 **Facies Models**

In case of the channel and submarine fan, facies and their geometry was taken from different literature and used as a guidance for facies modeling. The identified facies and the corresponding measurements are presented in the fact sheets.

For the channel this study investigates on the transition of a braided channel of more proximal areas (close to the origin) to a meandering channel of more distal areas (far from the origin). This transition is represented by different facies and geometries of the channels (changing architecture). To represent this transition, four facies models were defined..

For the salt dome, reef, volcano and karst body, real examples from literature and their profiles were taken for the Facies Models.

2.1.1 **Channel**

<u>Overview</u>

Channels are depressions in the land surface which are formed by the water flow of rivers as part of the fluvial system. Depending on topography, sediment supply, subsidence rate and climate, various river forms and accordingly channel deposits develop. Braided, meandering or straight rivers have only one channel belt, whereas anastomosing rivers consist of multiple interconnected belts, which are separated by areas of floodplain. Makaske (2000) defines a channel belt as a zone including a channel with its bars, abandoned channel segments, levees and crevasse splays and which is laterally bounded by the floodplain (overbank deposits). Meandering rivers have only a single thalweg compared to a braided river that develops multiple thalwegs (Makaske, 2000). The formation of a braided river to a meandering river is controlled by decreasing sediment supply and increasing channel stability.
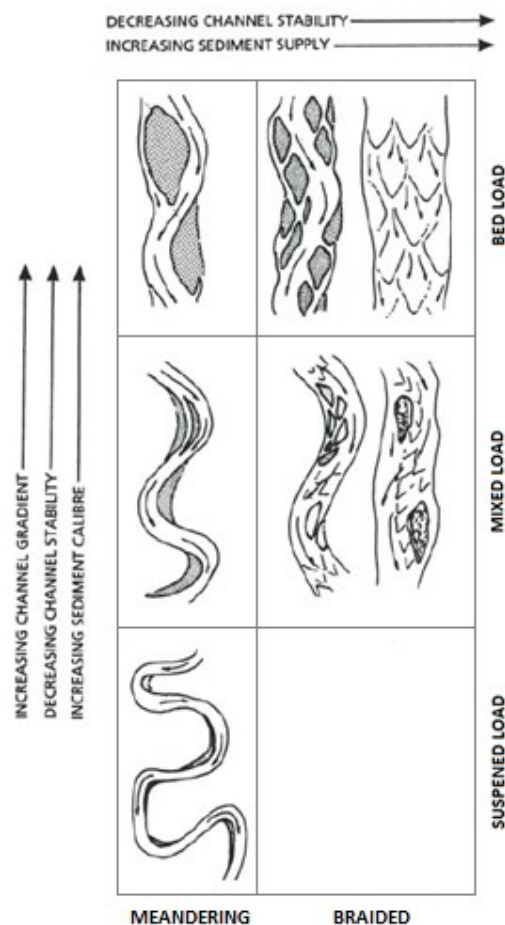
Figure 3: A classification of channel patterns (modified after Schumm, 1985).

Schumm (1985) defined the sediment load as bed load, mixed load and suspended load (Figure 3). Bed load dominated rivers have a high stream power due to a high gradient and can transport a high sediment load of coarse grained sediment. Their fine grained floodplain deposits are sub-ordinate, which leads to a minor channel stability. The transport energy as well as the sediment size of mixed load dominated rivers is decreased compared to those of the bed load system. The channel fill contains between 20 to 40% sand. Floodplain deposits are more common and lead to an increased channel stability, because of the cohesive behavior of the fine grained floodplain sediments. The transport energy of suspended load dominated rivers is very low, therefore the channel fills contain a high proportion of fine grained sediments. (Einsele, 2000; Lord et al., 2009).

Architectural Elements

Bed load, which consists mainly of sand and gravel is deposited as bars in the channel and gives the braided river its typical form (Figure 4). During high water, longitudinal bars (L-Bars) of gravel are deposited in the channel center. During low water, the channel is forced to split and to flow around the L-Bar and transverse bars (T-Bars) of large planar cross-bedded sand bodies develop. From proximal to distal areas the energy of the water flow decreases, which results in a decrease of gravel. In proximal areas (close to the origin) L-Bars (>50% gravel) and in distal areas (far from the origin) T-Bars (<10% gravel) are dominant (Einsele, 2000). Figure 5 shows the depositional architecture of a braided river.
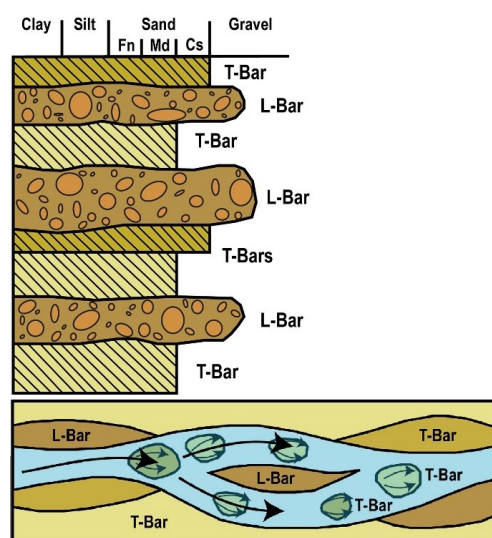
Figure 4: Above: Ideal facies sequence of a braided river deposit.
Below: Aerial view of a braided raided river (Bevis, 2014).
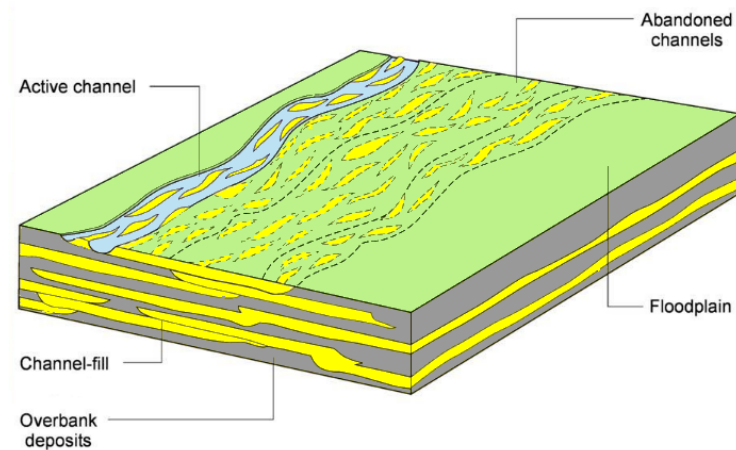
Figure 5: Facies model showing the architectural elements of a braided river (modified after Nichols, 2009).

A meandering river develops its form by erosion of the outer bank (high energy) and deposition on the inner bank (low energy). The deposition on the inner bank leads to the formation of point bars. Meandering rivers transport and deposit a mixed load of suspended and bed load (Nichols, 2009). The coarsest material is carried on the channel floor and finer material in shallower parts of the flow, which leads to a deposition of a fining upward profile (Figure 6).
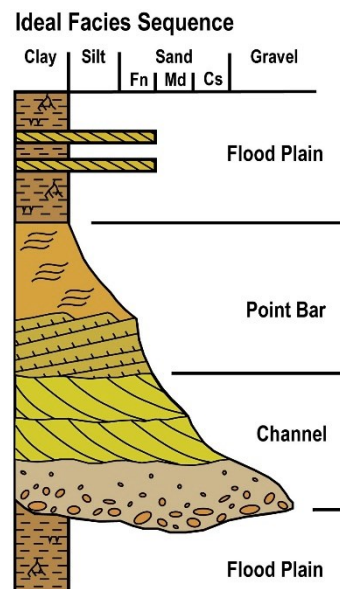
Figure 6: Ideal facies sequence of a meandering river deposit (Bevis, 2014).

Figure 7 shows the elements of a meandering river. Levees are banks of sediment at the edge of the channel and are higher than the floodplain. They are formed during moderate floods, where sand is deposited near the channel and is grading into silt and mud due decreasing flow velocity.

8

When the levee breaks water and sediment is carried out onto the floodplain and upward coarsening lobes of sand and silt develop (Nichols, 2009).
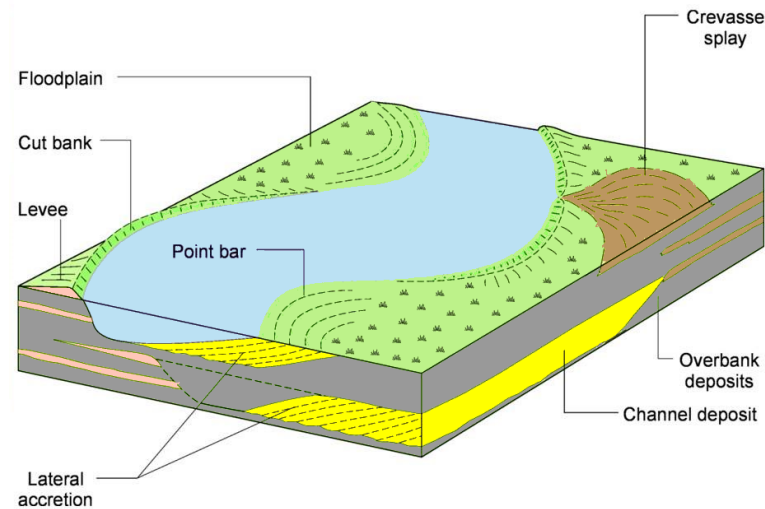
Figure 7: Facies model showing the architectural elements of a meandering river (modified after Nichols, 2009).

The architecture of fluvial deposits is defined as the three-dimensional arrangement of channel and overbank deposits (Figure 8). The architecture is mainly influenced by avulsion, subsidence and sediment supply. The avulsion of the channel affects the lateral migration. Less frequent avulsion, which is typical for braided rivers (bed load dominated rivers) leads to a more lateral migration and therefore to a higher width/depth-ratio (>40). More frequent avulsion is common in meandering rivers (mixed load dominated rivers), where less lateral migration leads to a lower width/depth-ratio. The width/depth-ratio of suspended load dominated rivers is even less than 10% (Einsele, 2000). Fast subsidence rate will result in an increased aggradation of floodplain (overbank) deposits compared to a slow rate.
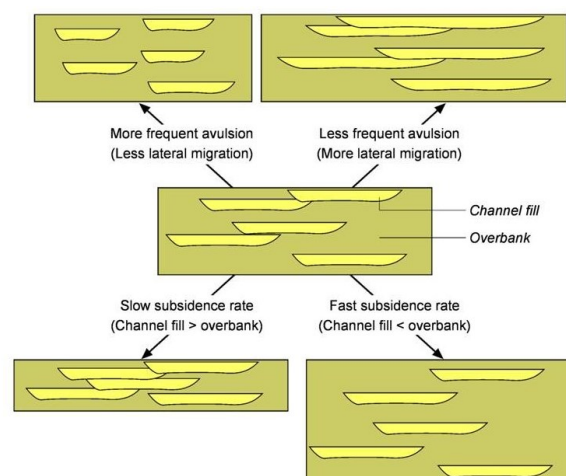
Figure 8: The architecture of fluvial deposits is determined by the rates of subsidence and frequency of avulsion (Nichols, 2009).

Hornung and Aigner (1999) show an example of the architectural elements of fluvial deposits, their characteristics, geometry and lithology (Figure 9).
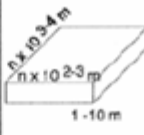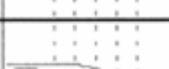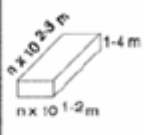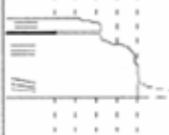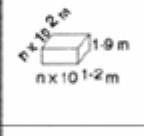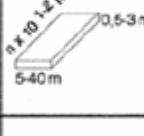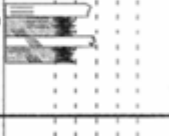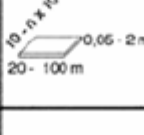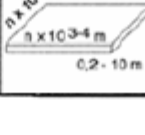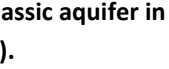
element	characterization	geometry	lithology
Channel (bed load)	Coarse-grained sandy bedforms, multilateral and multistory amalgamated channel complexes. Weakly developed fining-up trends.	$n \times 10^{3-4}$ m, $n \times 10^{2-3}$ m, 1-10 m	
Channel (mixed load)	Often massive sandbodies. Also alternating layers of silty, fine-grained and coarse-grained sandy bedforms. Clear fining-up trends.	$n \times 10^{2-3}$ m, 1-4 m, $n \times 10^{1-2}$ m	
Channel (suspended load)	Consists mainly of silt and clay. Rarely thin fine-grained sandy bedforms. No visible fining-up trends.	$n \times 10^2$ m, 1-9 m, $n \times 10^{1-2}$ m	
Lateral accretion	Inclined, alternating layers of silt and clay with fine-grained and coarse-grained sandy bedforms, often irregular bedding contacts. Clear overall fining-up trend.	$n \times 10^2$ m, 1-9 m, $n \times 10^{1-2}$ m	
Levee	Inclined layers of sand, alternating with silty fine sands. Often overall coarsening-up trend.	$n \times 10^{1-2}$ m, 0,5-3 m, 5-40 m	
Crevasse splays + sheet floods (LS)	Very coarse to fine sands. Could be amalgamated to thicker packages. Ripple crossbedded or low-angle crossbedded. Bedforms mostly missing. Mostly clear fining-up trends.	$10 - n \times 10^2$ m, 0,05 - 2 m, 20 - 100 m	
Floodplain, Paleosols Overbanks	Horizontal laminated clay and silt. Contains ± developed paleosols, desiccation cracks.	$n \times 10^{3-4}$ m, $n \times 10^{3-4}$ m, 0,2 - 10 m	

Figure 9: Architectural-element analysis from a field study of a Triassic aquifer in Germany (modified after Hornung and Aigner, 1999).

2.1.2 **Submarine Fan**

A submarine fan is deposited by mass-flow processes, mainly turbidity current, on the sea floor as lobe structure (Nichols, 2009). The main architectural elements of a submarine channel are channels and depositional lobes. Channels often consist of levees and incise into the lobes. The deposits are normally coarse sands and gravels that are characterized by the Bouma sequence. The levees are the overbank flow from the channel and consist of fine sand, silt and mud that spreads out as a fine grained turbidity current away from the channel. Lobes are placed at the end of the channel, where the turbidity current spreads out. The succession is typically a coarsening-up and thickening-up succession (Figure 10) and is often tens to hundreds of meters thick. The lobe deposits often represents a complete Bouma sequence.
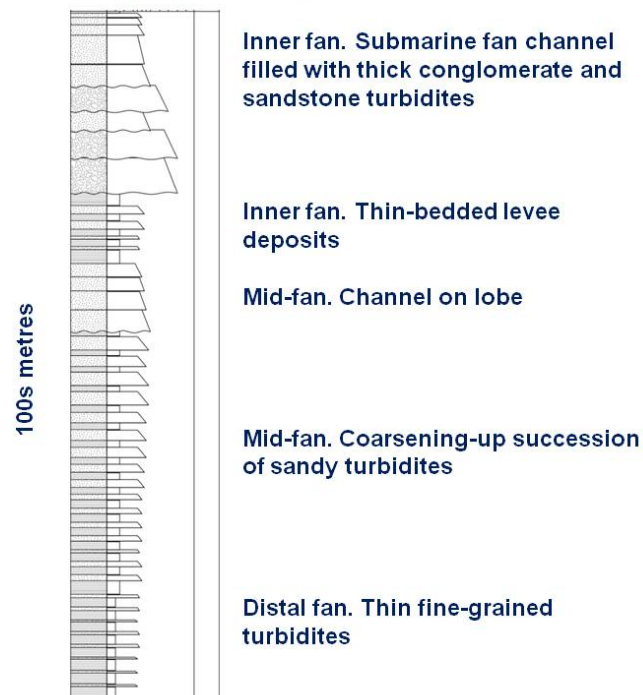
Figure 10: Profile through submarine fan deposits with proximal- (inner), mid- and distal fan deposits (modified after Nichols, 2009).

The geometry of the lobes depends on the grain size of the supplied material (Nichols, 2009). Most common are the gravel-, sand-, mixed sand and mud, and mud fan deposits. In case of sand-rich system more than 70% of the deposits need to be sandy material. This sand content is the lower limit for a major change in the seismic character and facies architecture of deep marine turbidite systems (Reading and Richards, 1994). Therefore, this thesis concentrates on the sand-rich systems (Figure 11). Sandy material normally originates from sand-rich shelves where

the material was sorted from waves and storms. The lobe is often less than 50km in radius, because sand-rich turbidity currents have a lower transport efficiency. This also leads to an abrupt transition between proximal, mid and distal lobes.
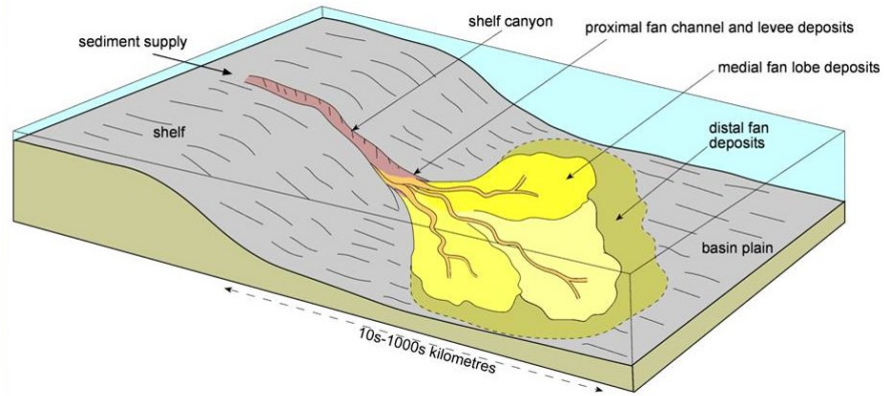
Figure 11: Facies model showing the architectural elements of a sand-rich submarine fan (Nicoles, 2009).

Prelat et al. (2009) showed a hierarchical scheme of the lobe architecture (Figure 12).
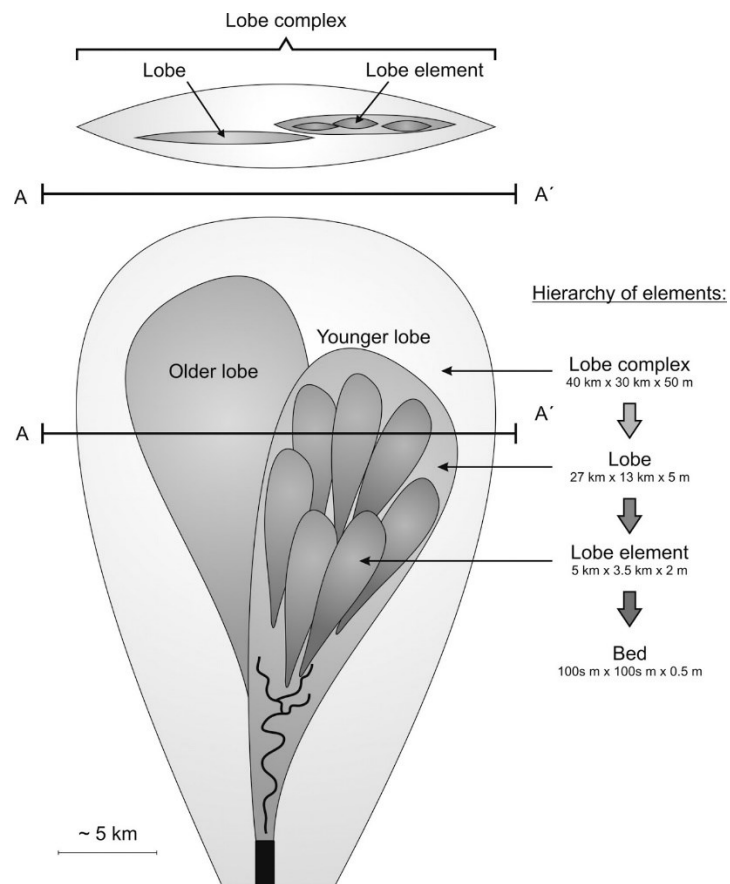
Figure 12: Hierarchical scheme of lobe deposits (Prelat et al., 2009)

2.1.3 **Salt Dome**

Salt domes vary on a wide scale (Figure 13) between immature, irregular massives and mature, jetlike stocks (Jackson and Talbot, 1986). Mature salt domes can reach diameters up to 10km like in Iran and their symmetry is highly variable. Figure 14 shows three examples of different salt stock symmetries from Louisiana. The Oakwood dome is a subcircular stock with small size (10 km²), symmetrical overhang, vertical axis and orthorhombic symmetry. The as well subcircular and of small sized (10 km²) Steen dome has an inclined stock. The small (6 km²) Mount Sylvian stock has an elliptical stock with multiply overhangs and no symmetry.
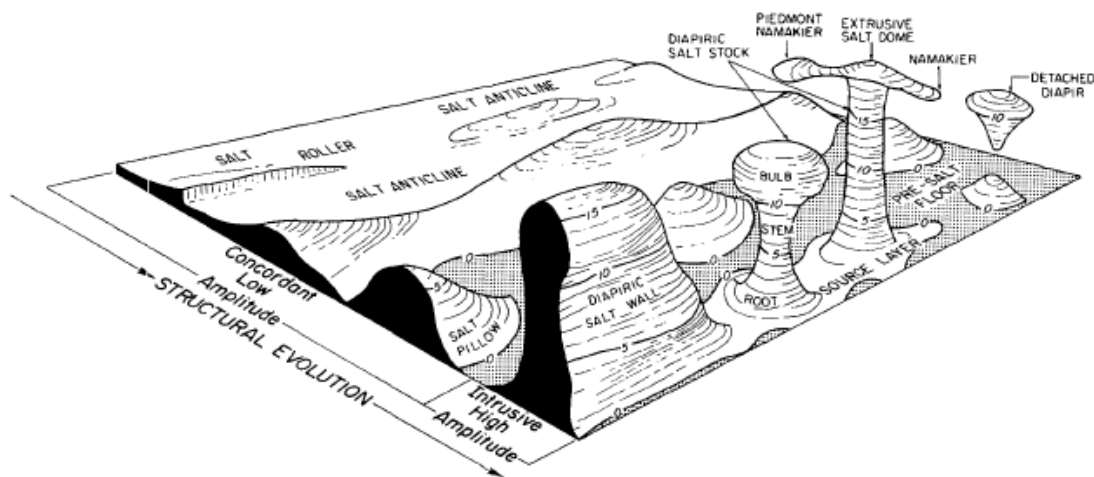
Figure 13: The main types of large salt structures (Jackson and Talbot, 1986).
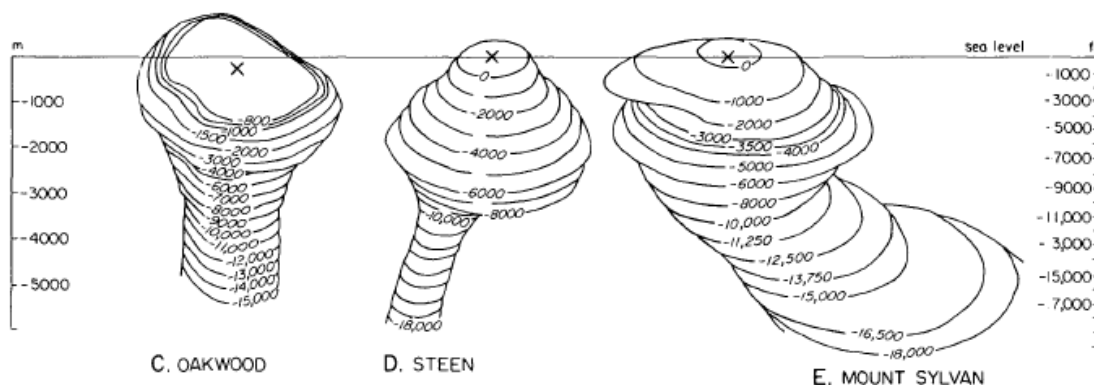
Figure 14: Three salt diapirs in south Louisiana (modified by Jackson and Talbot, 1986 from Jackson and Seni, 1984).

Most sediments have lower densities than salt, because they compact, dehydrate and cement with increasing burial. Salt in contrast remains almost incompressible throughout burial (Jackson

and Talbot, 1986). Arrhenius (1912) first described the simplest natural case of salt dynamics of the buoyant rise of salt into a laterally uniform overburden.

Ortlam (2001) published a salt dome of the Bremerhaven surrounded by a sedimentary column (Figure 15), which is comparable in dimensions to the Oakwook stock from Louisiana.
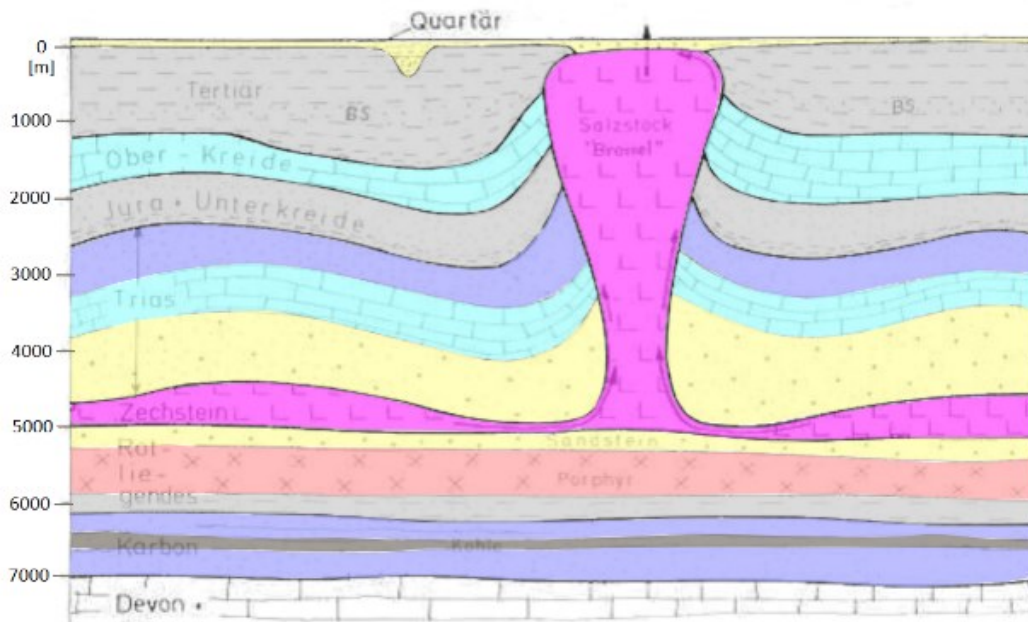
Figure 15: Profile through the salt dome "Bramel" (pink) from Bremerhaven in Germany (modified after Ortlam, 2001).

2.1.4 **Reef**

Reefs are wave resistant carbonate bodies that are build up of benthic organisms (like corals) and are formed in shallow waters (Nichols, 2009). Typical modern reef settings are the barrier reef, fringing reef and patch reef (Figure 16). The barrier reef is a linear reef form parallel to the shoreline. It forms offshore and protects the lagoon behind. A fringing reef is built on the coast-line and a patch reef (atoll) is formed isolated on a seamount.
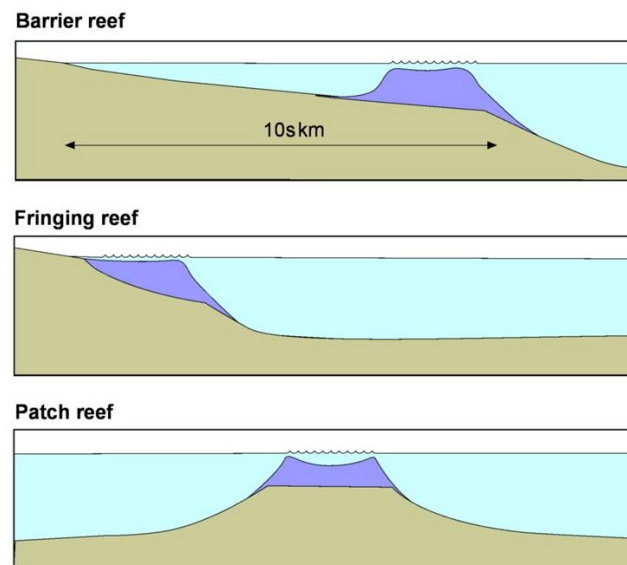
Figure 16: Typical reef forms from top to bottom: barrier reef, fringing reef and patch reef (Nichols, 2017)

Pomar (2004) investigated on the different lithofacies of a reef (Figure 17). The reef core is also referred as the high energy zone, where robust coral structures (grainstone and packstone) with-stand the force of waves. Behind the reef crest, in the outer lagoon, conditions become gradually quieter from outer to inner lagoon with a final deposition of mudstone/wackestone. The forereef is the result of the break up of the core material by waves, which leads to a slope (10°-30°) that is build up of dipping packstone and wackestone that passes into fine grained open shelf deposits.
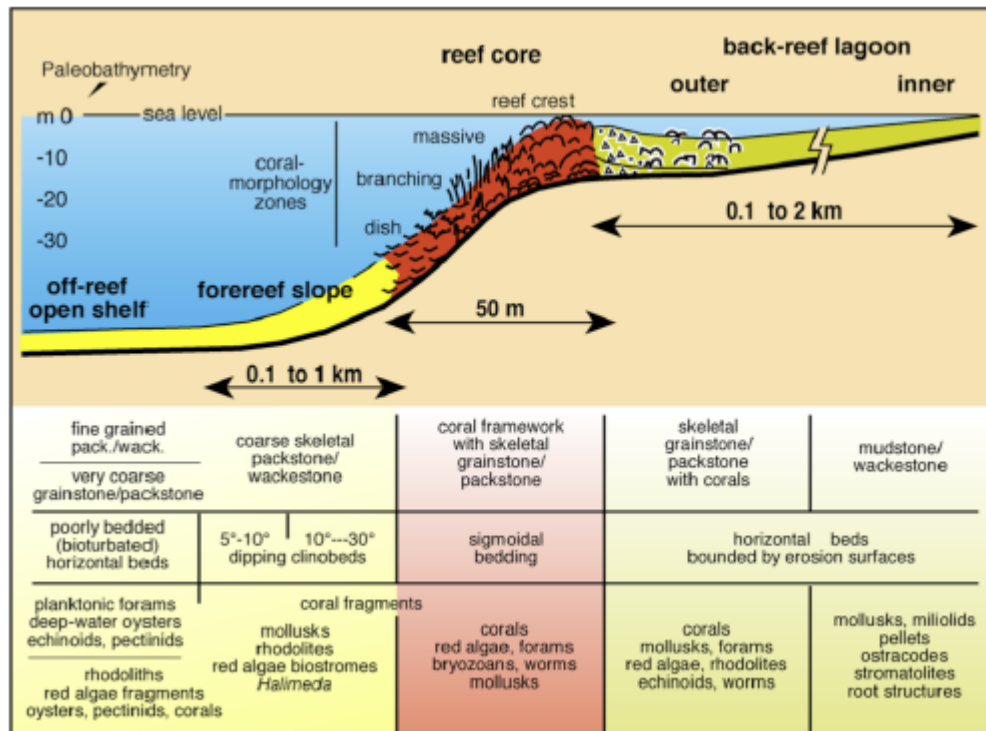
Figure 17: Lithofacies distribution in a reef complex (Pomar, 2004).

Figure 18 shows a carbonate mound that consists of a "mound stage" and an "atoll stage" on top. A carbonate mound is an ancient crudely bedded fine crystalline carbonate (modern examples are rare) (Nichols, 2009). The lithofacies of the "atoll stage "corresponds to the lithofacies of a typical reef complex (Figure 17).
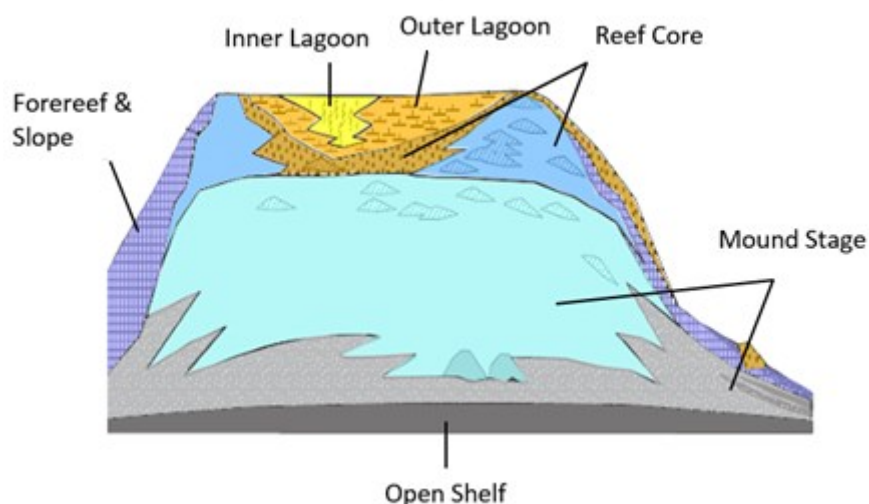
Figure 18: Modified profile (two times vertically exaggerated) through a carbonate mound from the middle Frasnian carbonate platform in Belgium, consisting of a "mound stage" and an "atoll stage" on top. (modified after Da Silva, 2004).

2.1.5 **Volcano**

This study investigates on stratovolcano, which is the classic form of a steep conical mountain with a vent in a crater. It is a composite body that results from alternating eruptions of pyroclastic flows and lava flows. The eruptions typically result from intermediate to acidic magmas. Deposits close to the volcanic center are normally ash fall products of Plinian eruptions and welded pumiceous tuffs resulting from ignimbrites. Further away ashes become reworked and form lahars and finally become mixed with terrigenous material (Nichols, 2009).

Bogie and Mackenzie (1998) point out that the major lithological divisions in volcanic facies are between lavas, pyroclastics and epiclastics. Lavas are characterized by thickness and autobracciation, whereas the main features of pyroclastics are bed thickness and size of the clasts. Regarding epiclastics mass flow deposits need to be distinguished from fluviatile deposits. Bogie and Mackenzie (1998) define four facies for an andesitic stratovolcano (Figure 19). The central zone is close to the vent and can be found up to 0,5km to 2km. The proximal zone is a mixture of lava and pyroclastics flows and extends 5 to 10km from the central vent. In the medial facies pyroclastics dominate over lavas and the facies is located 10 to 15km from the vent.
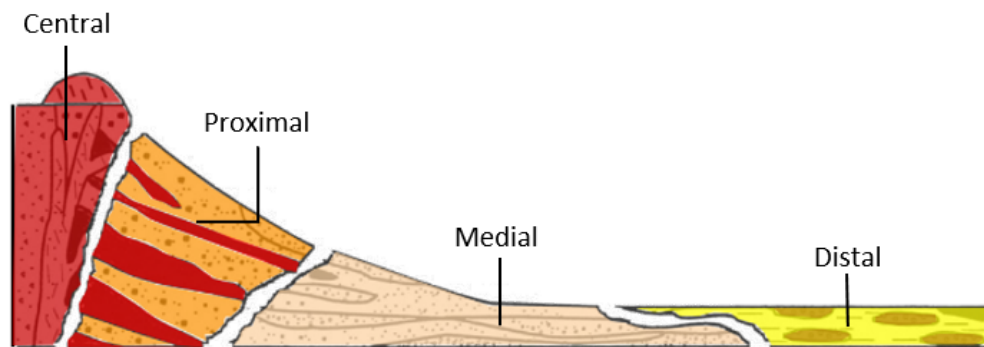
Figure 19: Facies model of an andesitic stratovolcano, represented by four main facies zones (central, proximal, medial and distal) (Bogie and Mackenzie, 1998).

2.1.6   **Karst**

Karst areas are characterized by sinking streams, caves, enclosed depressions, fluted rock out-crops, and large springs. Important factors in the formation of karst are rock structure and lithology such as massive, pure, and coarsely fractured rocks (Ford and Williams 1989). In karst hydrological three porosity types can be distinguished (Kiraly, 1975; Palmer, 1999). The matrix, the fracture and the cave (solution) porosity. The matrix porosity is the result of sedimentation and diageneses and consists of intergranular pores. The fracture porosity results from late diagenesis, tectonism and weathering. The cave porosity is defined by the diameter of the cavity greater than 0,5m and results from speleogenesis (Curl, 1986). The Buda Thermal Karst System originally consists of six large caves (50 to 130m wide and more than 1km long) (Figure 20). Depending on the location "main dolomite" and/or "dachstein limestone" is present.
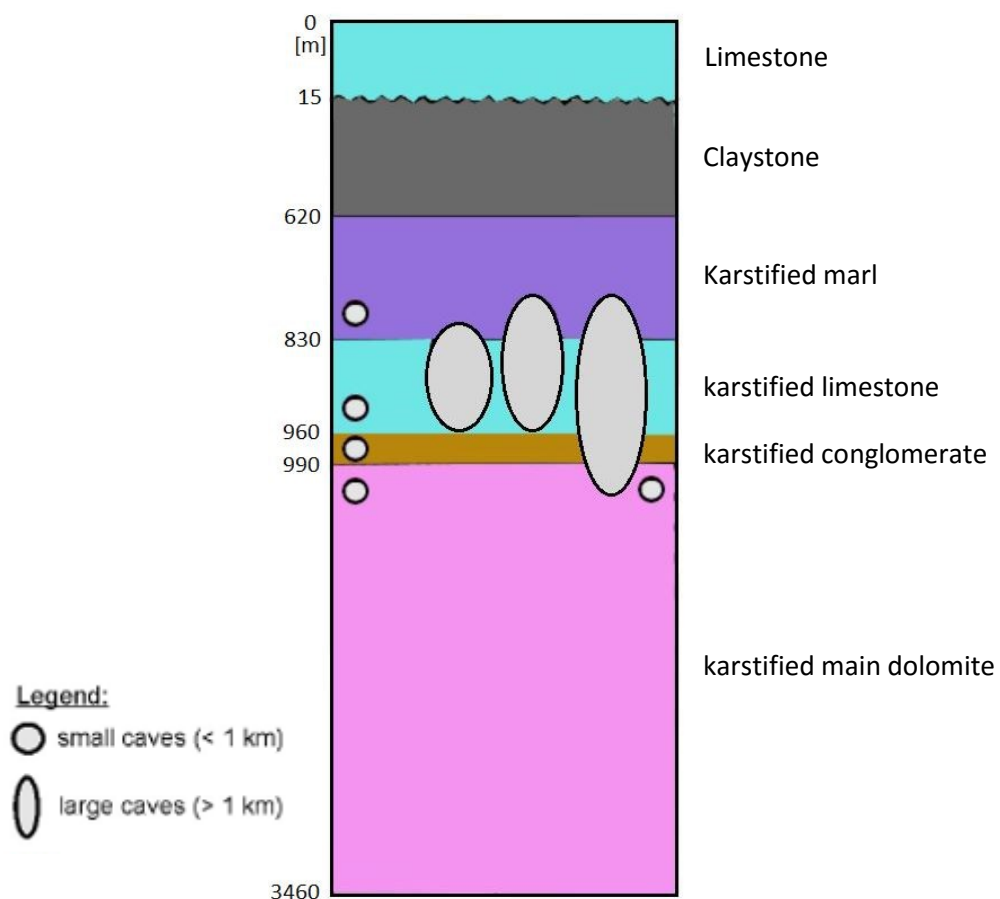
Figure 20: Lithological column of the Buda Thermal Karst System (Hungary) in the Rozsadomb area; caves are marked as circles (modified after Virag e t al., 2013).

2.2 Facies Modeling Methods

2.2.1 Stochastic Methods

Cell-based Methods

Cell-based methods are differentiated in two-point statistics and multi-point statistics. Traditional two-point statistics ("Sequential Indicator Simulation", "Truncated Gaussian Simulation") require the existence of upscaled well data to estimate the unknown data of the interspace between the wells (unsampled location). The degree of linear correlation between the two points is provided by the variogram (Goovaerts, 1997). Two-point statistics fail to capture common geological features like curvilinear shapes (meandering channel or mound) and cannot capture transitional trends (except "Truncated Gaussian Simulation") (Pyrz et al., 2014). Multi-point statistics allow the simulation of complex, non-linear spatial relationships by using patterns obtained from training images. Compared to two-point statistics, multi-point statistics allow the reconstruction of sedimentary environments like fluvial systems (Strebelle and Zhang, 2004), turbidite reservoirs (Strebelle et al., 2003) and carbonate platforms (Levy et al., 2008), but still do not reflect clean geometric shapes. In case of cell-based methods upscaled well data is required for facies modeling and the resulting facies can only be influenced by statistics (variogram or training images). Because no well data is existing for this study and an exact geometrical definition is required, other methods are preferred for facies modeling.

Object-based Methods

Object-based methods place predefined three-dimensional facies bodies (objects) stochastically and sequentially within a background facies as long as a defined proportion of objects is achieved (Pyrz et al., 2014). The geometry of the facies bodies can either be defined deterministically or stochastically. There are several possibilities for object shapes and their geometrical modifications as well as the option to link objects to each other. The resulting facies shows accurate geological shapes and realistic idealized nonlinear continuity that reflect outcrops and modern analoges. With object-based methods stochastically distributed sedimentary structures can be easily generated without data conditioning from wells. Petrel software provides such a method called "Object Modeling", which gained wide popularity in modeling fluvial systems. The software already provides a straight forward step by step workflow for modeling channels. The

first facies is set as the impermeable floodplain, which is defined as the background. The second facies type is the channel sand. The third facies type the levee sand and the fourth the crevasse splay. For each facies type fractions can be defined and facies are populated within the background facies according to the proportion. For modeling lobes, the software provides a body shape called fan lobe with predefined parameters that contribute to a lobe. "Object Modeling" has the opportunity to link facies to each other it fails for complex internal structures like the reef that consists of six different facies types which need to be in a specific order and place.

2.2.2 Deterministic Methods

Interactive Facies Modeling

Interactive Facies Modeling can be used to paint deterministic facies bodies, with tools like a pencil, brush or airbrush, directly into the 3D grid (Schlumberger, 2015). When using it as a stand-alone method, it is more suitable for simple bodies like a channel, than for bodies that have a complicated architecture build up by several different facies types. But it can be used as a simple tool to add facies do an already existing facies model.

2.3   **Method I - "Object Modeling" Workflow**

Due to the good applicability of "Object Modeling" for fluvial and lobe system, four fluvial channels (two braided rivers and two meandering rivers) and one submarine fan were created with this method. To populate the facies within a 3D grid a training image was created and a background facies was assigned to the grid. Several facies bodies are provided by "Object Modeling" and their geometry can be defined. For channels the software offers an own body shape, to define the sinuosity, wide and depth as well as the levee of the channel. For each facies body fractions can be defined.

The general workflow of creating a facies model by Method I is shown by Figure 21 and explained by the step by step process of modeling a fluvial channel. Alterations of modeling a submarine fan are pointed out.
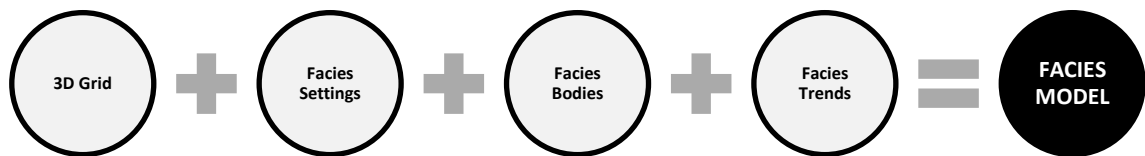
Figure 21: Workflow of Method I

2.3.1 **3D Grid**

To populate the different facies bodies along the 3D grid a simple training image grid was created. Therefore, the number of cells, cells size and the origin was defined. The cell size limits the resolution of the 3D grid. The generated 3D grid is a cuboid with an area of 1000m x 1000m and a height of 100m (Figure 22).
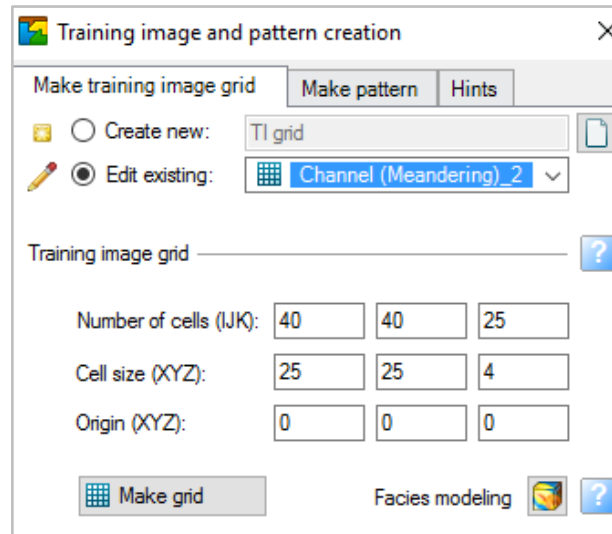
Figure 22: Training image with defined cell numbers, cell size and origin.

For the 3D grid of the submarine fan an area of 5000m x 5000m was defined by using the same cell size of 25m, but 200 cells instead. The height of the cuboid was defined as 100m.

2.3.2   **Facies Settings**

The modeling of a fluvial channel is an already provided workflow by the "Facies Modeling" process. The software provides four main facies types that build up a typical fluvial channel. These facies are the channel fill, the levee, a possible crevasse splay and the background as the floodplain (Figure 23).
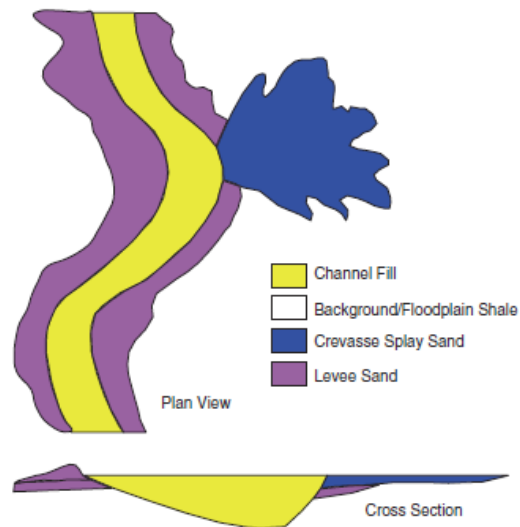
Figure 23: Geometry of a fluvial channel with main facies types (Pyrc at al., 2015).

The facies were named after the facies type and the facies fill. In case of the channel the facies type was defined as "Channel" and the facies fill as "Mixed Load" and therefore the final name is "Channel Mixed Load". Every facies was defined by a specific color and code (Figure 24).

Figure 24: Defined settings for the fluvial facies types.

2.3.3 **Facies Bodies**

The definition of the background facies is the last step before populating geometrical bodies (Figure 25). Everything that is not a geometric body is defined as the background. In case of the fluvial channel the background was defined as the floodplain with a constant distribution of shale.
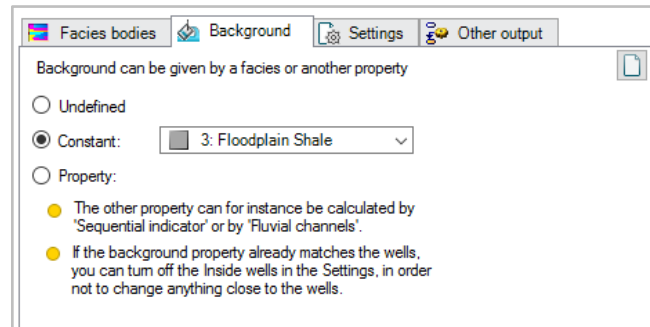
Figure 25: Floodplain defined as the background facies.

Channels and lobes were defined as the main facies bodies (Figure 26). The channel was added by a function called "add a new channel" and automatically named as "Fluvial channels". The lobe was added by "add a new geometric body", but its shape was defined in a later step.

Then the facies types were assigned to the facies bodies. The channel is made up of two facies types called "Channel Mixed Load" and "Levee Fine Sand" (Figure 27). The geometrical measurements that were assigned to the channel, under the layout and section tab, and the levee, under the levee tab, are shown in Figure 28 to Figure 30. The facies model with the floodplain as the background and the inserted channels and levees is shown in Figure 31.
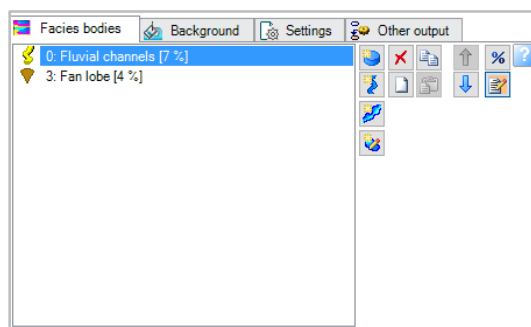
Figure 26: "Fluvial channels" and "Fan lobes" defined as the two different facies bodies.
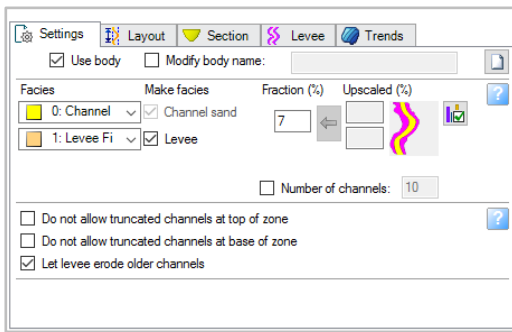
Figure 27: "Channel Mixed Load" and "Levee Fine Sand" facies as part of the "Fluvial channel" facies body together make up a fraction of 7%.
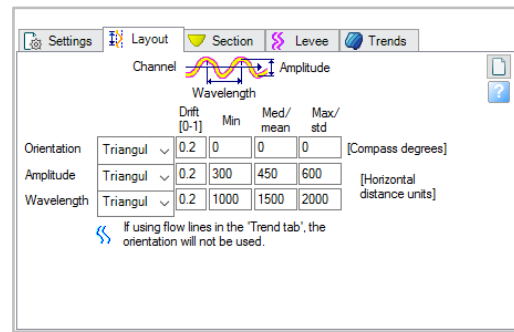
Figure 28: Defined measurements for the channel orientation, amplitude and wavelength using a triangular distribution.
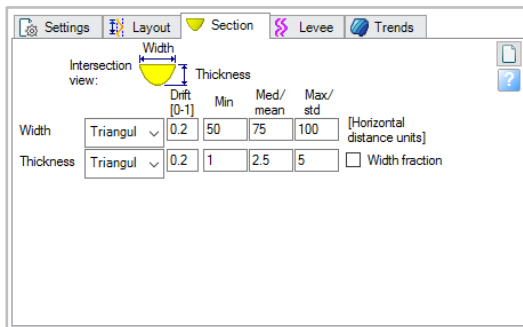
Figure 29: Defined measurements of the channel width and thickness using a triangular distribution.
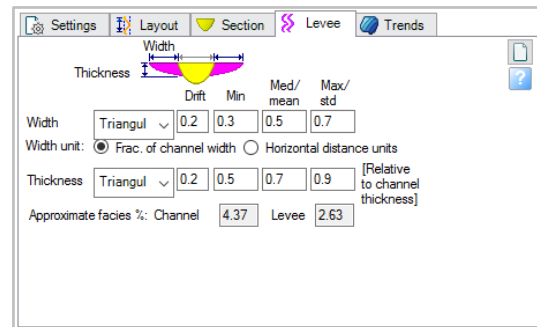
Figure 30: Defined measurements of the levee width and thickness using a triangular distribution.
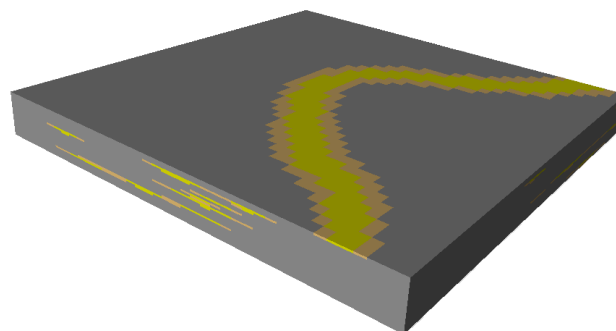
Figure 31: Facies model of the channel (yellow) and levee (rose) inserting the floodplain (grey).

The facies type "Crevasse Splay sand" is assigned to the lobe body (Figure 32). Under the geometry tab the body shape was chosen as "Fan lobe" and the radial profile as "Rounded" (Figure

33). To replace all facies (floodplain and levee) except the "Channel Mixed Load" by the "Crevasse Splay Sand" a rule was applied (Figure 34). The final facies model including all facies types of the meandering river is shown in Figure 35.
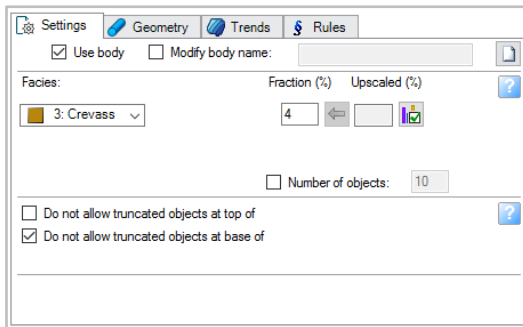
Figure 32: The facies "Crevasse Splay" assigned to the "Fan Lobe" facies body makes up a fraction of 4%.
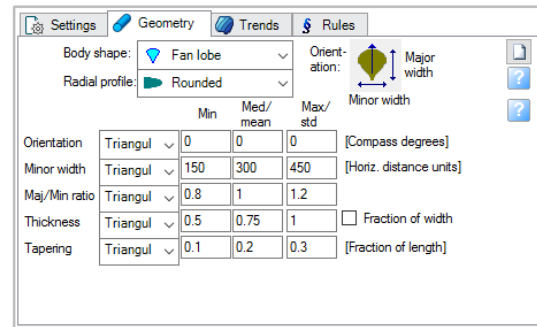
Figure 33: Defined measurements for the fan lobe width and thickness using a triangular distribution.
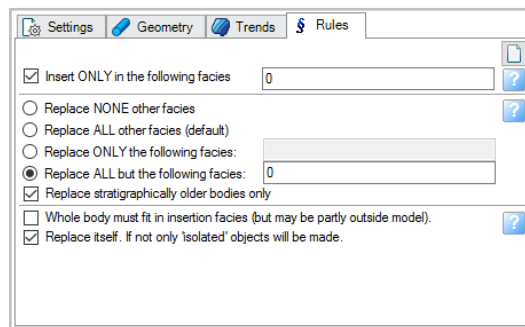
Figure 34: Defined rule to replace all but the channel facies coded with "0".
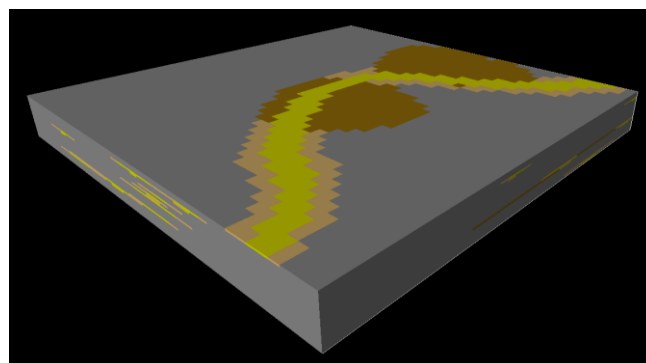
Figure 35: Final facies model of the meandering river.

The submarine fan consists of three different facies bodies. One distal fan lobe, several mid fan lobes that occupy a fraction of 20% and fluvial channels with a fraction of 10%.

2.3.4 Facies Trends

To influence the distribution of the facies bodies either in vertical or horizontal direction, trend maps can be inserted. In case of the channel no additional trend was included. Therefore the application of a trend map is shown by the lobes of a submarine fan (Figure 37). In this case a linear trend was inserted to model the increase of lobes with increasing depth. This trend should reflect the coarsening up succession of sandy turbidites. The trend was inserted under the vertical trend of the trend tab in the "Facies Modeling" process.
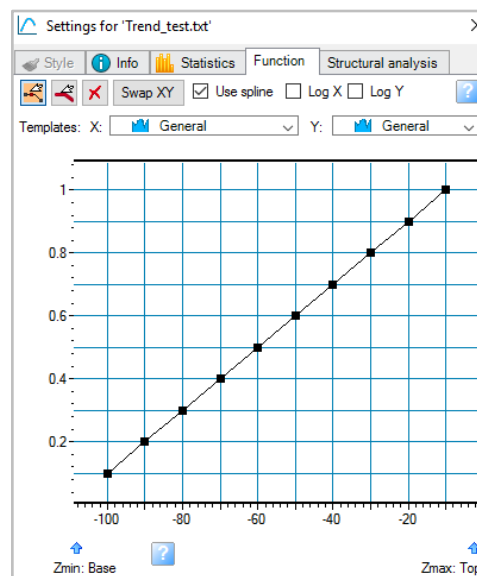
Figure 36: Increasing vertical trend from bottom of the 3D grid at a depth of -100m to top of the 3D grid at a depth of 0m.

2.4 Method II - "Radial Module Process" Workflow

To model the complex architecture of a salt dome, reef, volcano and karst body none of the existing methods work properly and therefore a new workflow (Method II) was invented. The concept of Method II is based on creating a classical geological model by picking faults and horizons in 3D. Instead of a 3D seismic, a profile of a geological body was used for modeling. Therefore, several pictures of the same profile were placed in space around the center or a fixed point of the profiles. This automatically limits this method to almost symmetrical profiles and at the end to symmetrical facies models, which needs to be considered. Boundary modeling is defined as the interpretation of vertical (faults in case of geological modeling) and horizontal boundaries. Vertical boundaries are then transformed to a fault model, which is used for pillar gridding to generate a 3D grid. For each main facies one 3D grid is required. Horizons are transformed to points and then to surfaces, which are used for the internal layering. The workflow is therefore called "Radial Module Process", because boundaries (faults and horizons) are interpreted "radial" around the profiles and the final facies models are build up of several grids per facies (="module"). In case of the salt dome a fault model was created for the salt dome itself and horizons were picked along the sedimentary column. Two 3D grids were created, one for the salt dome and one for the sedimentary column. The fault model of the volcano represents the vertical boundaries between the main zones (central, medial, proximal and distal), from which four 3D grids were generated. For each zone of the reef 3D grids were generated, whereby for some zones two 3D grids were required because of stacked facies. No fault model was created for the karst body, which consists of only one 3D grid by defining the external boundary. In this case the facies is defined by the interpreted horizons only.

Each step of Method II is described and represented by modeling of a volcano. Variations in modeling other facies bodies are pointed out and explained. To create the final facies model the workflow of Method II is presented in five steps (Figure 37):
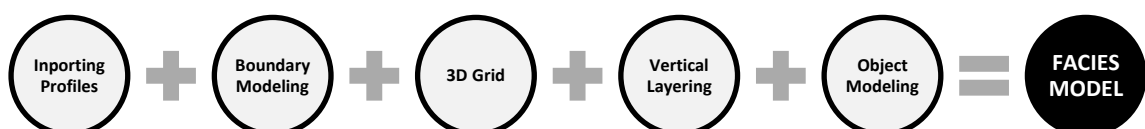
Figure 37: Workflow of Method II.

2.4.1 Importing Profiles

As a first step pictures of the same profile of a geological body were imported and aligned around the center to set a framework and the basis for modeling the geological body. After importing the profiles the measurements of each profile and the direction in the room were defined (Figure 38). To assign coordinates to the corners of the profile "Located in the World" was selected. Easting is expressed as the x-coordinate, northing as the y-coordinate and the depth as z-coordinate. The "Origin" of the center was selected, which represents the location around which the profiles can be aligned. In case of the volcano the center was represented as the left edge of the profile (Figure 38; Figure 39).
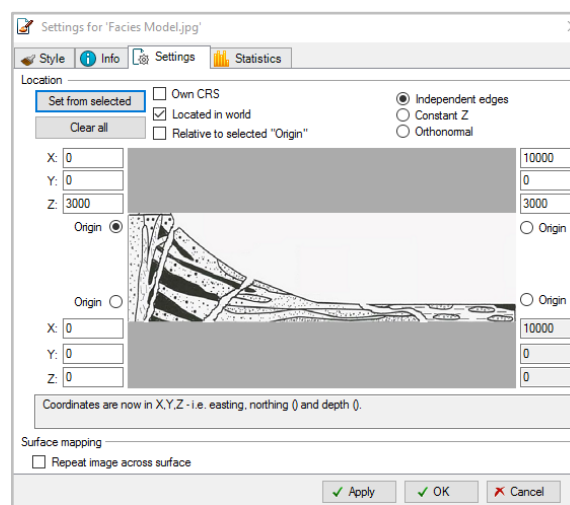
Figure 38: Profile of a volcano with defined measurements and directions in the room, displayed along the positive X-axis. The left lower corner of the profile was defined as zero (left lower corner: X=0, Y=0, Z=0), the height of the center of the volcano as 3000m (left upper corner: X=0, Y=0, Z=3000) and the length of the volcano from center to the edge as 10000m (right upper corner: X=10000, Y=0, Z=3000).
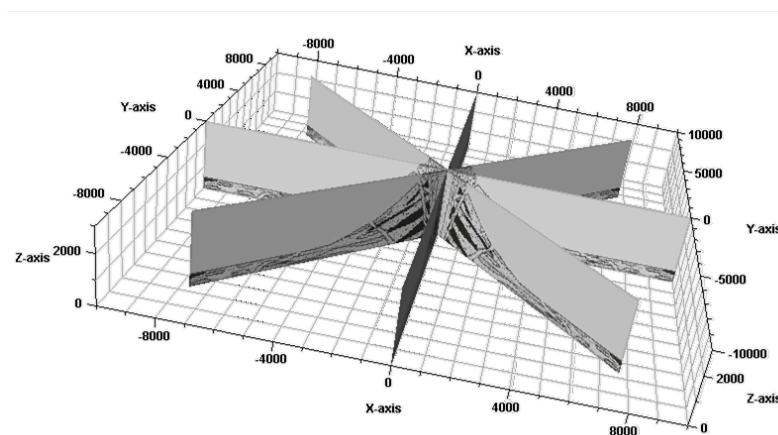
Figure 39: Eight equal profiles of a volcano placed 45 degrees to each other around the center.

For modeling the reef, the profile was cut in half to create two profiles, because of the asymmetry of the reef (Figure 40). A reef shows a slightly different architecture depending on its direction to the sea or landwards. Therefore, each of the two profiles were aligned four times around the center and equal profiles were neighbored to each other. The profiles were stretched and squeezed to create a slightly asymmetrical body.
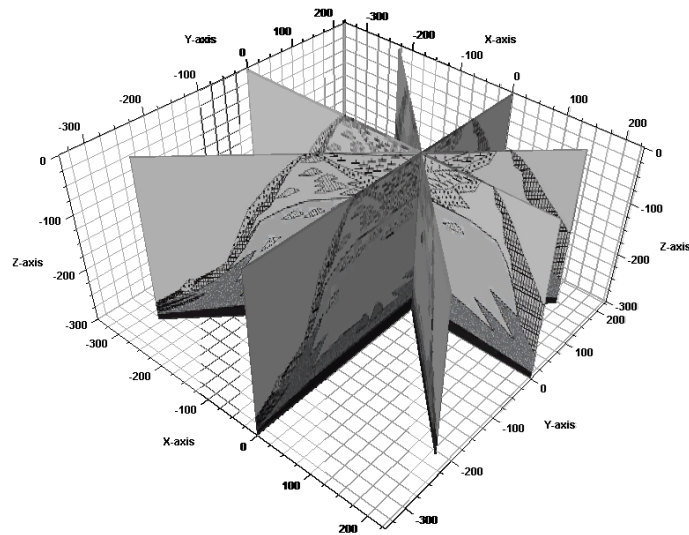
Figure 40: Eight stretched and squeezed profiles of a reef placed 45 degrees to each other around the center.

2.4.2 Boundary Modeling

Fault Modeling is the process of interpreting faults and converting them to a Fault Model. This concept was used for Method II, but was named Boundary Modeling instead, because it is the interpretation of facies boundaries instead of faults. For modeling vertical boundaries the same concept as for Fault Modeling was applied. Modeling horizontal boundaries differs by converting the interpreted horizontal boundaries to points and surfaces at the end, instead of creating a Fault Model.

Modeling vertical boundaries:

To understand the concept of modeling vertical boundaries the general architecture of a volcano is shown by a profile in Figure 41. The volcano is divided in four main zones (central, proximal, medial and distal). Each zone is represented by a different facies type. To represent these different facies in the final facies model the zones were first interpreted by faults along the vertical facies boundaries (Figure 42).
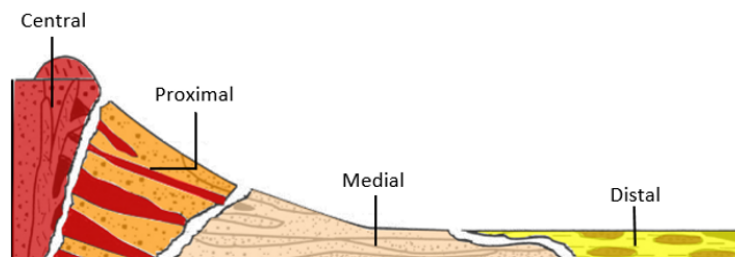
Figure 41: Profile of an andesitic stratovolcano (modified after Bogie et. al, 1998).
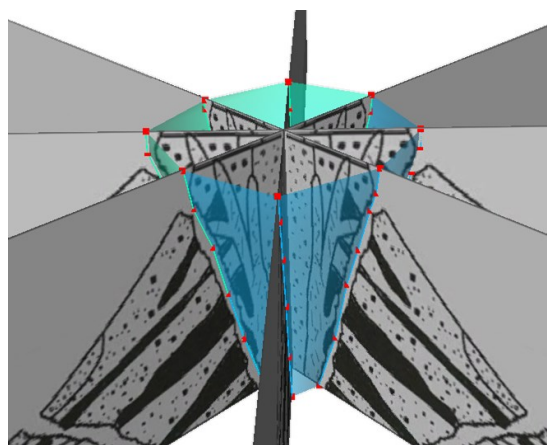
Figure 42: Two interpreted faults (blue and green) around the central zone of a volcano.

Next step after fault interpretation was the creation of a Fault Model. This process is called "Convert a fault in the active fault model" and was applied for each fault. Therefore, the pillar type was defined as a curved pillar to represent the faults best. It is a curved line described by five points along which the different pillars are connected. Created key pillars often do not match the interpreted faults (Figure 43), therefore the fault model was edited by manipulating pillars and adjusting them to the interpreted faults. After the key pillars matched the interpreted faults, both faults were joined by highlighting and connecting the outer two key pillars of each fault (Figure 44). The final Fault Model of the volcano is shown in Figure 45.
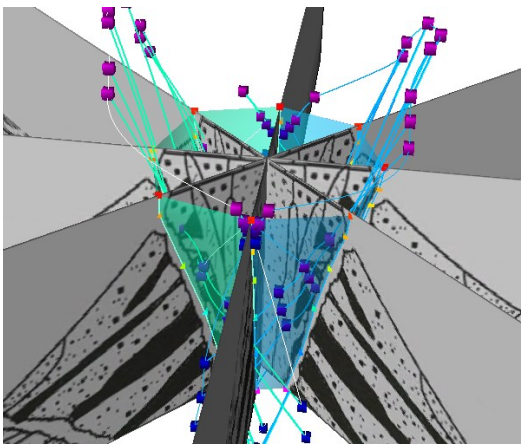
Figure 43: Key Pillars before editing the fault model of the central zone of a volcano.
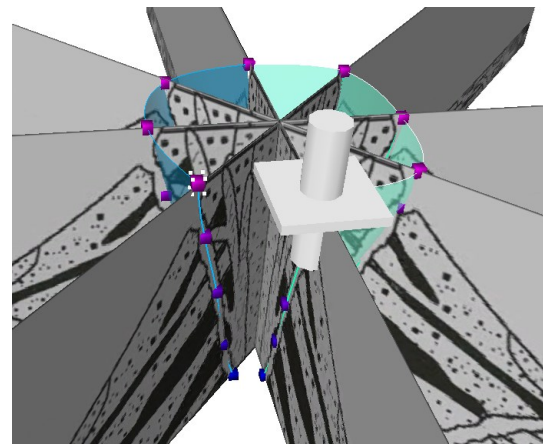
Figure 44: Key Pillars after editing the fault model of the central zone of a volcano.
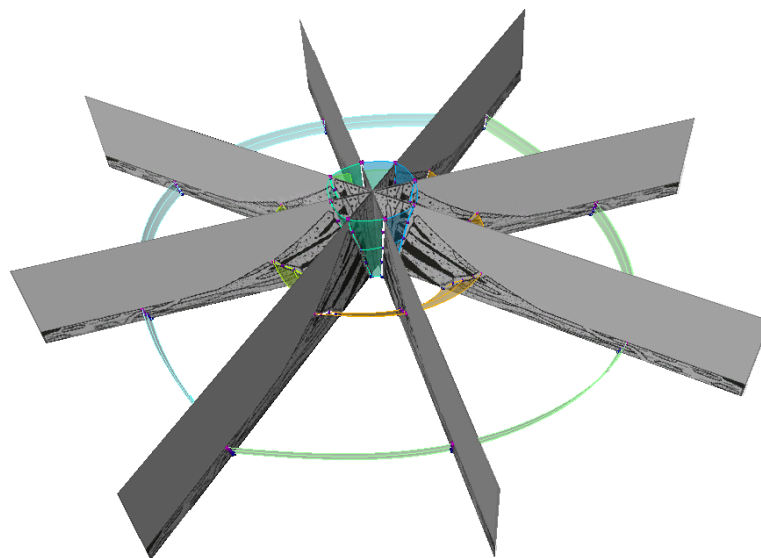
Figure 45: Final Fault Model of the volcano.

For interpreting the vertical boundaries of a reef the same principles were applied as for the volcano and a Fault Model was created. Because of the simplicity of the karst body no Fault Model was required.

In case of the salt dome faults were interpreted around the geological boundaries of the salt dome and converted to curved pillars (Figure 46).
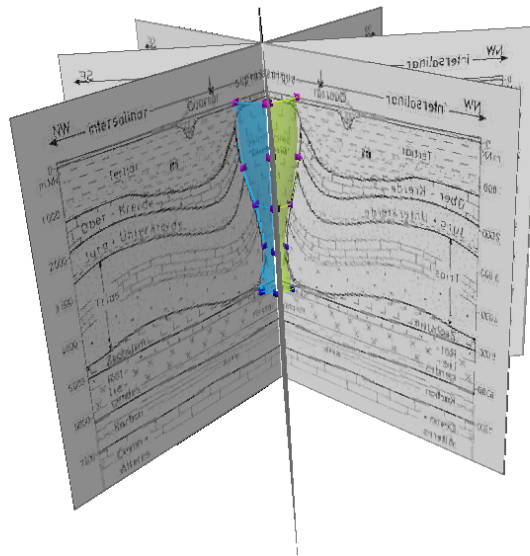
Figure 46: Final Fault Model of the salt dome.

Modeling horizontal boundaries:

Top and base of the volcano represent horizontal boundaries. The proximal zone of the volcano shows different layers of predominantly two different alternating facies types, which reflect additional horizontal facies boundaries (Figure 41). The horizontal boundaries were picked by fault interpretation as a first step (Figure 47) and then transformed into points by applying the process "Convert to points" (Figure 48). These points were then converted to surfaces. To make such a surface all relevant points from former interpretations, that should be included in the surface, were linked to one interpretation. This was done by appending points (Figure 49). By applying the "Make/Edit Surface" process points were transformed to a surface (Figure 50). Figure 51 shows the created surfaces of the volcano.
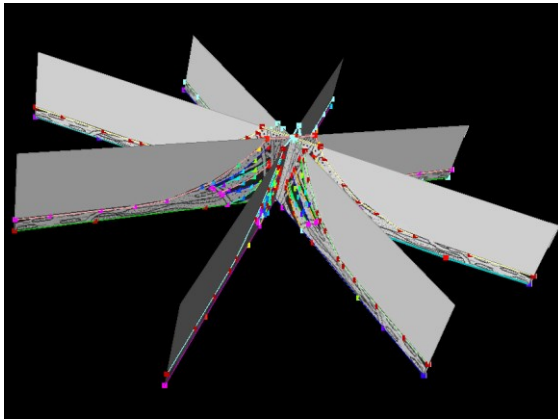
Figure 47: Interpreted horizontal boundaries of the volcano by fault interpretation.
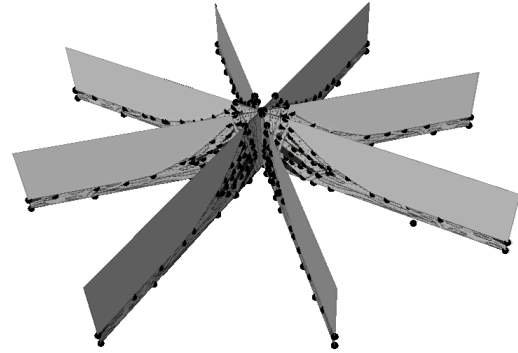
Figure 48: Interpreted horizontal boundaries of the volcano converted to points.
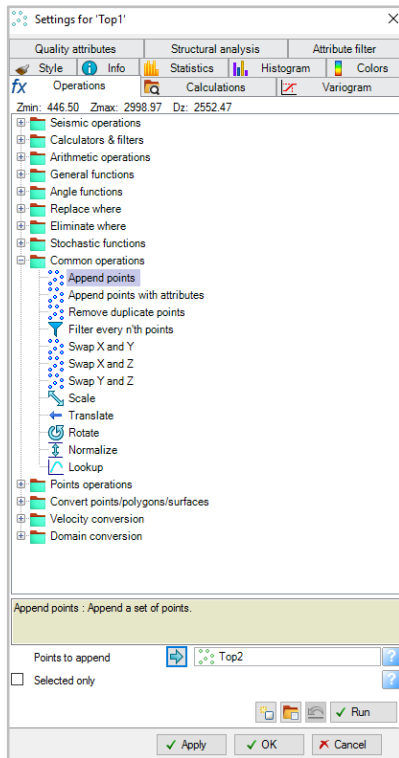
Figure 49: Appending points of Top 2 to Top 1. After running this process Top 1 included all points of Top 2 (Top 1 and Top 2 are names for the horizontal interpretations of the top of the volcano).
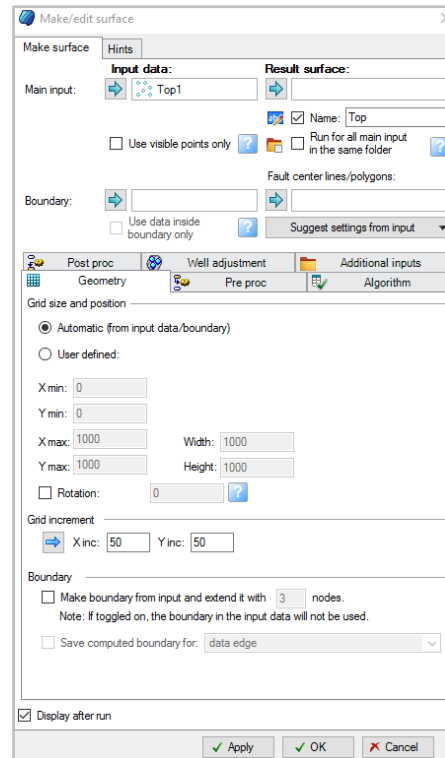
Figure 50: "Make/edit Surface" process converts points (Top 1) to a surface (Top) by using an automatic grid size.
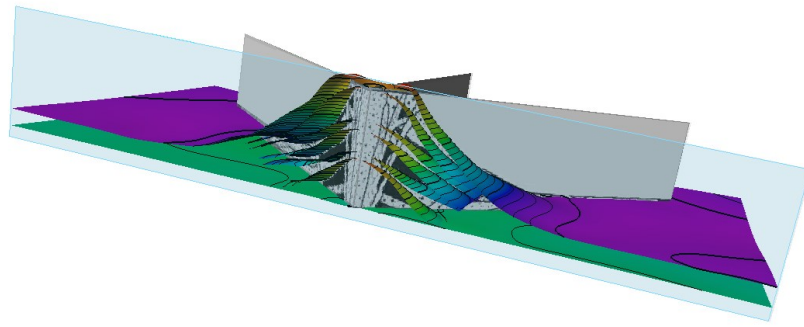
Figure 51: Intersection through the volcano with displayed surfaces.

2.4.3   **3D Grid**

After defining the vertical boundaries a 3D grid was created. It represents the framework of the model and is build up by cells. Petrel Software uses the Pillar Grid, which sets up the grid along the key pillars.

For Pillar Gridding the active Fault Model was displayed in a 2D window. First an external grid boundary was manually defined around the volcano and will later represent the outer boundary of the final facies model. Next each fault (vertical boundary) was defined with an I- or J-direction. I-directions are defined as green lines and J-directions as red lines (Figure 52). By applying the "Pillar Gridding" process a new 3D grid was generated with top-, mid- and base skeleton (Figure 53). The skeleton represents a series of pillars and each pillar is a corner of a grid cell (Schlumberger, 2015). Grid cells are aligned along the two previously defined directions. The generated 3D grid consists of four segments and each segment represents one of the four volcanic zones. After Pillar Gridding a quality check of the skeleton was performed in order to detect irregularities, which can occur due problems in the Fault Model. Therefore, the Fault Model was edited by adjusting the key pillars and the "Pillar Gridding" process was run again. Because problems of the fault model can often not be detected until Pillar Gridding, it is normally an iterative process until the skeleton is acceptable. To simplify Pillar Gridding and minimize irregularities only vertical, linear and listric pillars can be used to create the 3D grid. This can be defined during the Pillar Gridding process under Geometry by excluding Curved Pillars.

For the upcoming vertical layering of the volcano it was necessary to create four identical 3D grids. Because each grid is represented by four segments, only one segment per 3D grid was used for vertical layering. This means for the central 3D grid the central segment, for the proximal 3D grid the proximal segment (Figure 54, Figure 55) and so on. At the end all four 3D grids with their specific segments were displayed in a 3D window to show the final facies model.
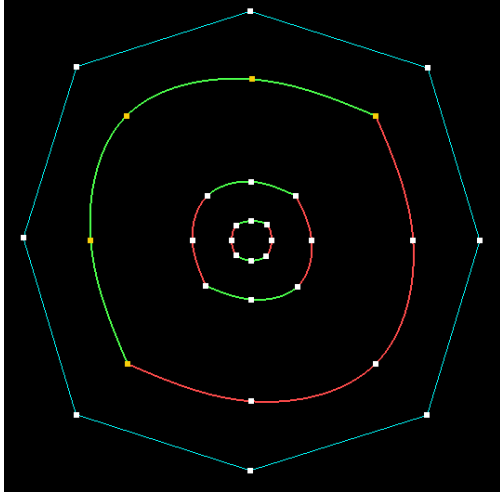
Figure 52: External grid boundary (blue line) and faults of the volcano represented by I- (green lines) or J-direction (red lines)
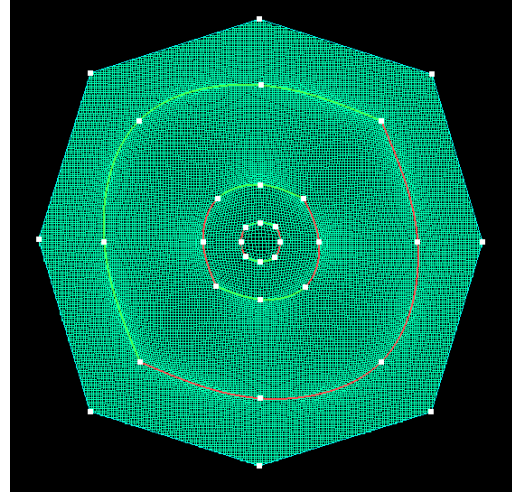
Figure 53: Green mid skeletons of the four segments after Pillar Gridding.
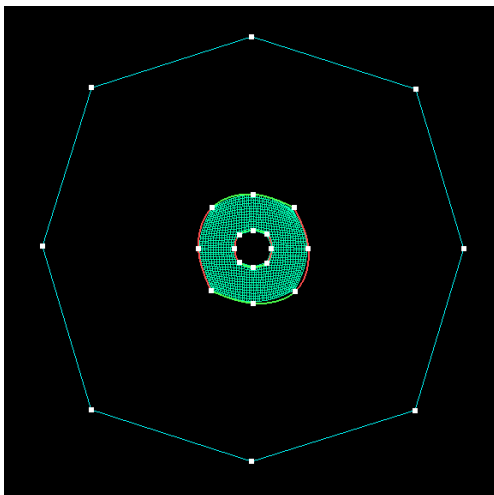
Figure 54: Green mid skeleton of the proximal zone of the volcano with surrounding faults.
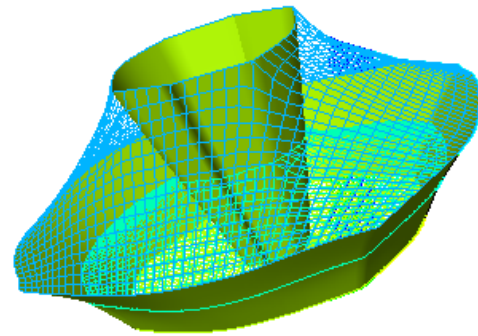
Figure 55: Proximal 3D grid of the volcano with edges (green) and top- (blue), mid- (green) and base skeleton (yellow).
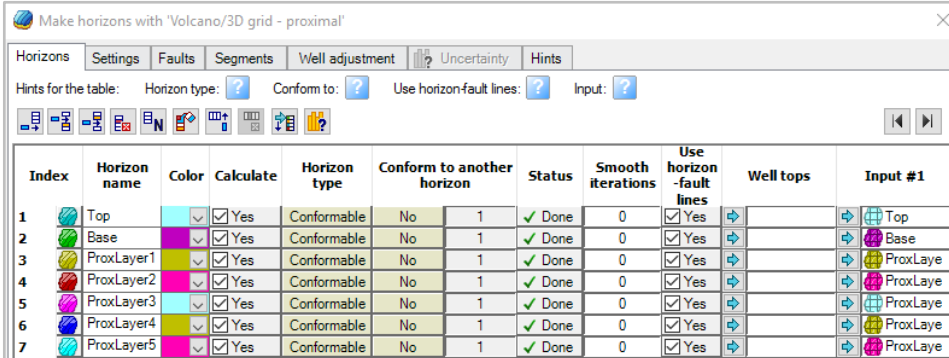
For complex geological bodies like the reef the grid building process becomes more elaborate. In general it was the same procedure like for the volcano (one 3D grid per facies), but due to stacked facies it was often necessary to create two grids per facies. For the reef the step by step process of building a 3D grid and vertical layering is demonstrated in Appendix A.

In case of the karst bodies only an external boundary (no Fault Model available) for Pillar Gridding was defined and therefore only one 3D grid was created.

2.4.4 Vertical Layering

To create the vertical layering of the 3D grid the previously created surfaces (horizontal boundaries) were transformed into horizons with the "Make Horizons" process. This was done for each zone and therefore each 3D grid separately.

For the central, medial and distal 3D grids of the volcano only horizontal boundaries of top and base were transformed into horizons. For the proximal zone of the volcano the internal horizontal facies boundaries were converted to horizons additionally to top and base. The process of "Make Horizons" is explained based on the proximal zone. To create horizons only for the proximal zone two steps were performed. First in the "Make Horizons" process under the Settings Tab „Force Horizons to be calculated for all segments" was deactivated and then under the Segments Tab only the proximal segment was activated. Under Input in the Horizons Tab all relevant surfaces for the proximal zone were included (Figure 56). Zones between the horizons were automatically created after applying the "Make Horizons" Process (Figure 57).

Figure 56: "Make Horizon" process for the proximal zone of the volcano. Under Input all relevant surfaces are included.
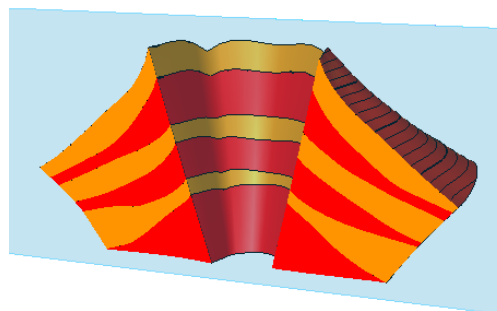
Figure 57: Intersection threw the proximal zone of the volcano with horizons (horizontal boundaries in red) and zonations (area between the horizons colored in orange and red).

2.4.5 **Object Modeling**

Facies modeling with Method II has its limitations. Especially when it comes to facies which is randomly distributed, not present in every direction and normally placed within a main facies. To overcome this issue Object Modeling from Method I was used.

In case of the volcano the distal zone consists of two facies types. The main facies already modeled by Method II and a second minor facies represented by clasts and randomly distributed within the main facies. To apply Method I it is necessary to layer the zone in which the facies should be distributed, which is done by the "Layering" process. The more layers are defined the better the resolution of the facies will be. To place the minor facies within the main, Object Modeling was used. Therefore, the minor facies was displayed as ellipsoids and the main facies, which is defined as zone "Top-Base" was set as the background (Figure 58). The final facies model is shown in Figure 59.
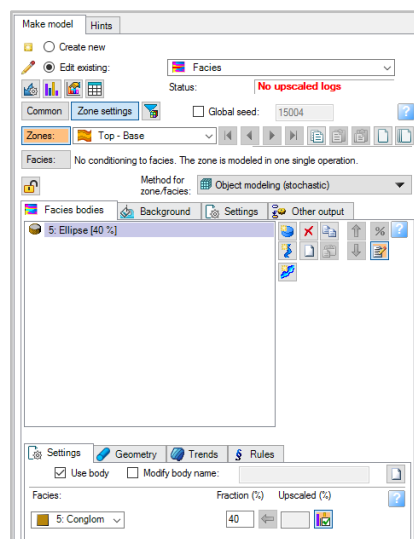
Figure 58: "Facies Modeling" process placing ellipsoids as minor facies with a fraction of 40% within zone "Top-Base" defined as major facies.
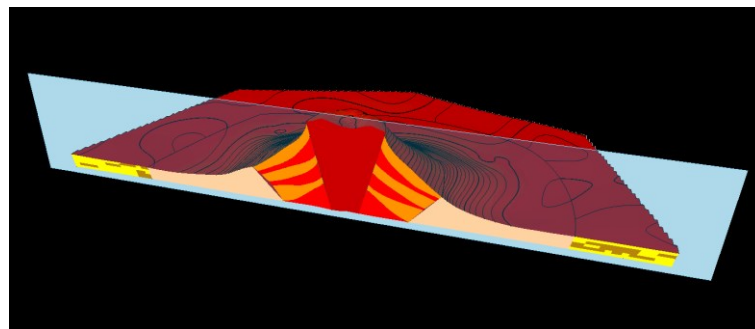
Figure 59: Final facies model of the volcano. Distal zone represented by the main facies in yellow and the minor facies in brown as ellipsoids.

For the karst body, caves were inserted to several distinct zones by Object Modeling. In case of the "main dolomite"/"dachstein limestone" an additional trend was included, which decreases linearly from top of the zone to the base. Inserting trends was already discussed under Method I. The karstified limestone zone contains even two cave types and therefore two additional facies to the main facies. Measurements and fractions of the caves applied to the zones can be found in the fact sheets for karst bodies (Figure 99, Figure 100).

2.4.1 Facies Trends

To influence the distribution of the facies bodies either in vertical or horizontal direction, trend maps can be inserted. In case of the channel no additional trend was included. Therefore, the application of a trend map is shown by the lobes of a submarine fan. In this case a linear trend was inserted to model the increase of lobes with increasing depth (Figure 59). This trend should reflect the coarsening up succession of sandy turbidites. The trend was inserted under the vertical trend of the trend tab in the "Facies Modeling" process.
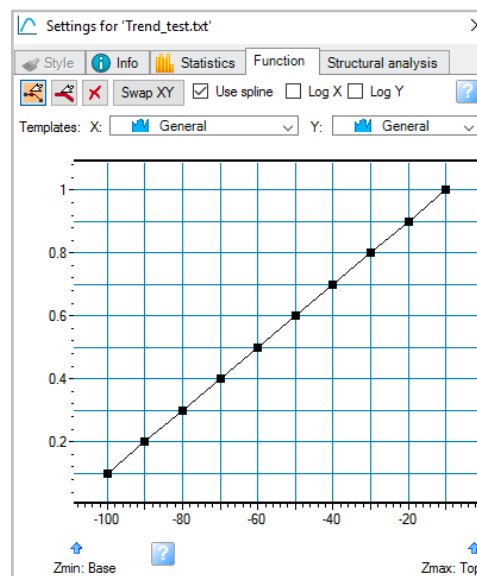
Figure 60: Increasing vertical trend from bottom of the 3D grid at a depth of -100m to top of the 3D grid at a depth of 0m.

3 Petrophysical parameters

3.1 Experimental results and empirical relationships

3.1.1 General characteristics

Density, compressional- and shear wave velocity change between different rock types and are strongly influenced by several factors. Table 1 gives an overview of the most common influencing factors (porosity, shale content, fluid fill and depth) beside the mineral composition on density and velocity for different rock types. In general there are more factors influencing density and velocity, but for the purpose of this study only the most common are discussed. Depth dependence due increasing effective stress from overburden has a direct influence on porosity. Changes of porosity, mineral composition and fluid fill finally affect density and velocity (compressional wave velocity is much stronger influenced by fluid properties than shear wave velocity). In general this is the case for clastic rocks and some limestones. Clay content in sandstones and carbonates has a direct influence on the depth dependence and therefore porosity (Schön, 1989). Dolomite is more rigid than limestone and in return less influenced by depth. Monomineralic rocks without porosity like salt and anhydrite are not influenced by any of the factors. Porosity of basalts and rhyolites influences density and velocity and may lead to depth dependence due to closure of pores and fractures under compaction (Schön, 2015).

Table 1: Density, compressional and shear wave velocity for different rock types influenced by porosity φ, shale content Vsh, fluids (water, gas, oil) and depth z.

Lithology	Influencing factors	Lithology	Influencing factors
Sandstone	Φ, Vsh, fluids, z	**Salt**	-
Shale	Φ, z	**Anhydrite**	-
Limestone	Φ, Vsh, fluids, (z)	**Basalt**	Φ, (z)
Dolomite	Φ, Vsh, fluids	**Rhyolite**	Φ, (z)

Elasticity of an isotropic material can be described by only two constants, which are mainly bulk modulus (k) and shear modulus (μ) (Gebrande et al., 1982). In literature different pairs of constants are used. Compressional- and shear wave velocity as well as density depend on them:

$$V_p = \sqrt{\frac{k+(4/3)\cdot\mu}{\rho}} \qquad (1)$$

$$V_s = \sqrt{\frac{\mu}{\rho}} \qquad (2)$$

Where ρ is the bulk density (kg/m³). Bulk density is the mean density of the rock volume, including the pore volume and is defined as the quotient of the mass m and the volume V:

$$\rho = \frac{m}{V} \qquad (3)$$

Stress and strain for an anisotropic, linear elastic material are related by the general Hooke's law (Equ. 4) (Landau and Lifshitz, 1965). A linear relation between stress and strain is in general not given for rocks, but can be assumed for sufficiently small changes (Schön, 2015).

$$\sigma_{ik} = C_{iklm}\varepsilon_{lm} \qquad (4)$$

Where:

σ_{ik} is the stress tensor

ε_{ik} is the strain tensor

C_{iklm} is the elastic modulus (or stiffness) tensor

The indices m and n are transformed from ij and kl. Stresses and strains are written as column matrices and straines as six times six matrix (21 independent constants). Symmetry results in a reduction of constants (Gebrande et al., 1982).

	ij(kl)	11	22	33	23, 32	13, 31	12, 21
	m(n)	1	2	3	4	5	6

3.1.2 Mineral composition, porosity and pore fluid

3.1.2.1 Influence on density

The density of porous rocks depends on the mineral composition (matrix density), the porosity (pores, fractures) and the density of the pore fluid (Schön, 2015). The pore fluid can be either gas, water, oil or a combination. For this study only a single pore fluid case was taken in account. Table 2 shows mean densities for pore fluids defined by Schlumberger (2000).

Table 2: Mean densities for fresh water, salt water and oil (after Schlumberger, 2000).

Fluid	Mean densities [kg/m^{-3}]
Fresh water	$1{,}000*10^3$
Salt Water (200.000ppm)	$1{,}146*10^3$
Oil	$0{,}85*10^3$

Equ. 6 explains a density decrease with increasing porosity and a change of pore fluid (salt water -> fresh water -> oil -> gas).

$$\rho = (1 - \emptyset) \cdot \rho_{ma} + \emptyset \cdot \rho_{fl} \qquad (6)$$

The influence of porosity on bulk density for dry (gas) and water saturated sedimentary rocks is illustrated by Figure 61 (Schön, 2011). In case of pore free rocks like salt, anhydrite and dense carbonates, the density is only determined by the mineral composition.
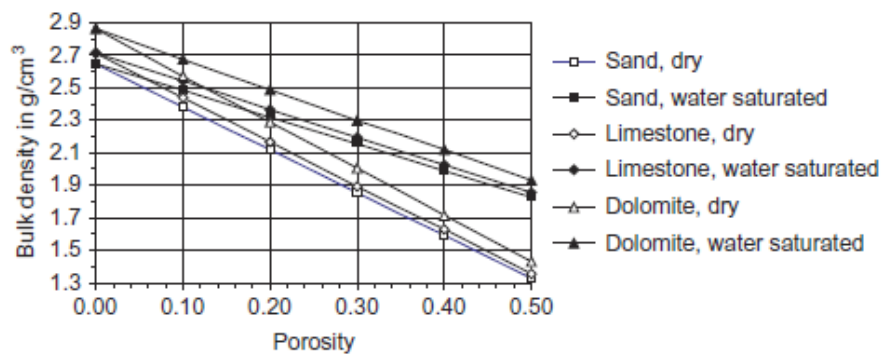
Figure 61: Relationship between bulk density and porosity for dry (ρfl = 0,00 g/cm³) and water saturated (ρfl = 1,00 g/cm³) sandstone (ρma = 2,65 g/cm³), limestone (ρma = 2,71 g/cm³) and dolomite (ρma = 2,86 g/cm³) (Schön, 2011).

3.1.2.2 Influence on compressional- and shear wave velocity

The velocity of pore free rocks is only controlled by the mineral composition, whereas the velocity of porous rocks is additionally influenced by porosity, pore type, grain-grain contact, cementation and pore fluid. In general velocity is decreasing with increasing porosity. A simplified porosity-velocity relationship is described by the time-average equation or so called Wyllie equation (Wyllie et al., 1956):

$$\frac{1}{Vp} = \frac{1-\Phi}{Vp} + \frac{\Phi}{Vfl} \qquad (7)$$

V_p compressional wave velocity of the porous rock

$V_{p,ma}$ compressional wave velocity of the matrix composition

V_{fl} compressional wave velocity of the pore fluid

The equation can also be written in terms of slowness:

$$\Delta t_p = (1 - \Phi) * \Delta t_{p,ma} + \Phi * \Delta t_{fl} \qquad (8)$$

The equation works best for isotropic, well compacted (30MPa) and water saturated porous rocks (Wyllie et al., 1956). The presence of gas may distort the results and poorly compacted porous rocks result in overestimated slowness values. If Δt_{shale} > 100µs ft^{-1}, a compaction correction on the porosity can be applied (Asquith and Krygowski, 2004):

$$\phi_{corrected} = \phi_{Wyllie} \cdot \frac{1}{C_p} = \frac{\Delta t - \Delta t_{ma}}{\Delta t_{fl} - \Delta t_{ma}} \cdot \frac{100}{\Delta t_{shale}} \qquad (9)$$

In case of carbonate rocks the Wyllie equation works best for intergranular porosity without vuggy porosity. Moldic or intrafossil porosities lead to an underestimation of slowness (Jennings and Lucia, 2001).

Raymer et al. (1980) suggests the Raymer-Hunt-Gardner equation as an improvement of the Wyllie Equation.

For porosity below 37%:

$$V_p = (1 - \phi)^2 \cdot V_{p,ma} + \phi \cdot V_{fl} \qquad (10)$$

For porosity above 47%:

$$\frac{1}{\rho V^2} = \frac{\phi}{\rho_{fl} V_{fl}^2} + \frac{1-\phi}{\rho_0 V_0^2}, \quad \phi > 47\% \qquad (11)$$

Figure 62 shows the comparison of the Wyllie et al. (1956) and Raymer et al. (1980) velocity porosity models for water saturated clay free sandstones. Consolidated and cemented sandstones fit the equations quite well, but unconsolidated and uncemented sandstones are not fitting any of the equations and should therefore not be used for velocity porosity models (Mavko et al. (1989).
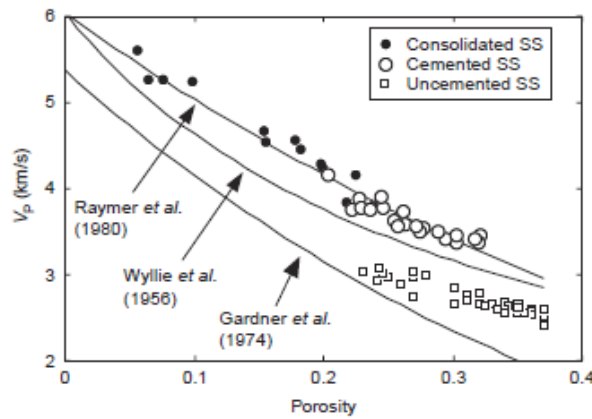
Figure 62: Comparison of the Wyllie et al. (1956), Raymer et al. (1980) and Gardner at al. (1974) velocity porosity models for consolidated, cemented and uncemented water saturated clay and free sandstones (Mavko et al. (1989).

Beside porosity, clay content plays a major role for compressional- and shear wave velocities. The influence is demonstrated on a sandstone example (Table 3). This example shows four cases using two different porosities Φ (10% and 25%) and two different shale volumes Vsh (0% and 30%) for compressional- and shear wave velocity estimation. The regressions (Equ. 12, 13) used for this example were investigated by Kirchberger (2001) for water saturated shaly sand formations from the Vienna Basin. The example shows that the highest porosities and shale content lead to the lowest velocities and vice versa.

$$V_P = 5.358 - 5.408 \cdot \phi - 2.926 \cdot V_{shale} = 5.358 \cdot (1 - 1.008 \cdot \phi - 0.546 \cdot V_{shale}) \qquad (12)$$

$$V_S = 2.802 - 3.935 \cdot \phi - 1.750 \cdot V_{shale} = 2.802 \cdot (1 - 1.404 \cdot \phi - 0.625 \cdot V_{shale}) \qquad (13)$$

where Vp and Vp is in km/s.

Table 3: Sandstone example to demonstrate the impact of porosity and shale content on compressional- and shear wave velocities.

Φ	Vsh	Vp [km/s]	Vs [km/s]
0,1	0	4,818	2,409
0,1	0,3	3,940	1,884
0,3	0	3,737	1,622
0,3	0,3	2,860	1,097

This velocity decrease with increasing porosity and shale volume (Figure 63) was already shown by Han et al. (1986) for water saturated shaly sandstones. Linear regressions for velocity (km/s) and slowness (s/km = 10^3μs/m) correlate very well:

$$V_p = 5.59 - 6.93 \cdot \phi - 2.18 \cdot C \qquad R = 0.985 \qquad (14)$$

$$V_s = 3.52 - 4.91 \cdot \phi - 1.89 \cdot C \qquad R = 0.959 \qquad (15)$$

$$\Delta t_p = 0.163 + 0.399 \cdot \phi + 0.119 \cdot C \qquad R = 0.972 \qquad (16)$$

$$\Delta t_s = 0.242 + 0.812 \cdot \phi + 0.307 \cdot C \qquad R = 0.945 \qquad (17)$$
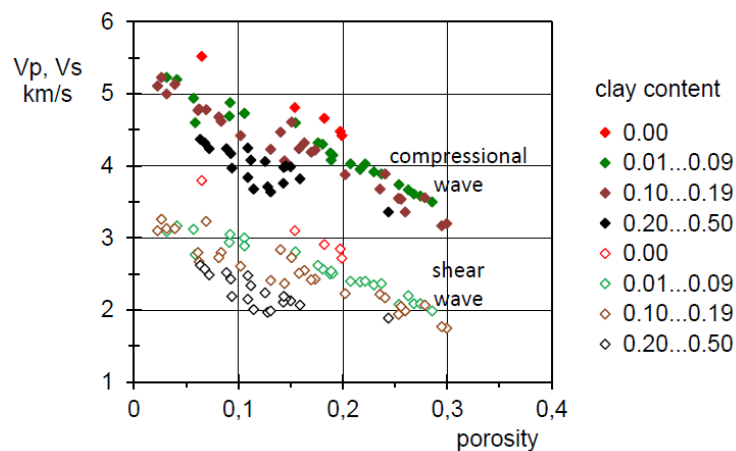
Figure 63: Influence of clay content on compressional- and shear wave velocities (km/s) versus porosity for water saturated shaly sandstones at 40MPa (Schön, 2015 after Han et al, 1986).

Similar equations were achieved by Castagna et al. (1985) for water saturated shaly sands of the Frio Formation:

$$V_p = 5.81 - 9.42 \cdot \phi - 2.21 \cdot C \qquad (18)$$

$$V_s = 3.89 - 7.07 \cdot \phi - 2.04 \cdot C \qquad (19)$$

where Vp is in km/s.

Equations for gas and brine saturated shaly sands from the North Sea (35MPa reservoir pressure) were investigated by Marion and Jizba (1992). The regressions show that shear wave velocity is relative insensitive to a change of pore fluid, that porosity has a similar effect on both velocities and that the effect of clay is more important to the shear wave velocity.

Gas:

$$V_p = 4.82 - 5.02 \cdot \phi - 0.597 \cdot C \qquad (20)$$

$$V_s = 3.26 - 3.03 \cdot \phi - 0.892 \cdot C \qquad (21)$$

Brine:

$$V_p = 5.46 - 6.29 \cdot \phi - 1.10 \cdot C \qquad (22)$$

$$V_p = 3.32 - 3.62 \cdot \phi - 0.952 \cdot C \qquad (23)$$

where Vp and Vs is in km/s.

For carbonate rocks the velocity porosity relationship depends on the pore type (Figure 64). Microporosity and interparticle crystalline porosity show a good correlation, whereas moldic porosity shows a broader scatter and densely cemented low porosity show high porosities (Eberli et al. (2003).
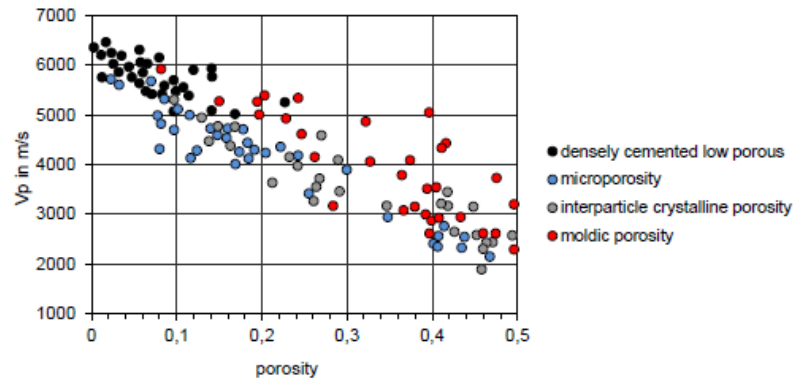
Figure 64: Velocity (m/s) versus porosity for different pore types of water saturated carbonate (Eberli et al. (2003).

Lebdev et al. (1974) and Schön (2015) show that the velocity of granites depends on porosity as well as grain size.
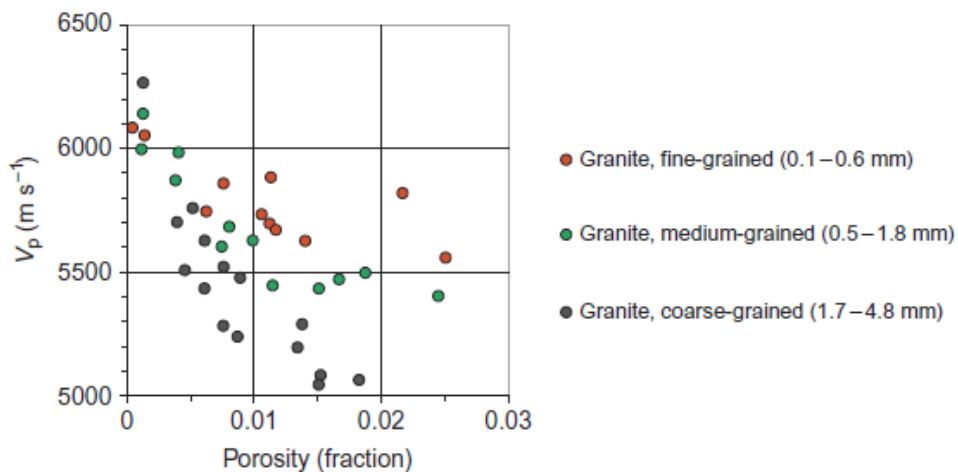
Figure 65: Compressional wave velocity (m/s) versus porosity influenced by the crack porosity (volume fraction) and the grain size of the granites (0,1MPa); (Schön, 2015 modified after Lebedev et al. (1974).

For sandstones Figure 66 shows the different effect of pore fluids on compressional- and shear wave velocities. Velocity change is the combined effect of elastic moduli and density variation. Compressional wave velocity increases from dry (gas) to kerosene and is highest for water. The opposite happens for shear wave velocity, because fluids have no shear resistance (King 1966). Therefore, the shear modulus of the sediment is not influenced by fluids and only the density effect originates velocity change. In general oil has a higher viscosity than water, but for heavy oils with high viscosities shear resistance is present (Wang and Nur, 1988).
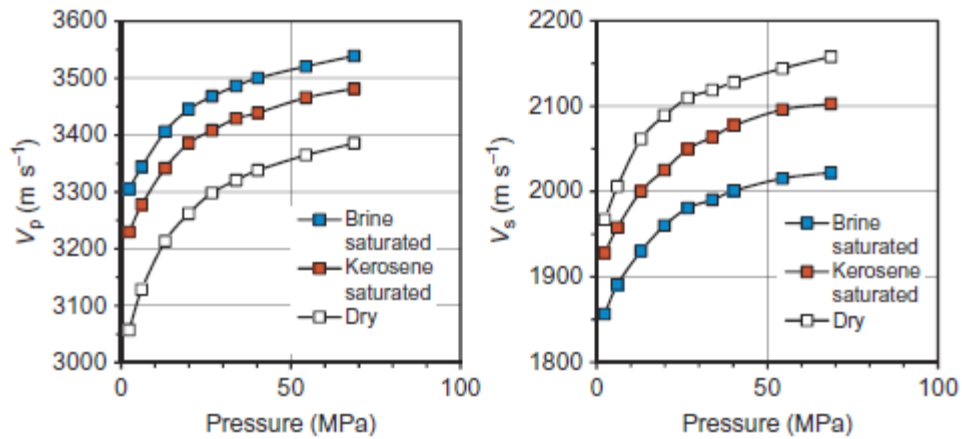
Figure 66: Compressional- and shear wave velocities (m/s) of Boise sandstone influenced by different pore fluids (Schön, 2015 modified after King, 1966).

The pore fluid has a comparable effect on carbonate rocks as on sandstones (Figure 67a). The saturated compressional wave velocity is higher than the dry one and vice versa for shear wave velocities (Rogen et al., 2005).
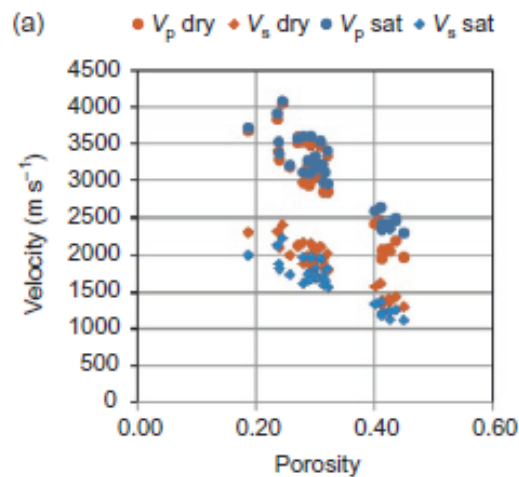
Figure 67: Compressional- and shear wave velocities (m/s) versus porosity for dry and saturated carbonate rocks (Rogen et al., 2005).

For fluid replacement the static Gassman model can be used. It predicts velocities for a saturated rock with one fluid, for instance water, from the velocities of a saturated rock with another fluid, for instance gas (Gassman, 1951). The Gassman Model assumes an isotropic rock with interconnected pores that are filled with a non-viscous fluid, but without fluid flow. Further the rock-fluid system is closed and the pore fluid does not change the rock skeleton (Dewa and Pickford, 2001). Figure 68 shows a rock under compression for two cases of fluid fill. For the left rock the

pores are gas filled and therefore the pore fluid has zero bulk and shear moduli. The deformation behavior is only characterized by the effective bulk and shear modulus of the dry rock (k_{dry}, μ_{dry}). In case of the water saturated rock, the fluid contributes now to the effective bulk modulus of the saturated rock (k_{sat}). The effective shear modulus for the saturated rock (μ_{sat}) is the same as for the dry rock, because pore fluid does not contribute to the shear modulus.
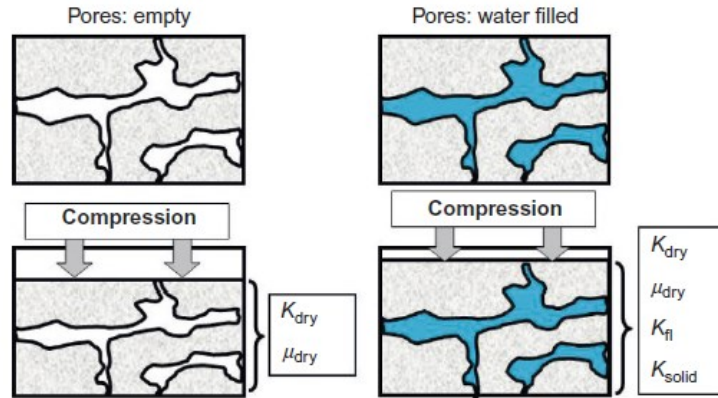
Figure 68: Graphical explanation of the Gassman Model showing two cases of fluid fill and the elastic moduli.

$$\frac{k_{sat}}{k_s - k_{sat}} = \frac{k_{dry}}{k_s - k_{dry}} + \frac{k_{fl}}{\phi \cdot (k_s - k_{fl})} \qquad (24)$$

$$k_{sat} = k_{dry} + \frac{\left(1 - \frac{k_{dry}}{k_s}\right)^2}{\frac{\phi}{k_{fl}} + \frac{1-\phi}{k_s} - \frac{k_{dry}}{k_s^2}} \qquad (25)$$

k_{sat} is the effitive bulk modulus of the rock with pore fluid

k_{dry} is the effective bulk modulus of the drained or dry rock ("framework")

k_s is the bulk modulus of the solid rock component

k_{fl} is the bulk modulus of the pore fluid

ϕ is the porosity

The two moduli and the density give the velocities:

$$V_p = \sqrt{\frac{k + \frac{4}{3}\mu}{\rho}} = \sqrt{\frac{k_{dry} + \frac{\left(1 - \frac{k_{dry}}{k_s}\right)^2}{\frac{\phi}{k_{fl}} + \frac{1-\phi}{k_s} - \frac{k_{dry}}{k_s^2}} + \frac{4}{3}\mu_{dry}}{(1-\phi) \cdot \rho_s + \phi \cdot \rho_{fl}}} \qquad (26)$$

$$V_s = \sqrt{\frac{\mu}{\rho}} = \sqrt{\frac{\mu_{dry}}{(1-\phi) \cdot \rho_s + \phi \cdot \rho_{fl}}} \qquad (27)$$

Table 4: Ranges of compressional bulk modulus k_{fluid} and density ρ_{fluid} (Schön, 2015).

Fluid	k_{fluid} (GPa)	ρ_{fluid} $(kg\ m^{-3})$
Gas	$0.01 - 0.4$	$0.1 - 0.5 * 10^3$
Oil	$0.4 - 3.0$	$0.7 - 1.1 * 10^3$
Water	$2.0 - 4.0$	$0.9 - 1,2 * 10^3$

3.1.3   **Depth**

3.1.3.1   **Influence on porosity**

Klopf (1977) distinguishes non porous rocks with nearly no depth dependence from depth dependent porous rocks. Figure 69 shows the tendency of porosity reduction for different rock types.
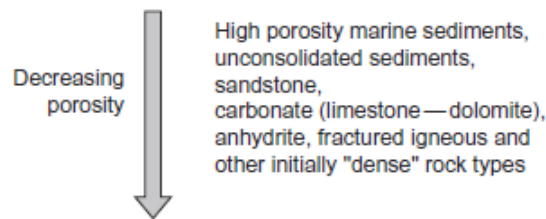
Figure 69: Tendency of porosity decrease for several rock types (Schön, 2015).

Athy (1930) was one of the first who described the nonlinear porosity decrease with depth for sedimentary environments:

$$\phi(z) = \phi_0 \cdot \exp(-b \cdot z)$$

(28)

ϕ_0 porosity at initial depth (z = 0m)

z actual depth

b parameter characterizing the compressibility of the sediment

Table 5: Initial porosity and exponent b for sandstone, shale and carbonate (Athy, 1930).

Rock	Initial Porosity ϕ_0	Remarks	Exponent b	Remarks
Sandstone	0.4 … 0.5	depends on sorting	$2 …4 * 10^{-4}$	
Shale	0.7 … 0.9	depends on clay mineralogy	$4 …6 * 10^{-4}$	depends on clay-silt-sand content
Carbonate	0.05 … 0.3	depends on carbonate type	$10^{-4} … 10^{-3}$	depends on type and mineral composition (shale)

Table 5 can be used as a first approximation. As a rule for clastic rocks the initial porosity is increasing and the exponent b is decreasing from sand to shale/clay. For carbonates the initial porosity is in general higher for dolomite than for limestone. The exponent b decreases with "hardness" and is therefore higher for rigid dolomite than for limestone.

In a log versus depth crossplot Athys correlation is shown by a straight line where the depth z is in meters and the porosity φ is a fraction (Figure 70).
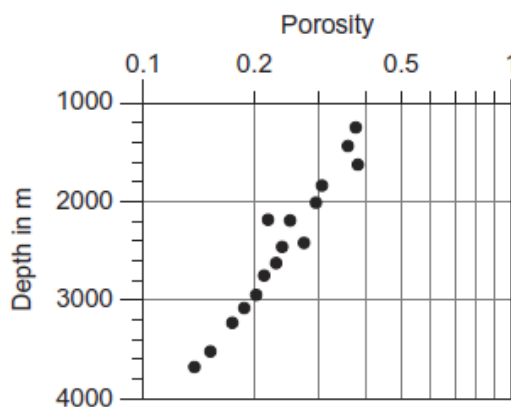
Figure 70: Logarithmic porosity versus depth crossplot for sandstone (Nagumo, 1965)

Porosity versus depth relationships were analyzed for sandstone and shale from the Northern North Sea by Liu and Roaldset (1994) and Sclater and Christie (1980). The exponential equations of Figure 71 show the higher initial porosity of shale compared to the loosely packed sand grains. Further the softer rock skeleton of shale has a lower compressibility than the sand rock skeleton.

Sandstone $\quad \phi = 0.490 \cdot \exp(-2.7 \times 10^{-4} \cdot z)$

Shale $\quad \phi = 0.803 \cdot \exp(-5.1 \times 10^{-4} \cdot z)$

Initial porosity

Rock skeleton compressibility
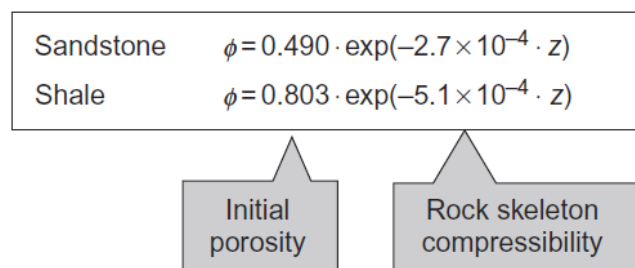
Figure 71: Exponential Equations for sandstone and shale indicating initial porosity and rock skeleton compressibility (Schön, 2015 after Liu and Roaldset, 1994 and Sclater and Christie, 1980)

In clastic rocks the porosity decreases nonlinear due to compaction. Thereby, the initial porosity depends on the grain size distribution and the depositional conditions during deposition (Schön,

1989). Compaction is an irreversible process caused by effective pressure due to overburden sediments, the drainage of pore fluids and the packing of grains (Schön, 2015). Figure 72 shows that the initial porosity is higher for shale compared to sand. The process of compaction can be either mechanically at more shallow depths or chemically at greater burial depths of 2000-3000m when quartz cementation of sand occurs. Mechanical compaction leads to a steeper porosity gradient for shale than for sand, but during chemical compaction the porosity gradient will be steeper for sand (Avseth et al., 2005).
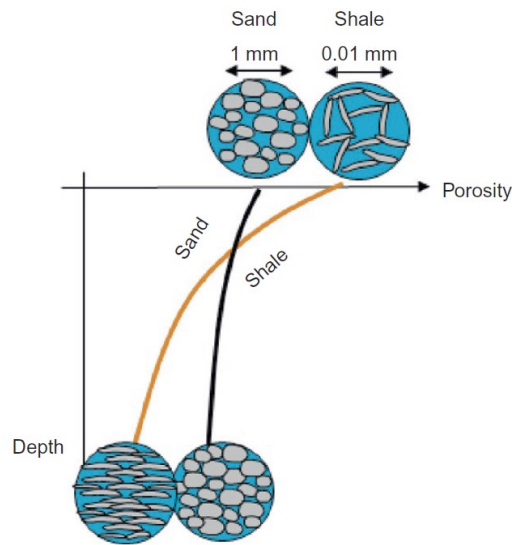
Figure 72: Compaction process for sand and shale (Schön, 2015).

Initial porosity ranges (Table 6) from porosity versus depth curves were summarized by Poelchau et al. (1997).

Table 6: Ranges of initial porosity from porosity versus depth curves (after Poelchau et al., 1997).

Lithology	Initial Porosity
Sandstone	0,25-0,55
Shale	0,50-0,90
Limestone	0,40-0,95
Grainstone/Packstone	0,44-0,55
Deep sea calcareous ooze	0,70-0,95

Rowen et al. (2003) derived exponential equations for sand, silt and shale from porosity versus depth curves from 19 offshore wells. The sediment groups were classified by using the shale content Vsh from a gamma log as a parameter:

$$for\ sand\ (V_{sh} < 0.01): \quad \phi = 0.50^{-0.29 \cdot z} \tag{29}$$

$$for\ silt\ (0.495 < V_{sh} < 0.505): \quad \phi = 0.44^{-0.38 \cdot z} \tag{30}$$

$$for\ shale\ (V_{sh} < 0.9): \quad \phi = 0.40^{-0.42 \cdot z} \tag{31}$$

Brown (1997) analyzed different carbonate rocks to show their porosity decrease with increasing depth (Figure 73). Depending on the mineralogical composition and clay content, carbonate rocks show different porosity depth curves. Argillaceous limestone has low porosities compared to the other carbonates. Clay content in limestone leads to a pronounced porosity decrease with depth. Dolomite is more porous than limestone, but because of its higher rigidity the porosity decrease of dolomite is less pronounced (Schön, 2015).
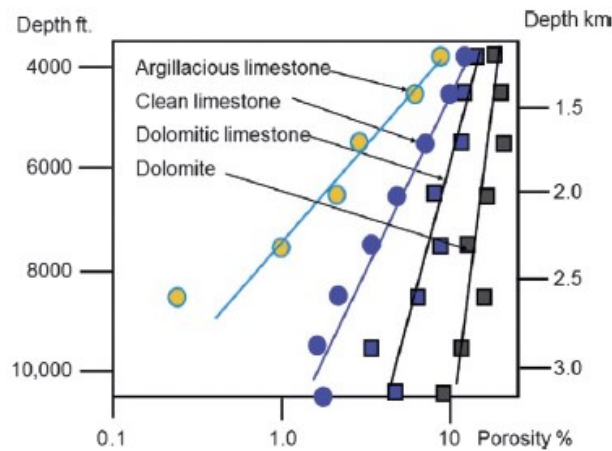
Figure 73: Porosity versus depth curves for argillaceous limestone, clean limestone, dolomitic limestone and dolomite of the Mississippian Madison Group in the Williston Basin (Brown, 1997).

3.1.3.2 Influence on density

Equ. (29) is the combination of the Equ. (6) for the density (kg/m³) of porous rocks with Athy's equation Equ. (28) for a nonlinear porosity decrease with depth (Athy, 1930). The equation can be used as a first approximation to determine the density at a specific depth under the influence of porosity or pore fluid:

$$\rho(z) = \rho(ma) - \left(\Phi(o) * e^{-bz}\right) * (\rho(ma) - \rho(fl)) \qquad (32)$$

Kopf (1977) investigated on the depth dependence of clastica. He concluded that the mechanical compaction of clay and silt leads to nearly pore free shale. If clay or silt is present in sandstones they show a similar density depth relationship like shale (Schön, 1983). Figure 74 shows an example of a density versus depth investigation for dry siltstones of the Norddeutsch-Polnische Senke (Kopf, 1970).
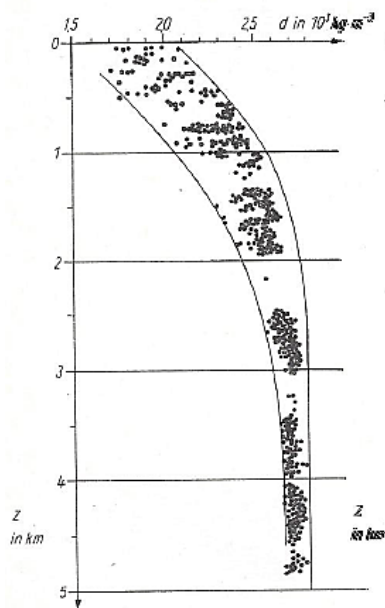
Figure 74: Nonlinear increase of density with depth for dry siltstones of the Norddeutsch-Polnische Senke (Kopf, 1970).
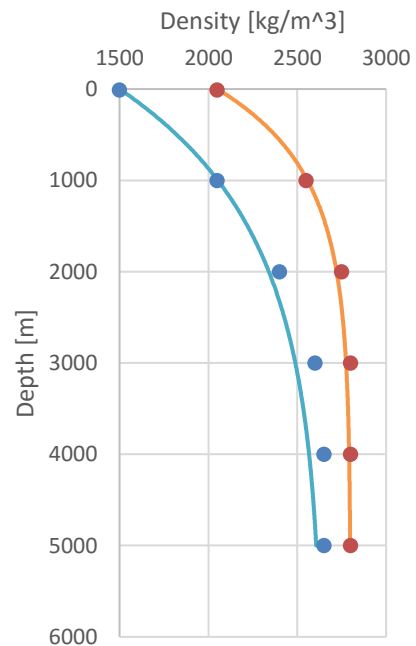
Figure 75: Exponential functions of the density depth relationship from Kopf (1970), recreated by using the exponential function of Stegena (1964). The blue line represents the minimum curve and the orange line the maximum curve.

To receive the nonlinear density depth relationship for dry siltstones of the Norddeutsch-Polnische Senke, the exponential function (Equ. 30) provided by Stegena (1964) was used for recreation (Figure 75):

$$\rho(z) = \rho(zo) + \big(\rho(zo) - \rho(zm)\big) * (1 - e^{-A*z}) \tag{33}$$

ρ(z)   density (kg/m³) at the actual depth z

ρ(zo)   density (kg/m³) at the initial depth

ρ(zm)   density (kg/m³) at maximum depth of subsidence; below zm no density increase occurs

A   empirical factor

Table 7: Density at initial depth ρ(zo), the density at maximum depth of subsidence ρ(zm) and the empirical factor (A) for minimum (blue) and maximum (orange) curves of Figure 75.

Curve	ρ(zo) [kg/m3]	ρ(zm) [kg/m3]	A [-]
min	1500	2650	0,000656
max	2050	2800	0,001127

For recreation of the exponential functions (Equ. 31, 32) of the density depth relationships (Figure 75) ρ(zo) and ρ(zm) were taken from Figure 74 and the empirical factor A was determined (Table 7). For the purpose of this thesis it is recommended to use the minimum curve for more shaly rock types and the max curve for more sandy rock types.

Density depth relationship for dry shaly clastic rocks:

$$\rho(z) = 1500 + (1500 - 2650) * (1 - e^{-0,00066*z}) \tag{34}$$

Density depth relationship for dry sandy clastic rocks:

$$\rho(z) = 2050 + (2050 - 2800) * (1 - e^{-0,00113*z}) \tag{35}$$

3.1.3.3 Influence on compressional- and shear wave velocity

Schön (1983) described after Figure 76 a nonlinear depth dependence of the velocity with strongly increasing velocities in the more shallow parts of the sedimentary column. Clay content strongly influences (shale, silt and shaly sandstone) elastic velocity with depth, whereas dense sandstones (salt, anhydrite and dolomite) show nearly no depth dependence.
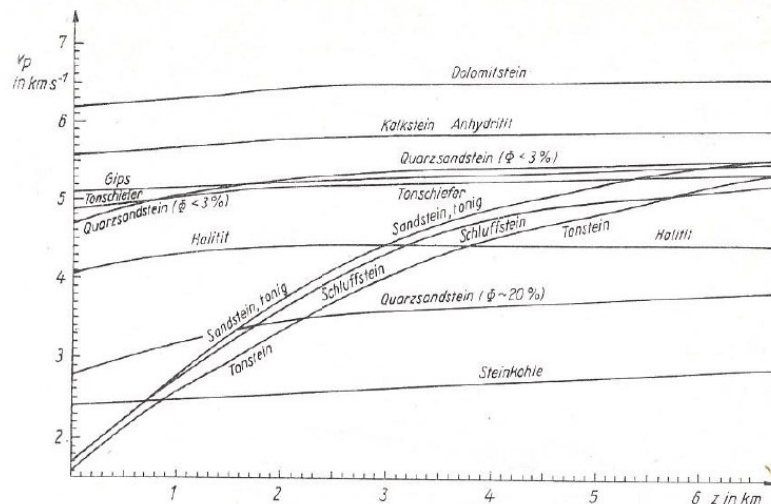
Figure 76: Velocity depth relationship for sediment rocks of the Norddeutsch-Polnisch Basin (Kopf, 1977)

The increase of velocity with depth is caused by the increased pressure on the rock skeleton (effective pressure). This causes a porosity decrease, increasing grain to grain contact and the closure of fractures (Schön, 2015). Schön (1996) implemented an equation (Equ. 33) for the velocity depth relationship for sediments with a granular structure. The factors a, b and m are empirical parameters and the exponent m is mostly in the order of 1/6 to 1/4.

$$V_p = a + b \cdot z^m \qquad (36)$$

Kirchberger (2011) investigated in a study on velocity depth relationships for sediments of the Vienna Basin (Figure 77). The results show different velocities for different deformation properties of sandstone and shale and different fluid properties. In case of the shear wave velocity a linear trend gives the best fit for shale (Schön, 2015).

Lithology	Compressional Wave	R^2	Shear Wave	R^2
Water sand	$V_P = 185 + 143 \cdot z^{0.41}$	0.82	$V_S = 42 + 36 \cdot z^{0.51}$	0.52
Gas sand	$V_P = 227 + 162 \cdot z^{0.38}$	0.79	$V_S = 72 + 58 \cdot z^{0.44}$	0.79
Shale	$V_P = 163 + 129 \cdot z^{0.42}$	0.92	$V_S = 393 + 0.76 \cdot z$	0.86

Figure 77: Compressional- and shear wave velocities [m/s] as a function of depth (Kirchberger, 2011).

Velocity depth trends for sandstone and shale from the North Sea were analyzed by Japsen et al. (2006). They show the increase of velocity with depth in relatively homogeneous, brine-saturated sedimentary formations as porosity is reduced during compaction.

Velocity–depth trends for the Bunter Shale by Japsen et al. (2006):

$$Vp = 1550 + 0.6z \qquad 0 < z < 1393\text{m} \qquad\qquad (37)$$

$$Vp = -400 + 2z \qquad 1393 < z < 2000\text{m} \qquad\qquad (38)$$

$$Vp = 2600 + 0.5z \qquad 2000 < z < 3500\text{m} \qquad\qquad (39)$$

$$Vp = 3475 + 0.25z \qquad 3500 < z < 5300\text{m} \qquad\qquad (40)$$

Where the velocities are in m/s.

Kopf (1977) shows a nonlinear increase of velocity with depth for magmatic rocks (Figure 78). This is mainly a result of the temperature dependence of elastic properties and (rock forming minerals, pore fluids) and a phase change of minerals (Schön, 2015).
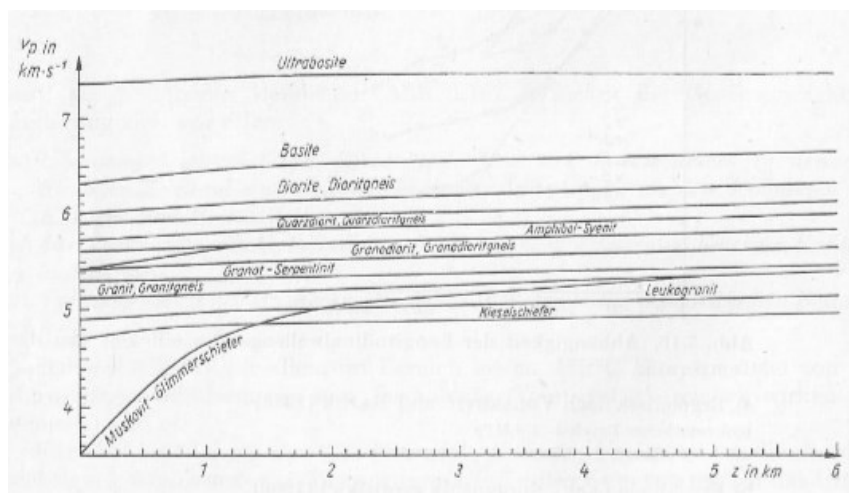
Figure 78: Velocity depth functions for magmatic and metamorphic rocks (Kopf, 1977)

3.2 Ranges of petrophysical parameters

3.2.1 Density

Porous sedimentary rocks show a broad range of density values, whereas pore free sediments (salt, anhydrite and dense carbonate) are only defined by their mineral composition (Figure 79). Some of them are even monomineralic like salt. Hence they show a very narrow range of density values. Porous sedimentary rocks are also influenced by porosity and saturation. The highest density values reflect low porosity sedimentary rocks and the lowest values high porosity and/or increasing gas content (Schön, 2015). Unconsolidated sediments show the lowest density due to grain-grain contacts and high porosity.
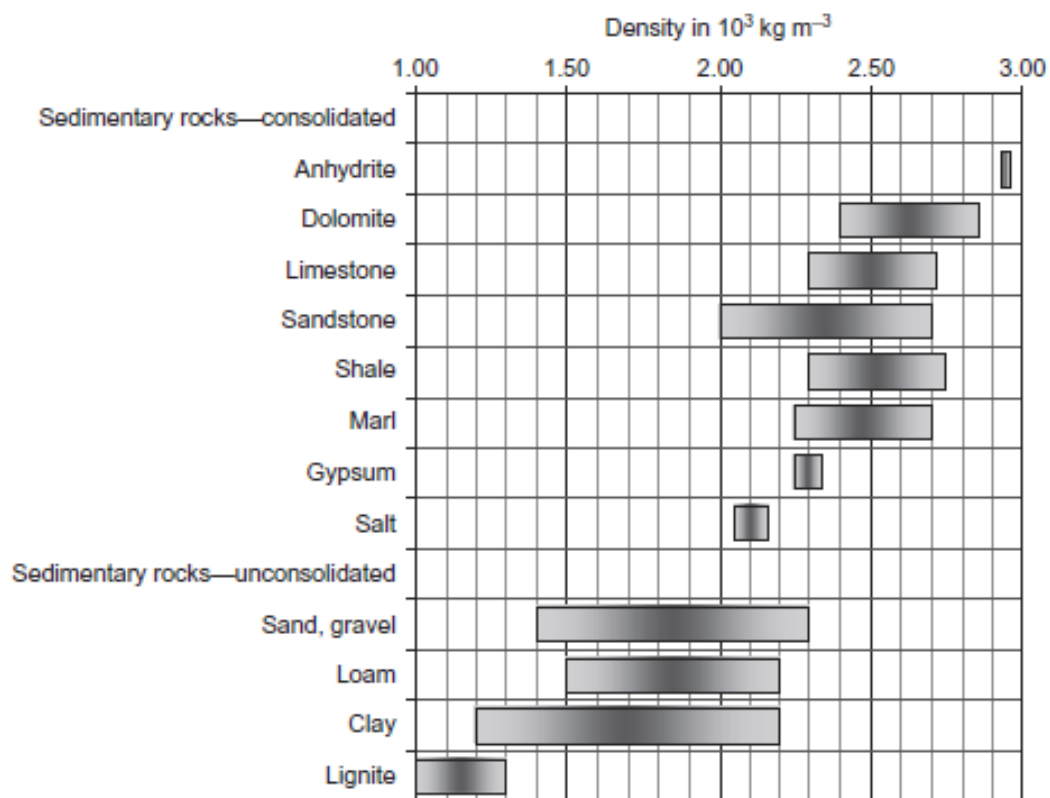
Figure 79: Mean range of density for sedimentary rocks (Schön, 2015).

Histograms of the density for the "main dolomite" (Figure 80) and "dachstein limestone" (Figure 81) are created from data provided by the petrophysical database of the Geophysical Institute of Leoben. The "main dolomite" is represented by 31 samples, which result in a slightly truncated normal distribution for the dry and a more random distribution for the saturated case by using eight bins. For the "dachstein limestone" a truncated normal distribution is shown due to

the higher number of 73 samples from the database represented in 12 bins. The histogram of the dachstein limestone shows one outlier with a dry density of 2,75 g/cm³ (saturated density of 2,80 g/cm³). This outlier may be a dolomite sample, because the mineral density of dolomite is around 2,84 g/cm³ (mineral density of limestone is around 2,71 g/cm³). For both rock types the histograms show higher densities for the saturated rocks compared to the dry. Densities of both rocks can be compared to the densities of dolomite and limestone (Figure 79) shown by Schön (2015).
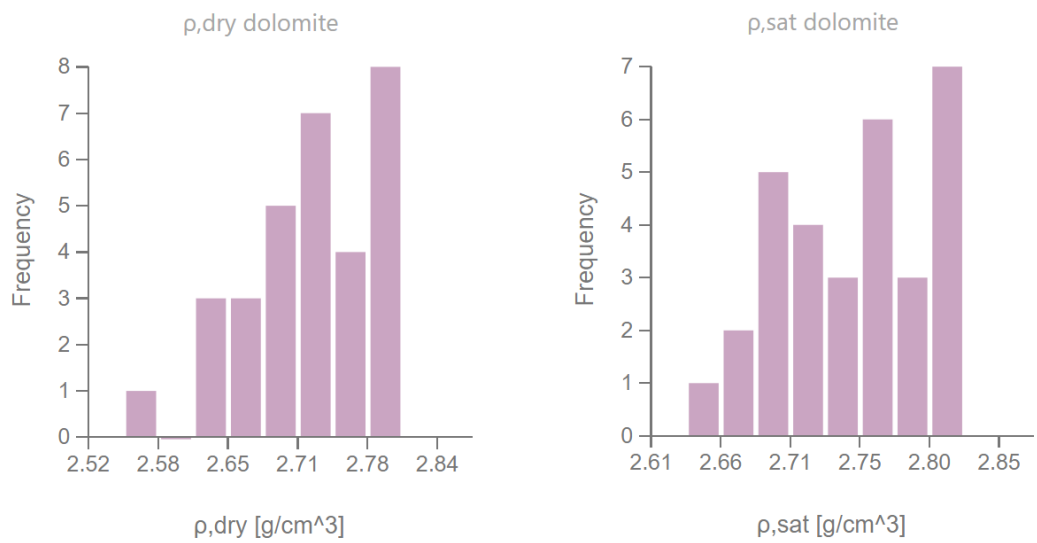
Figure 80: Histograms of the dry and saturated densities for the "main dolomite".
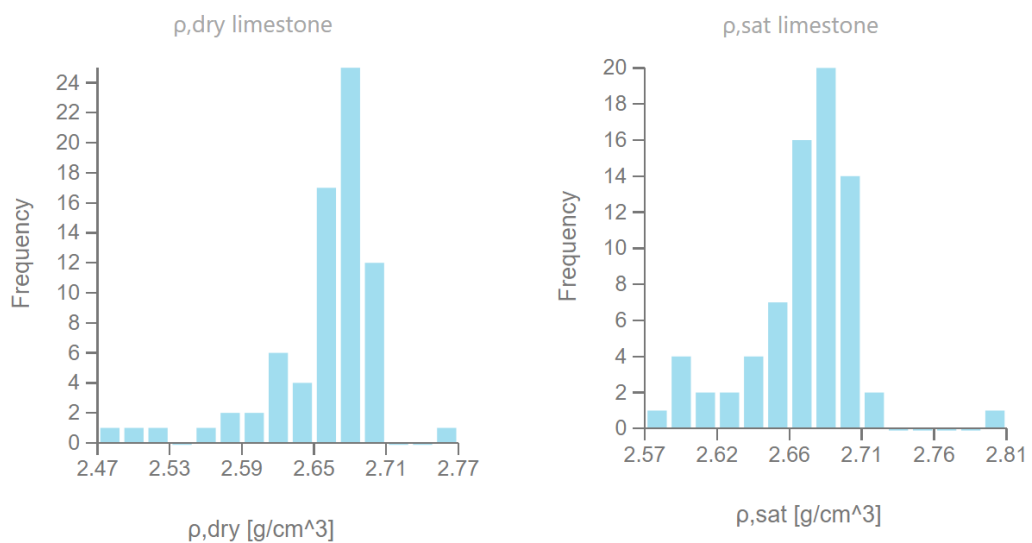
Figure 81: Histograms of the dry and saturated densities for the "dachstein limestone".

In comparison to sedimentary rocks the range of igneous rocks is much smaller (Figure 82). In general the density variation is more an influence of the rock composition than of pore- or fracture volume. The density values increase from felsic (acid) to mafic (basic) (Schön, 2015). For plutonic (intrusive) rocks density changes are mainly due to variations in the mineral composition and micro fractures. Volcanic (extrusive) rocks show a higher influence of porosity on density ranges (Schön, 1983).
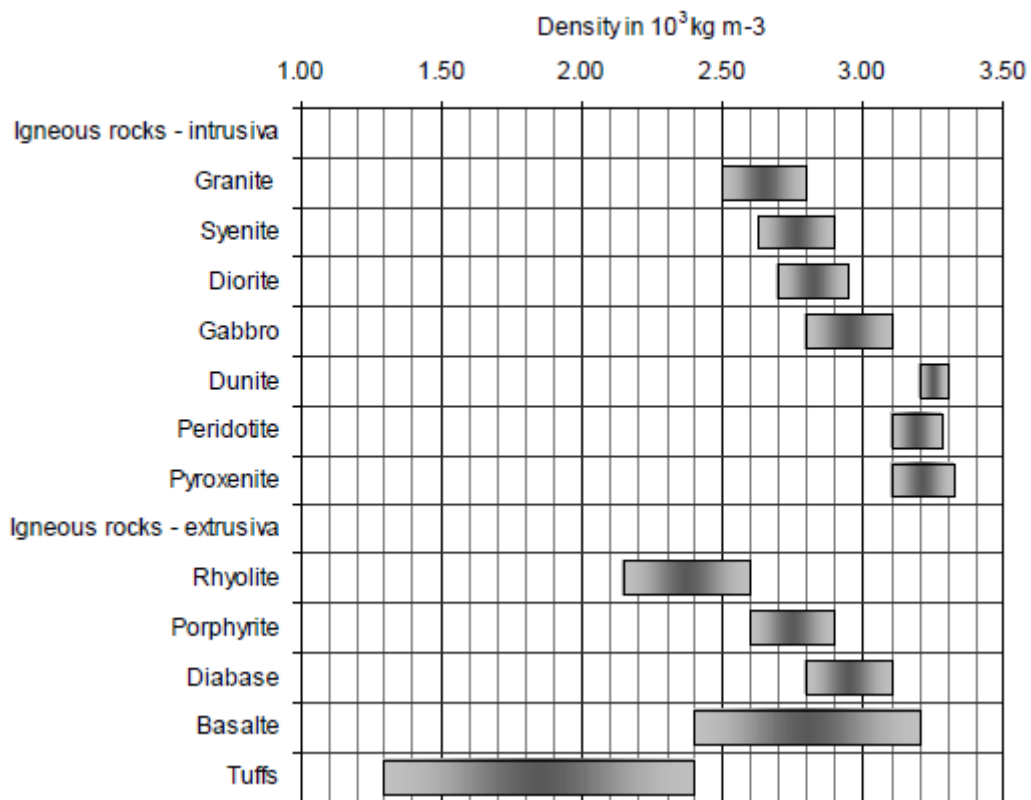
Figure 82: Mean ranges of density values for intrusive and extrusive igneous rocks (Schön, 2015)

3.2.2 Compressional- and shear wave velocity

The velocity of sedimentary rocks is low for dense or low porosity rocks and high for porous and/or gas bearing rocks (Figure 83). Dense rocks like (salt, anhydrite and dense carbonate) are only controlled by the mineral composition and have therefore very well defined density, especially in case of monomineralic rocks. Carbonates are further influenced by fracturing. The velocity of igneous rocks increases from felsic (acid) to mafic (basic). Due to higher porosities of extrusive igneous rocks compared to intrusiva, the velocities are lower.
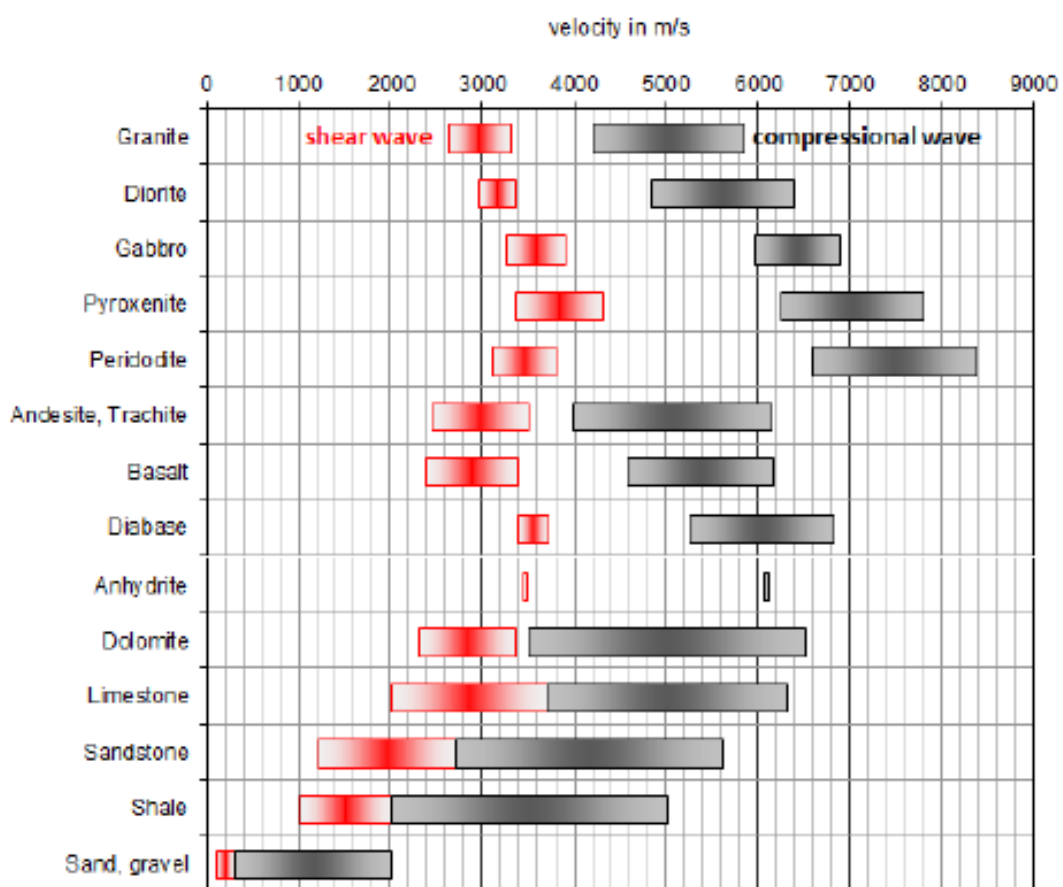
Figure 83: Mean ranges of velocity values for sedimentary and igneous rocks (Schön, 2015).

The compressional- and shear wave velocity ratio (Vp/Vs) is controlled by the rock type and pore fluid (Figure 84).
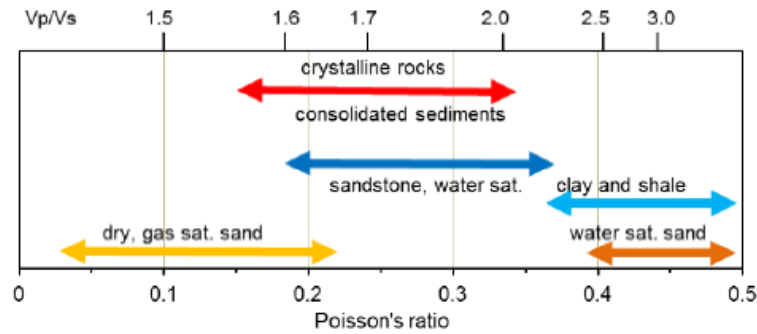
Figure 84: Average ratio Vp/Vs and Poisson's ratio for different rock types and fluid content (Schön, 2015 after Bourbie et al., 1987).

For the "main dolomite" (Figure 85, Figure 86) and "dachstein limestone" (Figure 87, Figure 88) histograms for the compressional- and shear wave velocities are created for dry and saturated case. The compressional- and shear wave velocity histograms for the main dolomite show gaps of an undersampled distribution. The histograms of the limestone velocities are more approximated to a truncated normal distribution, but more undersampled (in the area of lower velocities) than the density histograms. In general the compressional wave velocities are higher in case of saturation. For the shear wave velocities the histograms show lower velocities for the saturated rocks. The ranges of compressional- and shear wave velocities are comparable to mean ranges (Figure 83) shown by Schön (2015).
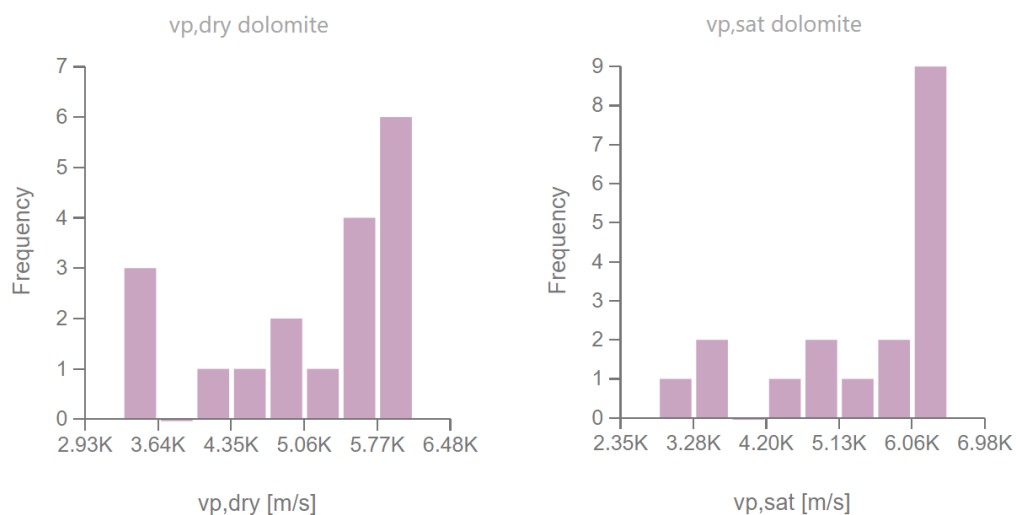
Figure 85: Histograms of the dry and saturated compressional wave velocities for the "main dolomite".
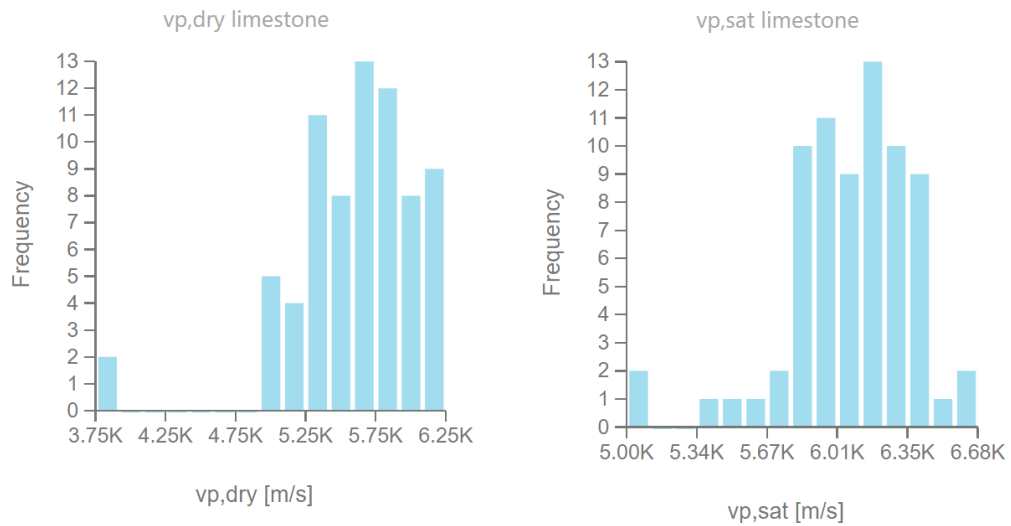
Figure 86: Histograms of the dry and saturated compressional wave velocities for the "dachstein lime-stone".
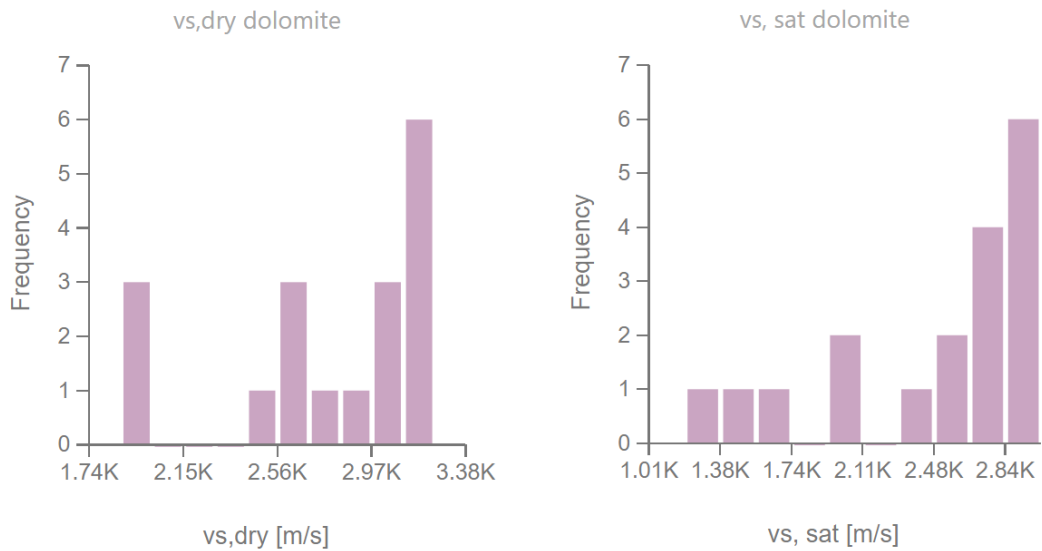
Figure 87: Histograms of the dry and saturated shear wave velocities for the "main dolomite".
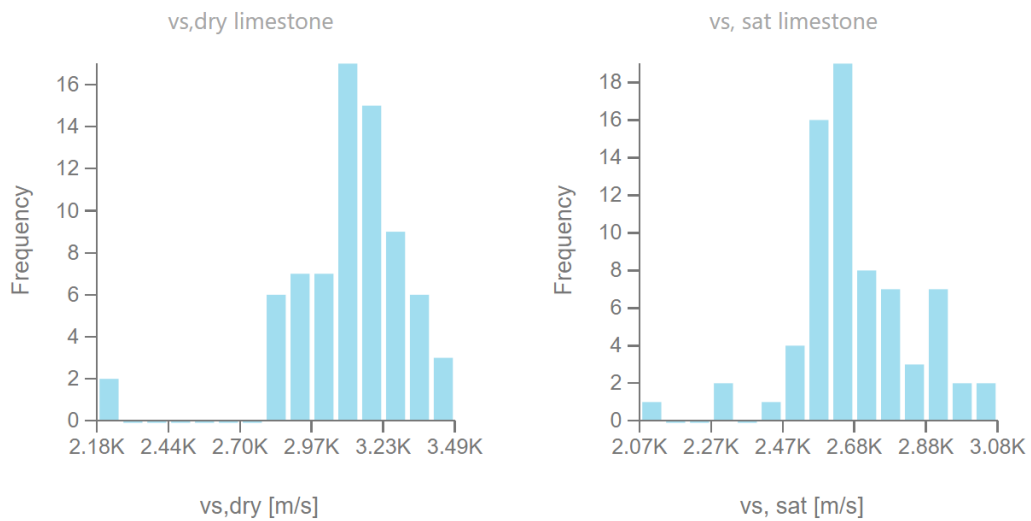
Figure 88: Histograms of the dry and saturated shear wave velocities for the "dachstein limestone".

3.2.3   Correlation between compressional- and shear wave velocity

In order to estimate shear wave velocity when only compressional wave velocity is available (and vice versa), Castagna et al. (1985) derived an empirical equation that is known as the "mudrock line":

$$V_s = 0.8621 \cdot V_p - 1.1724 \qquad (41)$$
$$V_p = 1.16 \cdot V_s + 1.36 \qquad (42)$$

where the velocities are in km/s .

In case of saturated carbonate rocks Castagna (1993) investigated following equations:

Limestone:

$$V_s = -0.055 \cdot V_p^2 + 1.017 \cdot V_p - 1.031 \qquad (43)$$
$$V_s = 0.5832 \cdot V_p - 0.07776 \qquad (44)$$

All of these correlations are pure empirically and valid only for a specific formation.

3.2.4 Correlation between density and velocity

Gardner (1974) derived an empirical relationship between density and velocity, used to transform velocity to density and vice versa. The equation represents an average over different brined saturated rocks (except evaporates). The relationship shows a nonlinear increase of density with increasing density (Figure 89).

$$\rho_b \approx 1.741 \cdot V_P^{0.25} \quad where\ \rho_b\ is\ in\ g\ cm^{-3}\ and\ V_P\ is\ in\ km\ s^{-1} \tag{45}$$

$$\rho_b \approx 0.23 \cdot V_P^{0.25} \quad where\ \rho_b\ is\ in\ g\ cm^{-3}\ and\ V_P\ is\ in\ ft\ s^{-1} \tag{46}$$
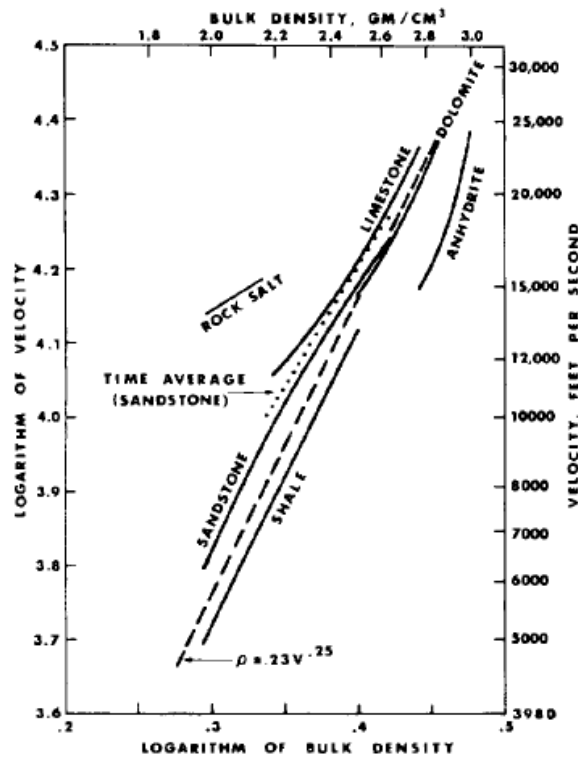
Figure 89: Velocity density relationship for brine saturated sedimentary rocks (Gardner, 1974).

Gardner (1974) and Castagna (1993) suggest a more lithological dependent form of the Gardner equation:

$$\rho_b = d \cdot V_p^{f} \tag{47}$$

where d and f are empirical parameters (Figure 90).

Rock Type	d	f	V_p (km s^{-1})
Sandstone	1.66	0.261	1.5–6.0
Limestone	1.50	0.225	3.5–6.4
Dolomite	1.74	0.252	4.5–7.1
Anhydrite	2.19	0.160	4.6–7.4
Shale	1.75	0.265	1.5–5.0

Figure 90: Coefficients for the Gardner Equation (Schön, 2015 after Castagna, 1993 and Mavko, 1998).

For dense igneous rocks (not fractured) the velocity is controlled by the mineral composition and therefore correlates with the density shown by Figure 91. Velocity and density generally increase from acid/felsic to basic/mafic (Schön, 2015).
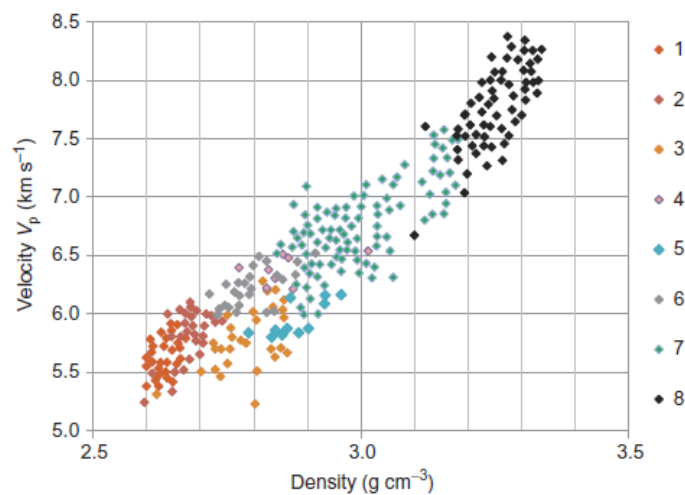
Figure 91: Velocity density relationship for magmatic and metamorphic rocks. 1: Granite, 2: Gneiss (Biotitic, Amphibolic), 3: Gneiss (Garnet-Biotitic), 4: Amphibole, Gneiss (Amphibolic), 5: Granulite, 6: Diorite, 7: Gabbro-Norite and 8: Ultrabasite. Schön, 2015 after Dortman, 1976.

The velocity density relationship for igneous rocks was first published by Birch (1960, 1961):

$$V_p = 2.76 \cdot \rho - 0.98 \qquad (48)$$

where the density is in 10³ kg/m^{-3} and the velocity is in km s^{-1}.

Gebrande et al. (1982) showed compressional- and shear wave velocities (km/s) for plutonic and volcanic rocks:

For plutonic rocks:

$$V_p = 4.36 \cdot \rho - 6.73 \pm 0.03 \quad V_s = 1.66 \cdot \rho - 1.48 \pm 0.06 \tag{49}$$

For volcanic rocks:

$$V_p = 2.81 \cdot \rho - 2.37 \pm 0.18 \quad V_s = 1.46 \cdot \rho - 1.02 \pm 0.22 \tag{50}$$

Christensen and Salisbury (1975) investigated nonlinear velocity density relations for basalts recovered in the Deep Sea Drilling Project (50kPa):

$$V_p = 2.33 + 0.08 \cdot \rho^{3.63} \tag{51}$$

$$V_s = 1.33 + 0.011 \cdot \rho^{4.85} \tag{37}$$

The pressure for these measurements was 0.5 bar (=50 kPa).

If igneous rocks are fractured, velocity and density will decrease.

4 Fact Sheets

The top of each fact sheet an example from literature (left) compared to the final model (right) is shown. Each number represents an own facies compound and for every facies compound the facies description, measurements and petrophysical properties are listed in the fact sheet.

4.1 Channel

4.1.1 Braided River (Proximal)

LITERATURE

Modified after Nichols, 2009

PETREL MODEL

FACIES COMPOUNDS

(1) **Channel Fill**

(2) **Floodplain/ Overbank deposits**

FACIES DESCRIPTION

(1) Channel fill of longitudinal gravel bar deposits and transverse cross-bedded sand bar deposits fining up.

(2) Floodplain deposits surround the belt of the channel fill and associated facies; mainly clay and silt-sized debris.

FACIES MEASUREMENTS

Facies	Width [m]	Thickness [m]
(1)	500 - 1000	5 - 10

PETROPHYSICAL PROPERTIES OF EACH FACIES COMPOUND

PARAMETERS	(1)	(2)
LITH	sandy congl	claystone
Log Pattern	minor fining up	-
ρ [kg/cm³]	2000-2700	2300-2750
Vp [m/s]	2800-5600	2000-5000
Vs [m/s]	1200-2800	1000-2000
Φ [%]	20-25	5-15
Vsh [%]	0-10	90-100
Fluids	gas/oil/water	gas/oil/water

Figure 92: Fact Sheet of a braided river (proximal to the origin) represented by seismic facies.

4.1.2   Braided River (Distal)

LITERATURE

Modified after Nichols, 2009

PETREL MODEL

FACIES COMPOUNDS

1. **Channel Fill**

2. **Floodplain/ Overbank deposits**

FACIES DESCRIPTION

1. Channel fill of longitudinal gravel bar deposits and transverse cross-bedded sand bar deposits fining up.

2. Floodplain deposits surround the belt of the channel fill and associated facies; mainly clay and silt-sized debris.

FACIES MEASUREMENTS

Facies	Width [m]	Thickness [m]
1	200 - 500	2 - 6

PETROPHYSICAL PROPERTIES OF EACH FACIES COMPOUND

PARAMETERS	1	2
LITH	gravelly sdst	clayst
Log Pattern	minor fining up	-
ρ [kg/cm³]	2000-2700	2300-2750
Vp [m/s]	2800-5600	2000-5000
Vs [m/s]	1200-2800	1000-2000
Φ [%]	15-25	5-15
Vsh [%]	0-10	90-100
Fluids	gas/oil/water	gas/oil/water

Figure 93: Fact Sheet of a braided river (distal to the origin) represented by seismic facies.

4.1.3 Meandering River (Proximal)

LITERATURE	PETREL MODEL

Modified after Nichols, 2009

FACIES COMPOUNDS

① Channel Fill   ③ Crevasse Splay

② Levee   ④ Floodplain/ Overbank deposits

FACIES DESCRIPTION

① Channel fill point bar sands are the thickest sand bodies. Cross-bedded and cross-laminated sands fining-up.

② Natural levee sandy muds at the channel edge; higher than the level of the floodplain.

③ Crevasse splay lobes of upward coarsening sediment; formed if levee breaks and water flows out onto the floodplain.

④ Floodplain deposits surround the belt of the channel fill and associated facies; mainly clay and silt-sized debris.

FACIES MEASUREMENTS

Facies	Width [m]	Thickness [m]
①	100 - 200	1 - 5
②	20 - 140	0,5 – 0,9
③	150 – 450	0,5 - 2

PETROPHYSICAL PROPERTIES OF EACH FACIES COMPOUND

PARAMETERS	①	②	③	④
LITH	gravelly muddy sdst	sandy mudst	muddy sdst	clayst
Log Pattern	fining up	-	coarsening up	-
ρ [kg/cm³]	2000-2700	2000-2300	2000-2700	2300-2750
Vp [m/s]	2800-5600	2000-2800	2800-5600	2000-5000
Vs [m/s]	1200-2800	1000-1200	1200-2800	1000-2000
Φ [%]	10-25	5-15	10-25	5-15
Vsh [%]	10-30	50-90	10-50	90-100
Fluids	gas/oil/water	gas/oil/water	gas/oil/water	gas/oil/water

Figure 94: Fact Sheet of a meandering river (proximal to the origin) represented by seismic facies.

4.1.4 Meandering River (Distal)

LITERATURE	F MODEL

Modified after Nichols, 2009

FACIES COMPOUNDS

① **Channel Fill**   ③ **Crevasse Splay**

② **Levee**   ④ **Floodplain/ Overbank deposits**

FACIES MEASUREMENTS

Facies	Width [m]	Thickness [m]
①	50 - 100	1 - 5
②	15 - 70	0,5 – 4,5
③	150 – 450	0,5 - 1

FACIES DESCRIPTION

① Channel fill point bar sands are the thickest sand bodies. Cross-bedded and cross-laminated sands fining-up.

② Natural levee sandy muds at the channel edge; higher than the level of the floodplain.

③ Crevasse splay lobes of upward coarsening sediment; formed if levee breaks and water flows out onto the floodplain; thin deposits

④ Floodplain deposits surround the belt of the channel fill and associated facies; mainly clay and silt-sized debris.

PETROPHYSICAL PROPERTIES OF EACH FACIES COMPOUND

PARAMETERS	①	②	③	④
LITH	gravelly muddy sdst	sandy mudst	muddy sdst	clayst
Log Pattern	fining up	-	coarsening up	-
ρ [kg/cm³]	2000-2700	2000-2300	2000-2700	2300-2750
Vp [m/s]	2800-5600	2000-2800	2800-5600	2000-5000
Vs [m/s]	1200-2800	1000-1200	1200-2800	1000-2000
Φ [%]	15-25	5-15	15-25	5-15
Vsh [%]	20-50	50-90	10-50	90-100
Fluids	gas/oil/water	gas/oil/water	gas/oil/water	gas/oil/water

Figure 95: Fact Sheet of a meandering river (distalto the origin) represented by seismic facies.

4.2 Submarine Fan (sand rich system)

LITERATURE

Nichols, 2009

PETREL MODEL

FACIES COMPOUNDS

(1) Proximal fan channel/levee

(3) Distal lobe

(2) Medial fan

(4) Basin plain

FACIES MEASUREMENTS

Facies	Width [km]	Length [km]	Thickness [m]
(1)	0,05-0,1	0,05-0,1	3-5
(2)	2-3,5	3-5	1,5-2
(3)	10-15	20-30	3-5

FACIES DESCRIPTION

(1) Submarine fan channel filled with thick conglomerate and sandstone turbidites fining up. Overlay thin bedded levee deposits.

(2) Coarsening up succession of sandy turbidites.

(3) Thin and fine grained turbidites.

PETROPHYSICAL PROPERTIES OF EACH FACIES COMPOUND

PARAMETERS	(1)	(2)	(3)	(4)
LITH	gravelly sdst	muddy sdst	sandy mudst	clayst
Log Pattern	fining up	> coarsening up	< coarsening up	-
ρ [kg/cm³]	2000-2700	2000-2700	2000-2300	2300-2750
Vp [m/s]	2800-5600	2800-5600	2000-2800	2000-5000
Vs [m/s]	1200-2800	1200-2800	1000-1200	1000-2000
Φ [%]	15-25	15-25	5-15	5-15
Vsh [%]	0-10	10-50	50-90	90-100
Fluids	gas/oil/water	gas/oil/water	gas/oil/water	gas/oil/water

Figure 96: Fact Sheet of a sand rich submarine fan represented by seismic facies.

4.3 Salt Dome

LITERATURE	PETREL MODEL
Modified after Ortlam, 2001	

FACIES COMPOUNDS

(1) **Salt Dome**

(2) **Sedimentary Cover:**

Yellow	Grey	Blue	Purple	Pink	Red	Black
sdst	clst	lmst	marlst	salt	porphyr	coal

FACIES MEASUREMENTS

Facies	Height [m]	Diameter thickest part [m]	Diameter thinnest part [m]
(1)	5000	1600	600

FACIES DESCRIPTION

Rock salt is soluble, weak and easily mobilized by solid-state flow. It remains almost incompressible throughout burial and metamorphism.

Salt structures evolve from concordant, low amplitude structures (immature) to high amplitude intrusions (mature).

Salt stocks (mature) vary in shape from squat to columnar and can be conical or barrel-shape. If the top of a diaper swells sideways it is called a "bulb". The "overhang" is part of the bulb and is wider than the stem.

PETROPHYSICAL PROPERTIES OF EACH FACIES COMPOUND

PARAMETERS	(1)	(2)					
LITH	salt/ salt dome	sdst	clayst	lmst	marl	porphyr	coal
ρ [kg/cm³]	2160	2000-2700	2300-2750	2300-2700	2100-2600	2700-2800	1300-1800
Vp [m/s]	4560	2800-5600	2000-5000	3700-6300	2000-3000	4700-5800	2200-2700
Vs [m/s]	2560	1200-2800	1000-2000	2000-3700	750-1500	3000-3600	1000-1400
Φ [%]	-	20-25	5-15	1-10	5-20	-	-
Vsh [%]	-	0-10	90-100	-	35-65	-	-
Fluids	-	water	water	water	water	-	-

Figure 97: Fact Sheet of a salt dome and the surrounding sedimentary column represented by seismic facies.

4.4 Reef

LITERATURE

Modified after Da Silva, 2004

PETREL MODEL

FACIES COMPOUNDS

1. Inner Lagoon
2. Outer Lagoon
3. Reef Core
4. Forereef and Slope
5. Mound Stage
6. Open Shelf

FACIES DESCRIPTION

1. 2. Inner lagoon comprises mudstone/wackstone and outer lagoon laminar wackstone/packstone, where they form horizontal beds.

3. The reef core is also referred as the high energy zone where massive coral framework with skeletal grainstone or rudstone occur.

4. The forereef and slope comprise coarse skeletal packstone from the reef core as well as wackstone.

5. The Open Shelf is mainly a place for fine-grained mudstone deposits.

FACIES MEASUREMENTS

Facies	Width [m]	Max.Thickness [m]
1	100 - 2000	10
2	5	15
3	100 - 2000	8

PETROPHYSICAL PROPERTIES OF EACH FACIES COMPOUND

PARAMETERS	1	2	3	4	5
LITH	mudst/wackst	wackst/grainst	rudst/grainst/boundst	packst/grainst	mudstone
ρ [kg/cm³]	2300-2700	2300-2700	2300-2700	2300-2700	2300-2750
Vp [m/s]	3700-6300	3700-6300	3700-6300	3700-6300	2000-5000
Vs [m/s]	2000-3700	2000-3700	2000-3700	2000-3700	1000-2000
Φ [%]	5-15	20-40	20-50	5-15	5-15
Vsh [%]	80-95	50-90	0-30	0-30	90-100
Fluids	gas/oil/water	gas/oil/water	gas/oil/water	gas/oil/water	gas/oil/water

Figure 98: Fact Sheet of a reef (proximal to the origin) represented by seismic facies.

4.5 Karst

4.5.1 Main Dolomite

LITERATURE

Modified after Virag et al, 2013

PETREL MODEL

FACIES COMPOUNDS

1. Limestone
2. Claystone
3. Marl (10% karstified)
4. Limestone (20% karstified)
5. Conglomerate (10% karstified)
6. Main Dolomite (10% karstified)

FACIES DESCRIPTION

FACIES MEASUREMENTS (Caves)

Caves	Facies	Width [m]	Length [m]	Thickness [m]
Small	1 2 3 4	10-500	10-1000	10-100
Large (1)	2	500-1500	1000-7500	50-130

PETROPHYSICAL PROPERTIES OF EACH FACIES COMPOUND

PARAMETERS	①	②	③	④	⑤	⑥ Main dolomite	
						dry	sat
LITH	lmst	clst	marl	lmst	congl	dry	sat
ρ [kg/cm³]	2300-2700	2300-2750	2100-2600	2300-2700	2000-2700	2550-2800	2600-2800
Vp [m/s]	3700-6300	2000-5000	2000-3000	3700-6300	2800-5600	3300-6100	2800-6500
Vs [m/s]	2000-3700	1000-2000	750-1500	2000-3700	1200-2800	1900-3200	1200-3000
Φ [%]	10-50	5-15	5-20	1-10	20-25	0,3-11	0,3-11
Vsh [%]	-	90-100	35-65	-	0-10	-	-
Fluids	gas/water	gas/water	gas/water	gas/water	gas/water	gas	water

Figure 99: Fact Sheet of a karst body ("main dolomite") represented by seismic facies.

4.5.2 Dachstein Limestone

LITERATURE	PETREL MODEL

Modified after Virag et al, 2013

FACIES COMPOUNDS

① Limestone
② Claystone
③ Marl (10% karstified)
④ Limestone (20% karstified)
⑤ Conglomerate (10% karstified)
⑥ Main Dolomite (10% karstified)

FACIES DESCRIPTION

FACIES MEASUREMENTS (Caves)

Caves	Facies	Width [m]	Length [m]	Thickness [m]
Small	① ② ③ ④	10-500	10-1000	10-100
Large (1)	②	500-1500	1000-7500	50-130

PETROPHYSICAL PROPERTIES OF EACH FACIES COMPOUND

PARAMETERS	①	②	③	④	⑤	⑥	
						Dachstein lmst	
LITH	lmst	clst	marl	lmst	congl	dry	sat
ρ [kg/cm³]	2300-2700	2300-2750	2100-2600	2300-2700	2000-2700	2500-2800	2700-2800
Vp [m/s]	3700-6300	2000-5000	2000-3000	3700-6300	2800-5600	3750-6300	5000-6700
Vs [m/s]	2000-3700	1000-2000	750-1500	2000-3700	1200-2800	2200-3500	2050-3100
Φ [%]	10-50	5-15	5-20	1-10	20-25	0,2-14	0,2-14
Vsh [%]	-	90-100	35-65	-	0-10	-	-
Fluids	gas/water	gas/water	gas/water	gas/water	gas/water	gas	water

Figure 100: Fact Sheet of a karst body ("dachstein limestone") represented by seismic facies.

4.6 **Volcano (Andesitic Stratovolcano)**

LITERATURE

Modified after Bogie et. al, 1998

PETREL MODEL

FACIES COMPOUNDS

① **Central Zone**   ③ **Medial Zone**

② **Proximal Zone** ④ **Distal Zone**

FACIES MEASUREMENTS

Facies	Distance [m]	Max. Height[m]
①	1250	3000
②	1250-3000	3000
③	3000-7000	1000
④	7000-10000	500

FACIES DESCRIPTION

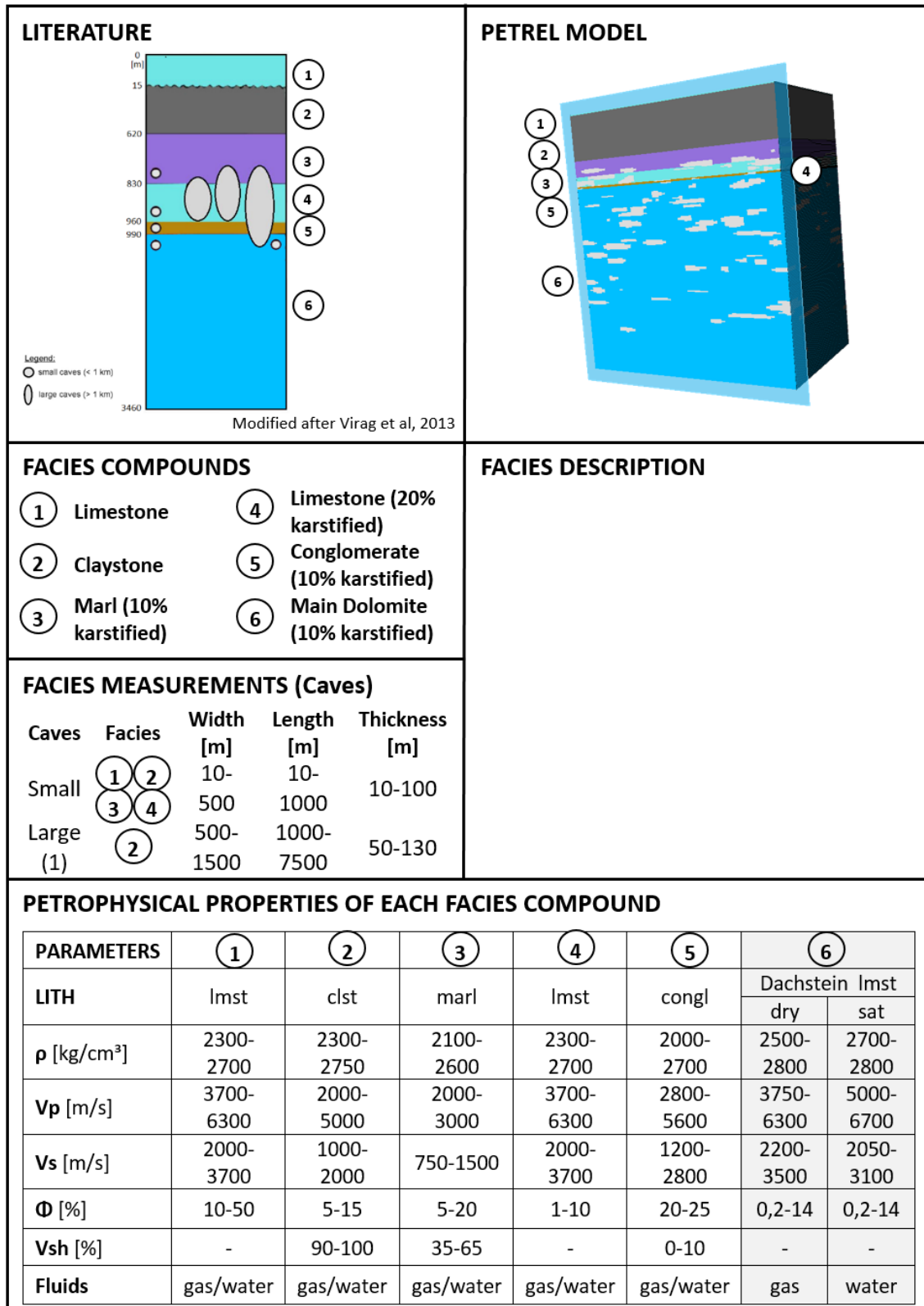① Core Facies at the vent mainly comprises lava domes and thick bended lavas as well as dykes, sills and stocks.

② Proximal Facies is located at the slope and is made up mainly of thick lava and coarse-grained pyroclastic breccia.

③ Medial Facies is part of the outer flanks. Lahars with blocks up to 10m are intercalated in pyroclastic deposits (lapilli to coarse ash grain size).

④ Distal facies at the base of a volcano has a great lateral continuity. Epiclastics dominate.

PETROPHYSICAL PROPERTIES OF EACH FACIES COMPOUND

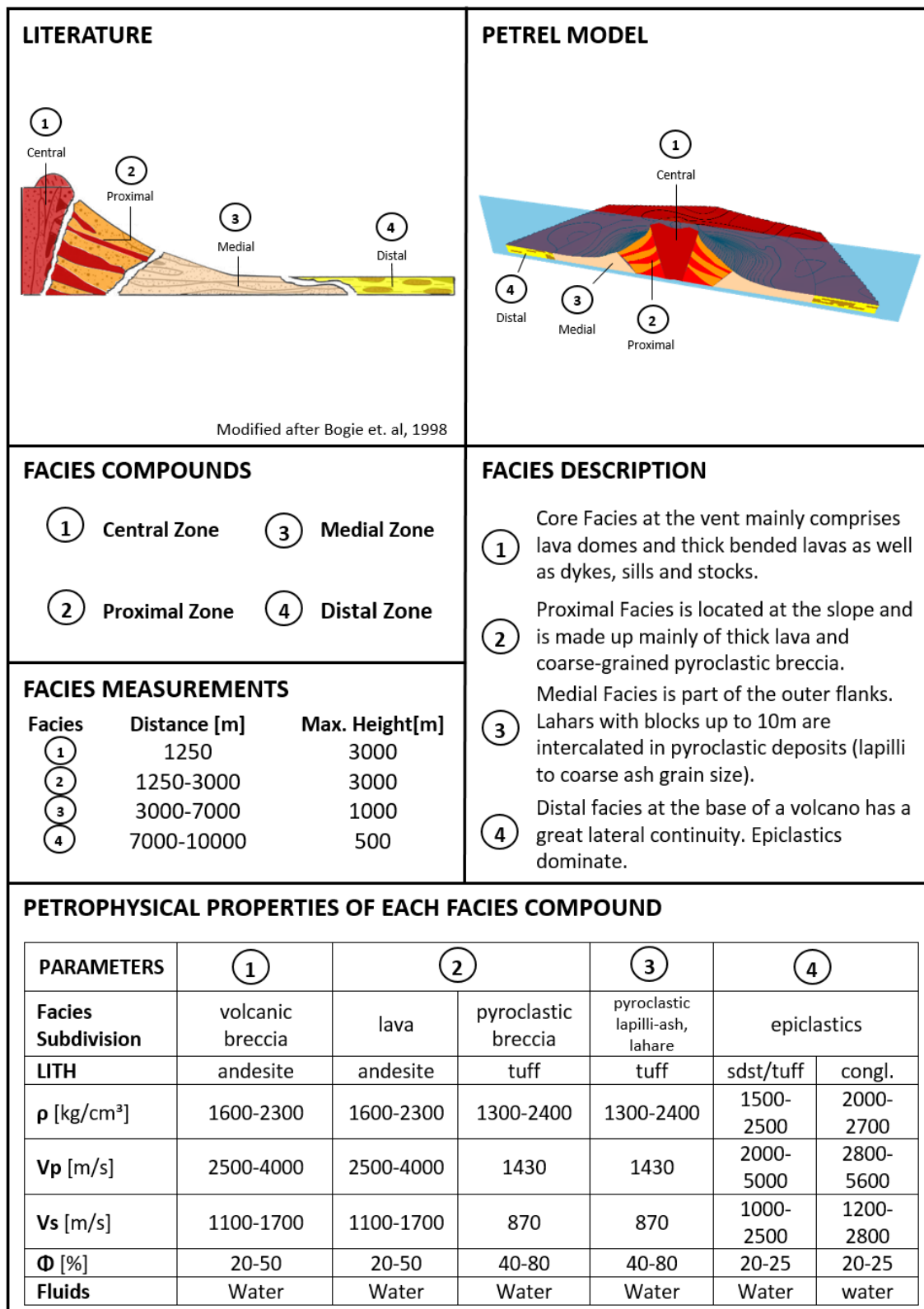| PARAMETERS	①	②	③	④	
Facies Subdivision	volcanic breccia	lava	pyroclastic breccia	pyroclastic lapilli-ash, lahare	epiclastics	
LITH	andesite	andesite	tuff	tuff	sdst/tuff	congl.
ρ [kg/cm³]	1600-2300	1600-2300	1300-2400	1300-2400	1500-2500	2000-2700
Vp [m/s]	2500-4000	2500-4000	1430	1430	2000-5000	2800-5600
Vs [m/s]	1100-1700	1100-1700	870	870	1000-2500	1200-2800
Φ [%]	20-50	20-50	40-80	40-80	20-25	20-25
Fluids	Water	Water	Water	Water	Water	water

Figure 101: Fact Sheet of an andesitic stratovolcano represented by seismic facies.

5   Conclusion and Discussion

It can be concluded, that Object Modeling is the best and fastest way for modeling channels, because it has an already provided step by step workflow for modeling fluvial systems. The software also offers other stochastic tools for modeling, but due to the simplicity, Object Modeling is recommended. The limitation of this stochastic method is the randomly placement of objects. The user has an influence on the fraction of the object on the whole facies model and can include trend maps, but detailed reconstructions of geological situations are not possible. If well data is available it is possible to fit facies along the wells to increase the realistic result. For this study no well data is available and placement can only be influenced by trend maps. Compared to other stochastic methods it is the only method that allows facies modeling without existing well data. Another advantage of object modeling compared to the other stochastic methods is, that the geometry of the objects can be defined deterministically beside the stochastic way. Due to the good applicability to fluvial and lobe system, four fluvial channels (two braided rivers and two meandering rivers) and one submarine fan were modeled and there workflow shown under Method I – "Object Modeling" Workflow. Although "Object Modeling" has the opportunity to link facies to each other, it fails for complex internal structures like the reef that consists of six different facies types which need to be in a specific order and place. While "Object Modeling" provides several different body shapes it is still limited. Object modeling does not provide a cone shape for the volcanic center and neither ring structures to model the proximal, medial and distal volcanic zones. This is also the case for the salt dome, which mushroom like shape is not provided by "Object Modeling".

For facies models that have a complex architecture and where geometrical objects need to be defined deterministically the provided methods fail. Method II is able to solve this issue, but with the limitation of nearly symmetrical facies models, because profiles are placed radial around a center. Due to the complexity of the facies models an own 3D grid for each facies needs to be constructed. In very complicated cases, like the reef, it is necessary to generate more than one 3D grid per facies. Problems in the Fault Model can create gaps and other irregularities in the grid. To minimize them, the fault model needs to be edited and pillar gridding run again to achieve an acceptable result. This can be an iterative process and in case of complex architecture quite time consuming. Another new idea is the integration of Method II in Method I. This is done by populating objects, which are defined under Object Modeling, randomly in one of the facies

created by Method II. An example is the integration of caves in several facies of the karst model. Trends of the objects can be further applied by using trend maps. Beside all the new possibilities created with this method it can be, depending on the complexity of the model, a very time consuming process, which needs to be considered. Method II can be used for future work to recreate the models shown by this study or investigate on new models, where well data is not available.

The facies models created by this study will be used for forward modeling and clustering tests in combination with seismic attributes in further work of the GeoSegment3D research project.

For future property modeling, which needs to be realised in front of seismic forward modeling, ranges of petrophysical parameters are listed in tables for the main lithologies, which are linked to facies. It needs to be considered that empirical relationships between petrophysical parameters are representative for specific petrographic groups and are generally not representative for other regional or stratigraphic areas (Kopf, 1977). In case of this master thesis no real data exists and approximations need to be taken. This study shows a gap in investigations for depth dependence on petrophysical parameters, especially when it comes to porous igneous rocks (extrusiva).

Fact sheets for each facies model provide an overview of the geometrical inputs of each facies and list ranges of petrophysical parameters. These fact sheets represent the summary of this work and show all necessary inputs. They provide a new and easy way to show the link between facies, lithology and their petrophysical parameters for typical geological bodies and can be used as a basis for further work of building geological models. The types of fluids listed in the fact sheets indeed indicate an influence on density, compressional- and shear wave velocity, but not the degree of influence. Only in case of the "main dolomite" and "dachstein limestone" seismic properties are listed for the dry and water saturated case. For future work, the fact sheets can be extended by showing ranges of petrophysical parameters for each case of fluid fill (gas, oil and water).

References

Bogie, I. and Mackenzie, K. [1998] The application of a volcanic facies model to an andesitic stratovolcano hosted geothermal system at Wayang Windi, Java, Indonesia. *Proceedings of the 6th Petroleum Geology Conference.*

Bourbié, T., Coussy, O. and Zinszner, B. [1987] *Acoustics of porous media*. Éditions Technip, Paris.

Da Silva, A. [2004] From paleosols to carbonate mounds: facies and environments of the Middle Frasnian platform in Belgium. *Geological Quarterly*, **48**, 253–266.

Nichols, G. [2009] *Sedimentology and Stratigraphy*. Wiley-Blackwell, West Sussex.

Ortlam, D. [2001] Geowissenschaftliche Erkenntnisse über den Untergrund Bremerhavens in ihrer wirtschaftlichen Bedeutung. *Bremisches Jahrbuch*, **80**, 181-197.

Schön, J.H. [2015] *Physical Properties of Rocks: Fundamentals and Principles of Petrophysics*. Elsevier, Amsterdam.

Virág, M., Kálmánfi-Ast, H., and Mindszenty, A. [2013] *Földtani értékek és az ember Spatial: Characterization of cave levels, cave minerals and travertines*. ELTE Eötvös Kiadó, Budapest.

Reading, H.G. and Levell, B.K. [1996*] Sedimentary Environments: Processes, Facies and Stratigraphy*. Blackwell Science, Oxford.

Walther, J. [1893-4] *Einleitung in die Geologie als historische Wissenschaft*. Verlag von Gustav Fisher, Jena.

Bacon, M., Simm, R., and Redshaw, T. [2003] *3D seismic interpretation*. Cambridge University, Press.

Emery, D. and Myers, K. J. [1996] *Sequence Stratigraphy*. Blackwell Science, Oxford, UK.

Goovaerts, P. [1997] *Geostatitics for natural resources evaluation*. Oxford University Press, New York.

Strebelle, S. and Zhang, T. [2004] *Non-stationary multiple-point geostatistical models*. Banff, Canada.

Strebelle, S., Payrazyan, K., and Caers, J. [2003] Modeling of a deepwater turbidite reservoir conditional to seismic data using principal component analysis and multiple-point geostatistics. *SPE Journal*, **8**, 227–235.

Levy, M., Harris, P., Strebelle, S., and Rankey, E. [2008] *Geomorphology of carbonate systems and reservoir modeling: Carbonate training images, fdm cubes, and mps simulations*. Long Beach, CA.

Fjaer, E., R.M. Holt, P. Horsrud, A.M. Raaen, and R. Rines. [2008] *Petroleum related rock mechanics*. Elsevier Science Publ., Amsterdam.

Prelat, A., Hodgson, D., and Flint, S. [2009] Evolution, architecture and hierarchy of distributary deep-water deposits: a high-resolution outcrop investigation of submarine lobe deposits from the permian karoo basin, south africa. *Sedimentology*, **56**, 2132–2154.

Arrhenius, S. [1912] Zur Physik der Salzlagerstätten. *Meddelanden Vetenskapsakademiens Nobelinstitut*, **2**, 1-25.

Jackson, M. and Talbot, J.C. [1986] External shapes, strain rates, and dynamics of salt structures. *Geological Society of Americal Bulletin*, **97**, 305-323.

Pyrcz, M.J. and Deutsch C.V. [2014] *Geostatistical Reservoir Modeling*. Oxford University Press, New York.

Appendix A
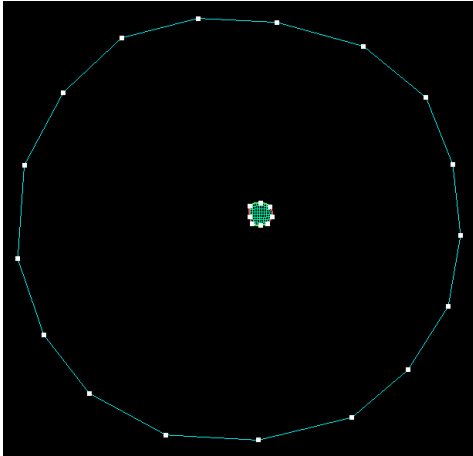
Figure 102: Faults that marge the inner lagoon were used for creating the 3D grid. The inner lagoon is represented by the green mid skeleton.
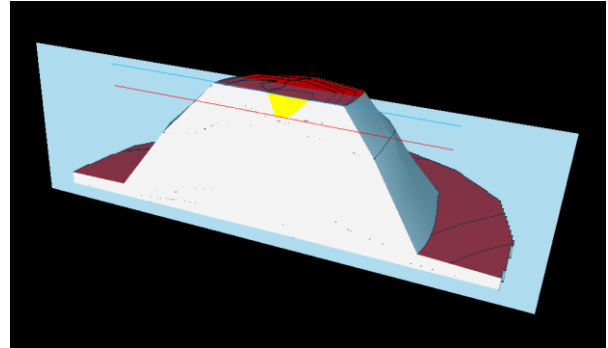
Figure 103: Inner lagoon (yellow zonation) with top and bottom horizons (marked as straight lines). Remaining reef is indicated as grey zonation.
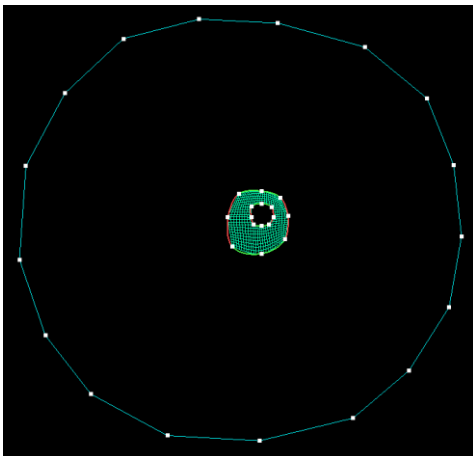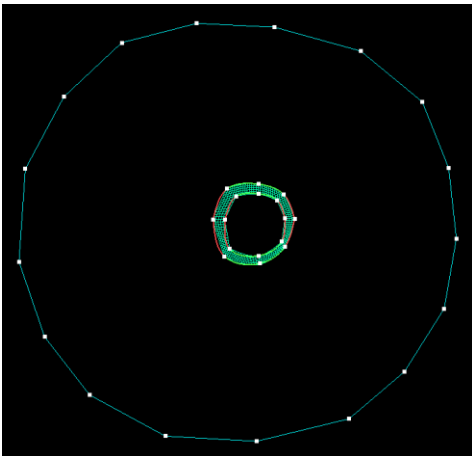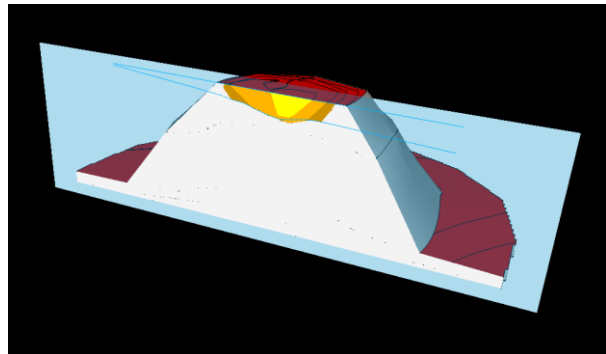

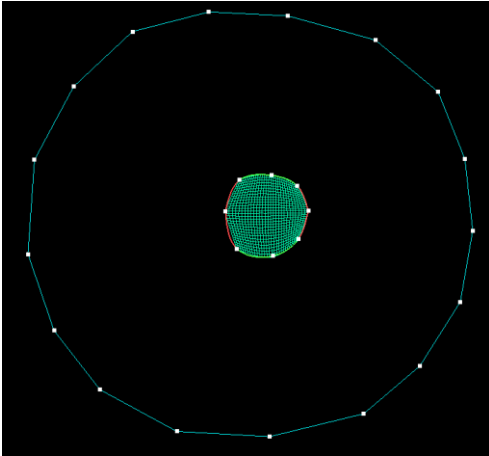Figure 104: Faults that marge the upper part of the Outer Lagoon were used for creating the 3D grid. The upper part of the outer lagoon is represented by the green mid skeleton. By using this grid only the flanks, but not the bottom of the outer lagoon was realized.
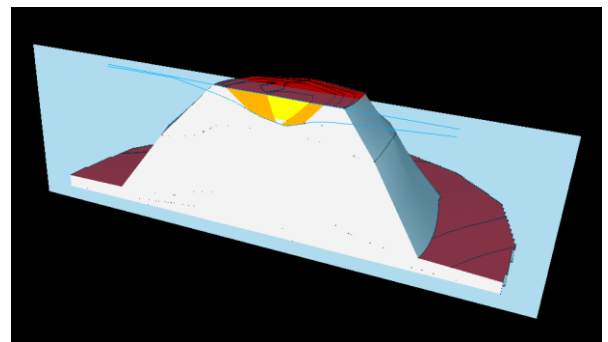
Figure 105: Upper part of the outer lagoon (orange zonation) with top and bottom horizons (marked as straight lines). Remaining reef is indicated as grey zonation.
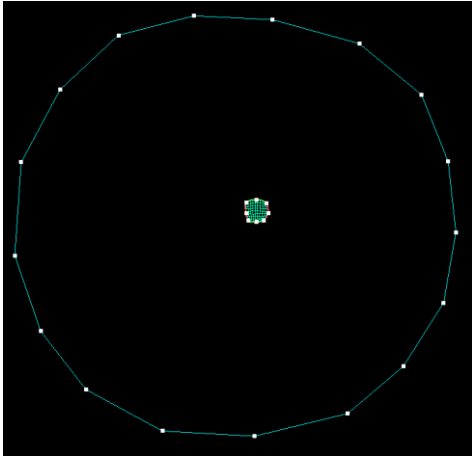
Figure 106: Faults that marge the lower part of the outer lagoon were used for creating the 3D grid. The lower part of the outer lagoon is represented by the green mid skeleton.
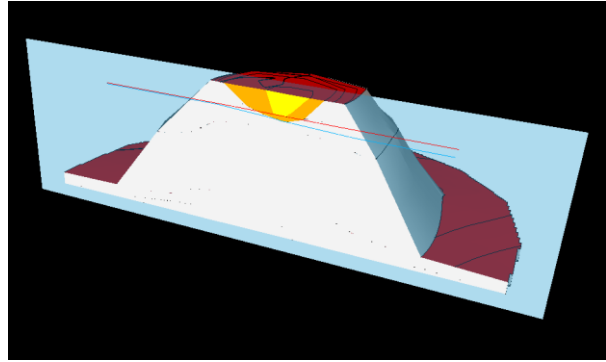
Figure 107: Lower part of the outer lagoon (orange zonation below the yellow inner lagoon and the orange flanks of the outer lagoon) with top and bottom horizons (marked as straight lines). Remaining reef is indicated as grey zonation.

Figure 108: Faults that marge the upper part of the reef core were used for creating the 3D grid. The upper part of the reef core is represented by the green mid skeleton. By using this grid only the flanks, but not the bottom of reef core can be realized.

Figure 109: Upper part of the reef core (brown zonation) with top and bottom horizons (marked as straight lines). Remaining reef is indicated as grey zonation.

Figure 110: Faults that marge the lower part of the reef core were used for creating the 3D grid. The lower part of the reef core is represented by the green mid skeleton.
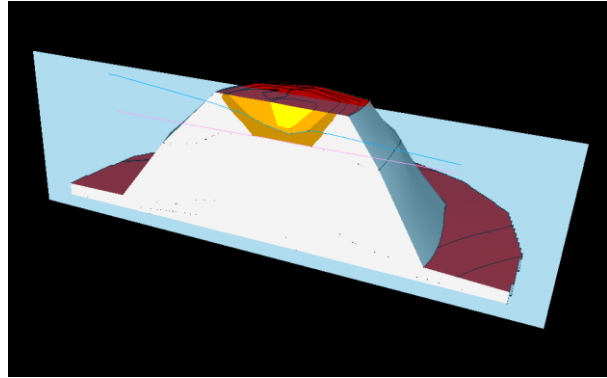
Figure 111: Lower part of the reef core (brown zonation below the orange outer lagoon and the brown upper part of the reef core) with top and bottom horizons (marked as straight lines). Remaining reef is indicated as grey zonation.
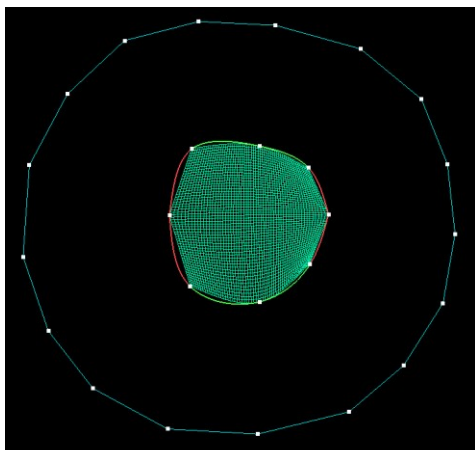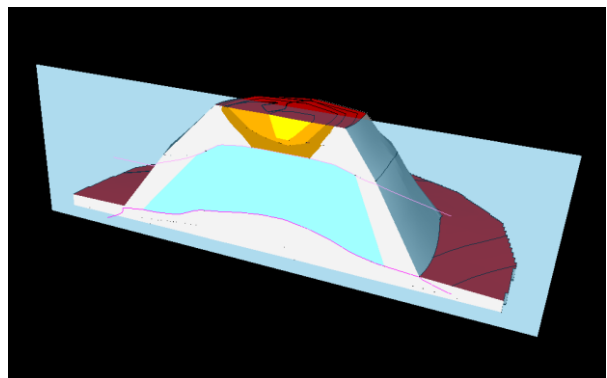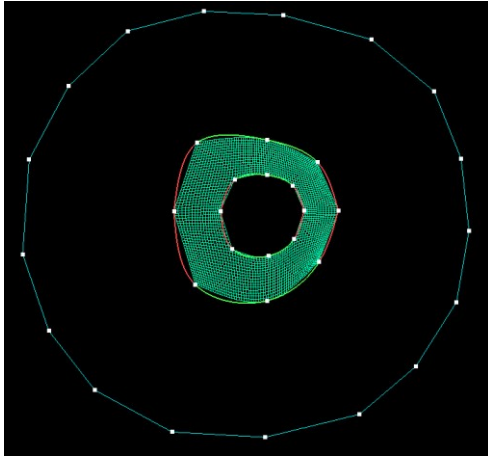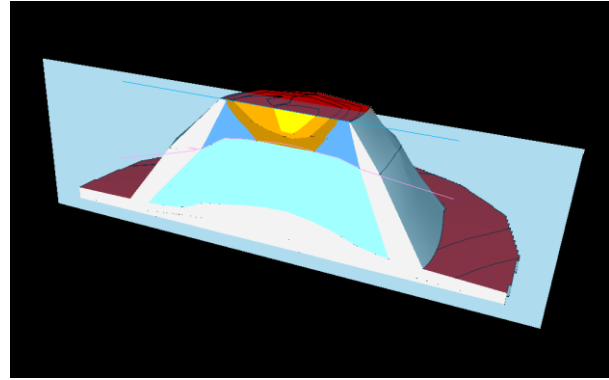

Figure 112: Faults that marge the upper mound stage were used for creating the 3D grid. The upper mound stage is represented by the green mid skeleton.

Figure 113: Upper mound stage (green zonation) with top and bottom horizons (marked as straight lines). Remaining reef is indicated as grey zonation.

Figure 114: Faults that marge the reef core were used for creating the 3D grid. The reef core is represented by the green mid skeleton.

Figure 115: Reef core (blue zonation with top and bottom horizons (marked as straight lines). Remaining reef is indicated as grey zonation.
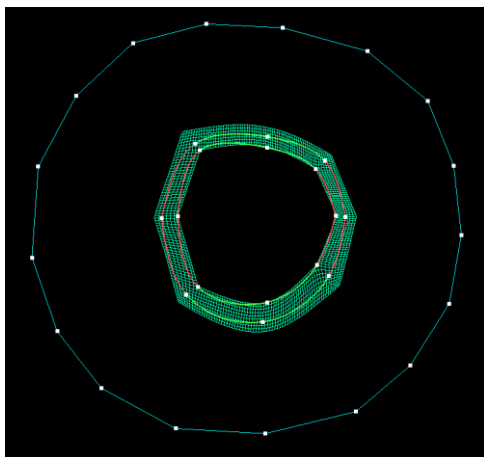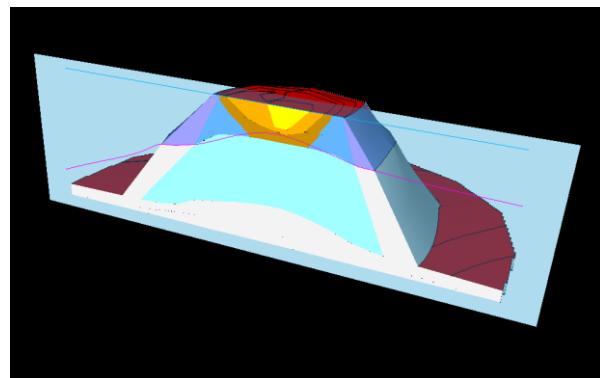

Figure 116: Faults that marge the upper part of the forereef were used for creating the 3D grid. The upper part of the forereef is represented by the green mid skeleton. By using this grid only the upper part, but not the bottom of the forereef can be realized.

Figure 117: Upper part of the forereef (purple zonation) with top and bottom horizons (marked as straight lines). Remaining reef is indicated as grey zonation.
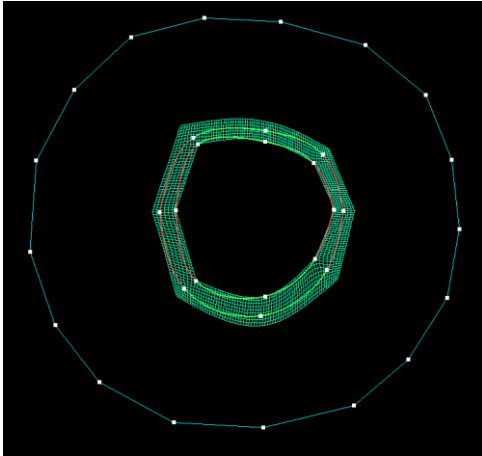
Figure 118: Faults that marge the lower part of the forereef were used for creating the 3D grid. The lower part of the forereef is represented by the green mid skeleton.
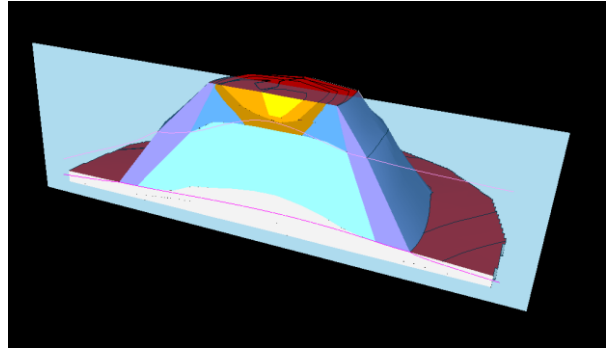

Figure 119 Lower part of the forereef (purple zonation below the purple upper part of the forereef) with top and bottom horizons (marked as straight lines). Remaining reef is indicated as grey zonation.
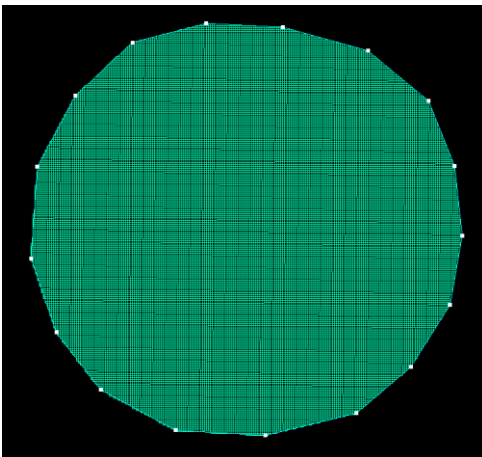

Figure 120: Faults that marge the lower mound stage were used for creating the 3D grid. The lower mound stage is represented by the green mid skeleton.
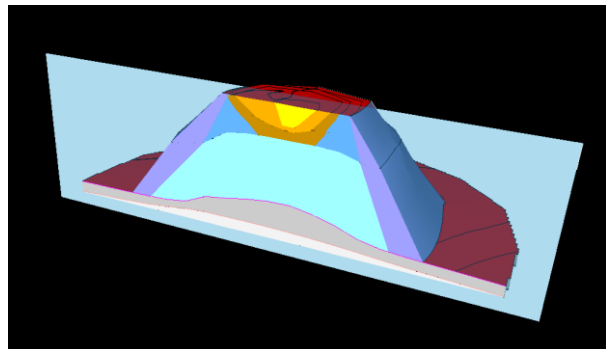

Figure 121: Lower mound stage (middle grey zonation) with top and bottom horizons (marked as straight lines. Remaining reef is indicated as grey zonation.
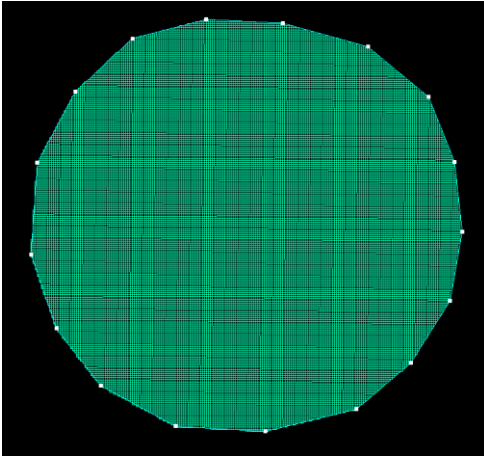
Figure 122: Faults that marge the open shelf were used for creating the 3D grid. The open shelf is represented by the green mid skeleton.
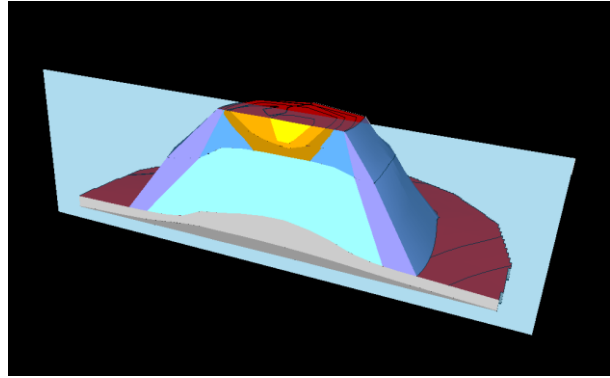

Figure 123: Open shelf (dark grey zonation) with top and bottom horizons (marked as straight lines).